



**THREE-DIMENSIONAL POSITRON ANNIHILATION
MOMENTUM MEASUREMENT TECHNIQUE APPLIED
TO MEASURE OXYGEN-ATOM DEFECTS IN 6H
SILICON CARBIDE**

DISSERTATION

Christopher S. Williams, Lieutenant Colonel, USAF
AFIT/DS/ENP/10-M02

**DEPARTMENT OF THE AIR FORCE
AIR UNIVERSITY**

AIR FORCE INSTITUTE OF TECHNOLOGY

Wright-Patterson Air Force Base, Ohio

APPROVED FOR PUBLIC RELEASE; DISTRIBUTION UNLIMITED

The views expressed in this dissertation are those of the author and do not reflect the official policy or position of the United States Air Force, Department of Defense, or the United States Government.

AFIT/DS/ENP/10-M02

THREE-DIMENSIONAL POSITRON ANNIHILATION MOMENTUM
MEASUREMENT TECHNIQUE APPLIED TO MEASURE OXYGEN-
ATOM DEFECTS IN 6H SILICON CARBIDE

DISSERTATION

Presented to the Faculty

Department of Engineering Physics

Graduate School of Engineering and Management

Air Force Institute of Technology

Air University

Air Education and Training Command

In Partial Fulfillment of the Requirements for the

Degree of Doctor of Philosophy

Christopher S. Williams, MS Nuclear Engineering, MS Environmental Engineering

Lieutenant Colonel, USAF

March 2010

APPROVED FOR PUBLIC RELEASE; DISTRIBUTION UNLIMITED

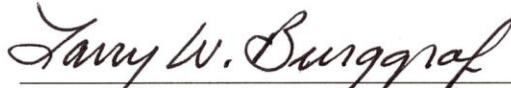
THREE-DIMENSIONAL POSITRON ANNIHILATION MOMENTUM
MEASUREMENT TECHNIQUE APPLIED TO MEASURE OXYGEN-ATOM
DEFECTS IN 6H SILICON CARBIDE

Christopher S. Williams, MS Nuclear Engineering, MS Environmental Engineering

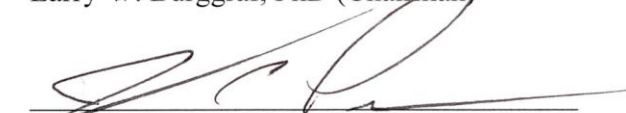
Lieutenant Colonel, USAF

Approved:

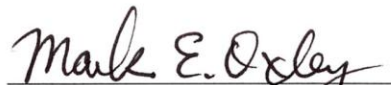
Date


Larry W. Burggraf, PhD (Chairman)

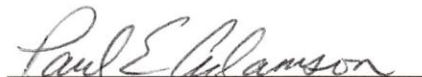
15 Mar 2010


James C. Petrosky, PhD (Member)

15 Mar 10


Mark E. Oxley, PhD (Member)


15 Mar 2010


Paul E. Adamson, PhD (Member)

8 Mar 2010

Accepted:

Date


M. U. Thomas
Dean, Graduate School of
Engineering and Management

19 Mar 2010

Abstract

A three-dimensional Positron Annihilation Spectroscopy System (3DPASS) capable to simultaneously measure three-dimensional electron-positron (e^-e^+) momentum densities measuring photons derived from e^-e^+ annihilation events was designed and characterized. 3DPASS simultaneously collects a single data set of correlated energies and positions for two coincident annihilation photons using solid-state double-sided strip detectors (DSSD). Positions of photons were determined using an interpolation method which measures a figure-of-merit proportional to the areas of transient charges induced on both charge collection strips directly adjacent to the charge collection strips interacting with the annihilation photons. The subpixel resolution was measured for both double-sided strip detectors (DSSD) and quantified using a new method modeled after a Gaussian point-spread function with a circular aperture. Error associated with location interpolation within an intrinsic pixel in each of the DSSDs, the subpixel resolution, was on the order of ± 0.20 mm (this represents one-standard deviation). The subpixel resolution achieved was less than one twenty-fifth of the 25-mm^2 square area of an intrinsic pixel created by the intersection of the DSSDs' orthogonal charge collection strips. The 2D ACAR and CDBAR response for single-crystal copper and 6H silicon carbide (6H SiC) was compared with results in the literature. Two additional samples of 6H SiC were irradiated with 24 MeV O^+ ions, one annealed and one un-annealed, and measured using 3DPASS. Three-dimensional momentum distributions with correlated energies and coincident annihilation photons' positions were presented for all three 6H SiC samples. 3DPASS was used for the first experimental measurement of the structure of oxygen defects in bulk 6H SiC.

Acknowledgements

Completion of this research would not have been remotely possible without the help of several people. First, my advisor, Dr. Burggraf, provided not only the intellectual assistance and mentorship necessary for this massive undertaking, but also the patience and considerable encouragement I needed (and greatly appreciated) to make the final push to complete the project. I thank him for his persistent support and tolerance.

Next, I would like to thank the AFIT model shop folks, Jan, Dan, Brian and Jason. Their willingness to make my last minute rush jobs a priority and their willingness to finish them before I needed them saved me valuable time and stress. Also, Eric's assistance in assembling my experiment apparatus and maintaining and filling them with LN₂, enormous amounts of LN₂, was greatly appreciated.

Next, to my fellow PHDs, Dave, Tom and Ty. I am indebted to their competitiveness and eagerness to bounce ideas off of. Their spirited competition to lead the pack pushed me to study just a tad more and strive to do better than I thought I could. Also, they were always willing to help with complex concepts and reviewing codes and papers. This helped me overcome several complicated problems.

Finally and most importantly, I would like to thank my wife and sons. I knew when we agreed to pursue my PhD I needed their support, which was unwavering. Through the coursework, specialty exams, and research, they always understood when I had to take time away to study or complete assignments.

Christopher S. Williams

Table of Contents

	Page
Abstract	iv
Acknowledgements	v
Table of Contents	vi
List of Figures	ix
List of Tables	xiii
1. Introduction	1
1.1. Motivation	1
1.2. Overview	4
2. Theory	6
2.1. Overview	6
2.2. Positrons, The Discovery	6
2.3. Positron Production	7
2.3.1. Lifetimes	9
2.4. Positron Interactions	9
2.4.1. Positron Annihilation	10
2.4.2. Positronium Formation and Annihilation	11
2.4.3. Positron Interaction with Matter	12
2.5. Positron Annihilation Spectroscopy Techniques	15
2.5.1. Positron Annihilation Lifetime Spectroscopy	15
2.5.2. Doppler-Broadening of Annihilation Radiation	17
2.5.3. Angular Correlation of Annihilation Radiation	26
2.6. Electronics	31
2.7. Pulse Processing Basics: Pulse Formation and Transient Charge	32
2.8. Pulse Shape Analysis	39
2.9. Spatial Resolution	43
2.10. SiC Material Characteristics	48
2.11. Oxygen in SiC	50
2.12. Investigation of SiC Using PAS Techniques	52
2.13. Investigation of Ion Irradiated SiC	56
2.14. Investigation of Cu Using PAS Techniques	58
3. Equipment	63
3.1. Overview	63

	Page
3.2. Position-Sensitive Semiconductor Detectors	63
3.2.1. Ortec Detector	63
3.2.2. PHDS Position-Sensitive Semiconductor Detectors	65
3.3. Electronics.....	66
3.3.1. XIA Digitizers	67
3.3.2. Spec32.....	68
3.4. Sources Used.....	70
3.5. Samples Used.....	71
3.6. Vacuum Chamber and Pump	71
3.7. Source Shielding	72
3.8. Collimator Fabrication	73
3.9. Translator	74
4. Procedure to Finalize Spectrometer Layout and Sample Preparation	75
4.1. Resolution Characterization of Ortec and PHDS DSSDs.....	75
4.2. Relative Interpolation Method for Determining Full-Charge Event Location Using Transient Charge Analysis	76
4.3. Spatial Resolution Determination.....	78
4.3.1. Validity of FOM Proportionality Assumption.....	84
4.3.2. Efficiency of the Interpolation Method	86
4.4. Absolute Interpolation Method.....	88
4.5. Compensation for Subpixel Efficiency	90
4.6. Potential Correlation Between Event Energy and Associated FOMs.....	94
4.7. Spectrometer Layout.....	95
4.8. Code Development.....	97
4.9. Simultaneous 2D ACAR and CDBAR Experiment.....	99
4.10. Ion Irradiation	101
4.11. Sample Annealing and Diffusion of O Atoms	104
5. Results and Discussion	106
5.1. Overview	106
5.2. PALS Measurements	106
5.3. Virgin Cu 2D ACAR Response with No DSSD Efficiency Compensation	109
5.4. Virgin Cu 2D ACAR Response Compensated for DSSD Efficiency.....	112
5.5. Virgin Cu 2D CDBAR Response	117
5.6. Virgin 6H SiC 2D ACAR Response With and Without DSSD Efficiency Compensation.....	123
5.7. Virgin 6H SiC 2D CDBAR Response	129
5.8. 3D Momentum Distribution for Virgin 6H SiC.....	134
5.9. O ⁺ Ion Irradiated, Un-annealed 6H SiC 2D ACAR Response With DSSD Efficiency Compensation.....	138
5.10. O ⁺ Ion Irradiated, Un-annealed 6H SiC 2D CDBAR Response.....	143

	Page
5.11. 3D Momentum Distribution for O ⁺ Ion Irradiated, Un-annealed 6H SiC	147
5.12. O ⁺ Ion Irradiated, Annealed 6H SiC 2D ACAR Response with DSSD Efficiency Compensation.....	150
5.13. O ⁺ Ion Irradiated, Annealed 6H SiC 2D CDBAR Response	152
5.14. 3D Momentum Distribution for O ⁺ Ion Irradiated, Annealed 6H SiC	157
6. Conclusions and Future Work	160
Appendix A Spec32 Settings and Operation	164
Appendix B Lifetime Spectra and PALSfit Results	167
Bibliography	175

List of Figures

Figure	Page
1. Diagram of three PAS techniques: PALS, 2D ACAR and CDBAR	3
2. Decay scheme of ^{22}Na	7
3. Positron emission spectrum of a ^{22}Na source	8
4. Positron-electron annihilation in the center-of-mass frame of reference.....	10
5. Ross' fast-fast PALS hardware layout used for the PALS measurements	16
6. Valence and core electron contributions to annihilation photopeak.....	19
7. 511-keV annihilation photopeak using 1 and 2 detector DBAR	21
8. Regions of interest for 1D DBAR annihilation photopeak.....	22
9. Example 2D DBAR spectrum for well-annealed aluminum	25
10. Exaggerated relationship between annihilation photons (p^1 , p^2) and the transverse electron momentum prior to annihilation	27
11. Sample 1D ACAR spectrometer (not to scale)	29
12. Sample 2D ACAR spectrometer (not to scale)	30
13. Diagrams of hole and electron migration current as a function of time	34
14. Transient charge and full-charge signals from 662-keV photon interaction within Cooper et al's detector	38
15. Hypothetical pulse shape from a HPGe detector (not to scale)	40
16. Image charge asymmetry parameter distribution for an event location.....	42
17. Single layer tetrahedral bond structure for SiC polytypes	49
18. Rempel et al's DB lineshape for 6H SiC, diamond and Si.....	53
19. 2D ACAR spectra for 6H SiC by Kawasuso et al	55
20. Theoretical prediction for 6H SiC by Kawasuso et al	55
21. Annihilation lineshape for Ni, Cu, Sb, Ge, and Si.....	59

Figure	Page
22. 2D ACAR spectra for single-crystal Cu	60
23. 1D ACAR spectra for (100) annealed, virgin and neutron-irradiated Cu.....	61
24. Ortec HPGe DSSD and electrode layout (not to scale)	64
25. Event location using intersecting front and rear strips (not to scale).....	65
26. Photograph of PHDS detector and electrode masking layout (not to scale).....	66
27. Picture of DGF-4C digital waveform acquisition/spectrometer card	67
28. Photograph of Spec32 digitizer system.....	69
29. Vacuum chamber and pump	72
30. Subpixel irradiation pattern on Ortec's F3/R3 pixel.....	78
31. Full-charge and transient waveforms.....	81
32. 2D histogram for subpixel locations within the Ortec DSSD's intrinsic pixel.....	81
33. 2D contour plot for subpixel locations within the Ortec DSSD's intrinsic pixel	82
34. Gaussian point-spread function with circular aperture and normalized count distribution (corrected for background)	84
35. Relative average efficiency as a function of distance from the center of the intrinsic pixel for both DSSDs.....	87
36. Successor-only FOM values at each subpixel location across F3/R3 intersection.....	89
37. Predecessor-only FOM values at each subpixel location across F3/R3 pixel	89
38. 2D count distribution in DSSDs over entire active charge collection strips.....	91
39. Subpixel average relative efficiency for Ortec and PHDS DSSD	93
40. Correlation between event energy and FOMs	95
41. Final spectrometer configuration with PHDS and Ortec DSSDs (not to scale)	96
42. SRIM output for 24.0 MeV O ⁺ ions in SiC	103
43. Single-crystal Cu 2D ACAR spectrum reconstructed from the 3DPAMM data.....	110

Figure	Page
44. Contour plot of Cu ACAR momentum distribution displaying misalignment	110
45. Cu raw and smoothed ACAR projections without efficiency compensation	111
46. Cu raw and smoothed ACAR projections with efficiency compensation	114
47. Derivative of projections extracted from Cu ACAR spectrum.....	115
48. Single-crystal Cu CDBAR spectrum	117
49. Single-crystal Cu DB lineshape for $\Delta = 0, 0.3$, and 0.5 keV	119
50. Derivative of DB lineshape with $\Delta = 0.3$ keV for virgin Cu	121
51. Derivative of DB lineshape and ACAR projections for Cu.....	122
52. Virgin 6H SiC 2D ACAR spectrum with and without efficiency compensation	125
53. Virgin 6H SiC 2D ACAR position-corrected spectrum (efficiency compensated) ..	127
54. First two layers in 6H SiC unit cell rotated 45° on (100) axis	129
55. Virgin 6H SiC CDBAR spectrum using the same events from ACAR analysis	130
56. Virgin 6H SiC DB lineshape for $\Delta = 0, 0.3$, and 0.4 keV	131
57. Derivative of DB lineshape with $\Delta = 0.3$ keV for virgin 6H SiC	134
58. 3D momentum lineshape for virgin 6H SiC	136
59. O^+ ion irradiated, un-annealed 6H SiC 2D ACAR spectrum.....	139
60. O^+ ion irradiated, un-annealed 6H SiC 2D ACAR spectrum with virgin 2D ACAR subtracted out	141
61. First two layers in 6H SiC unit cell with O atom interstitial	142
62. O^+ ion irradiated, un-annealed 6H SiC DB lineshape for $\Delta = 3$ keV.....	144
63. Derivative of DB lineshape with $\Delta = 0.3$ keV for O^+ ion irradiated, un-annealed 6H SiC	145
64. Ratio curve for ion irradiated, un-annealed 6H Si.	147
65. 3D momentum lineshape ion irradiated, un-annealed 6H SiC	148

Figure	Page
66. O^+ ion irradiated, annealed 6H SiC 2D ACAR spectrum	150
67. O^+ ion irradiated, annealed 6H SiC 2D ACAR spectrum with ion irradiated, un-annealed 2D ACAR subtracted out	152
68. O^+ ion irradiated, annealed 6H SiC DB lineshape for $\Delta = 3$ keV	153
69. Derivative of DB lineshape with $\Delta = 0.3$ keV for ion irradiated, annealed 6H SiC ..	155
70. Ratio curve for ion irradiated, annealed 6H Si	156
71. 3D momentum lineshape for ion irradiated, annealed 6H SiC	158
72. Lifetime spectrum for virgin, single-crystal Cu.....	167
73. Lifetime spectrum for virgin, single-crystal 6H SiC	168
74. Lifetime spectrum for O^+ ion irradiated, un-annealed single-crystal 6H SiC.....	168
75. Lifetime spectrum for O^+ ion irradiated, annealed single-crystal 6H SiC	169

List of Tables

Table	Page
1. Key properties for common semiconductors	1
2. Physical properties of SiC polytypes	49
3. 6H-SiC Bulk, V_C , V_{Si} , and $V_{Si}V_C$ theoretical and experimental lifetimes.....	52
4. FWHM of each strip in Ortec and PHDS DSSDs.....	76
5. Comparison of actual and observed subpixel location	85
6. Average relative efficiency of each subpixel type in each DSSD	92
7. Final Spec32 settings for experiment.....	164

THREE-DIMENSIONAL POSITRON ANNIHILATION MOMENTUM MEASUREMENT TECHNIQUE APPLIED TO MEASURE OXYGEN-ATOM DEFECTS IN 6H SILICON CARBIDE

1 Introduction

1.1 Motivation

Wide band-gap semiconductors, like silicon carbide (SiC) and gallium nitride for example, were extensively studied in the past few decades for use in electronic devices. SiC is further gaining utility in several applications: micro-structures, opto-electric devices, high temperature electronics, radiation hard electronics and high power/frequency devices [1]. This increased popularity is the result of several favorable SiC properties which make SiC devices suitable for use in harsh environments: low density, high strength, low thermal expansion, high thermal conductivity, high hardness and superior chemical inertness. Table 1 compares important SiC properties with other materials commonly used in the above applications.

Table 1. Key properties for common semiconductors [2].

Property	Si	GaAs	GaP	3C SiC (6H SiC)	GaN
Band Gap (eV) at 300 K	1.1	1.4	2.3	2.2 (2.9)	3.39
Maximum Operating Temp (K)	600	760	1250	1200 (1580)	
Melting Point (K)	1690	1510	1740	Sublimes >2100	
Electron Mobility RT, (cm ² /V s)	1400	8500	350	1000 (600)	900
Hole Mobility RT, (cm ² /V s)	600	400	100	40	150
Thermal Conductivity c_T , (W/cm)	1.5	0.5	0.8	5	1.3
Dielectric Constant K	11.8	12.8	11.1	9.7	9

Several of the above listed properties of SiC are well-matched to applications in severe environments. SiC's band-gap, operating temperature and melting point are suitable for devices that operate in high temperature environments. Exceptional radiation hardness, coupled with the capability of operating at high temperatures, enables SiC to be utilized in nuclear reactors and in space assets which require maximum survivability. Finally, SiC's high thermal conductivity and electron mobility make it well-suited for increased power density and high frequency operations, like high-powered microwave power switches, in which the Air Force is very interested.[1] With so many possible applications for SiC, reliably characterizing deep-level defects in bulk, as-grown material is critical.

Several methods are currently used by groups in the scientific community and industry to measure and characterize defects in semiconductor materials, to include photoluminescence (PL), electron paramagnetic resonance (EPR) and positron annihilation spectroscopy (PAS). PAS encompasses several experimental techniques; the most commonly used are positron annihilation lifetime spectroscopy (PALS), Doppler-broadening of annihilation radiation (DBAR), and angular correlation of annihilation radiation (ACAR), displayed in Figure 1. These non-destructive PAS techniques have been gaining increasing popularity as a result of technological improvements in detector performance and affordability of digital electronics.

While PAS techniques can provide a wealth of information on the structure of the material interrogated, they have an inherent problem. The application of the coincidence DBAR (CDBAR) technique results in a one-dimensional measurement of the electron-

positron (e^-e^+) momentum distribution parallel to their motion, whereas two-dimensional ACAR (2D ACAR) results in the two-dimensional measurement of the momentum distribution in the plane perpendicular to the e^-e^+ pair's motion. Historically, these two techniques were applied separately and independently to provide a partial description of the e^-e^+ momentum distribution. However, interpretation of spectra using total 3D momentum conservation was not possible because the data was uncorrelated.

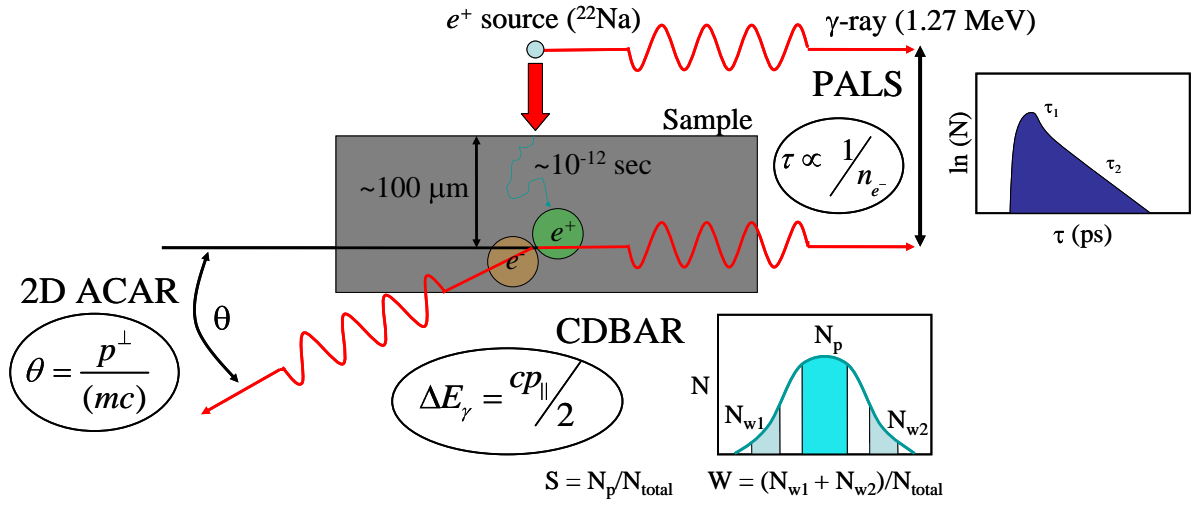


Figure 1. Diagram of three PAS techniques: PALS, 2D ACAR and CDBAR.

The individual techniques, themselves have several limitations. First, for DBAR applications, the detection system used must possess extremely fine energy resolution, bordering on the limit of most semiconductor detector systems, in order to reveal information about the material's core electron environment. Next, ACAR measurements require high activity sources and large distances between detectors and the sample in order to obtain sub-milliradian (mrad) angular resolution. The large footprint is necessary to achieve adequate angular resolution. Additionally a considerable source

activity is required to overcome the inefficiency of the large system to collect a spectrum in a reasonable amount of time. Unless the efficiency is significantly improved, a high activity source is required. Finally, copious amounts of data produced from PAS measurements have been historically ignored due to the inability to efficiently collect and store the data. Although these problems have plagued many PAS experiments, simple novel engineering techniques and post acquisition processing can significantly improve current state-of-the-art PAS systems and practices and produce a single measurement producing the three-dimensional e^-e^+ momentum distribution.

A three-dimensional Positron Annihilation Spectroscopy System (3DPASS) was designed to simultaneously determine total electron-positron (e^-e^+) momentum densities from e^-e^+ annihilation photons. 3DPASS collects a single data set of correlated photon energies and positions of coincident annihilation photons. These data are typically collected individually using the 2D ACAR and CDBAR PAS techniques. 3DPASS extracts the 3D momentum distribution by the technique termed three-dimensional positron annihilation momentum measurement (3DPAMM), enabling conservation of total momentum to be used to interpret results. The measurement of the total 3D momentum distributions of virgin copper (Cu) and virgin and oxygen (O)-atom defected 6H SiC was demonstrated and 3D momentum lineshapes were constructed for all measured 6H SiC samples.

1.2 Overview

The focus of this research effort was to design and develop a single spectrometer composed of two, position-sensitive semiconductor detectors that when used together,

extracted correlated CDBAR and ACAR spectra from a single measurement. This was possible by incorporating several engineering enhancements and by using post acquisition pulse processing. This system was applied to analyze virgin (un-irradiated) Cu and 6H SiC single-crystal with and without O-atom defects by ion bombardment. In order to understand how to improve PAS techniques, the origins of the growth of PAS to its current state-of-the-art techniques with relevant published research is presented. A brief background summary of positron physics and a solid-state physics review of SiC are presented in Chapter 2.

Once the theoretical groundwork is laid, a thorough discussion of the equipment incorporated in this experiment, as well as, the engineering techniques and post acquisition pulse processing improvements to the system are detailed in Chapter 3.

Several experiments were conducted in order to characterize the systems in 3DPASS and finalize the layout of the spectrometer. This, along with methods used to extract momentum data from the electronics' raw output files is described in Chapter 4.

Chapter 5 presents the raw and processed data and results of the momentum data analysis. 3DPAMM data sets were collected and analyzed for virgin single-crystal Cu and 6H SiC and the 2D ACAR and CDBAR response was compared with results in the literature. Two samples of the 6H SiC were irradiated with O^+ ions, one annealed and the other un-annealed, and subsequently measured using 3DPASS. The measurement of the total 3D momentum distributions of these defect structures were demonstrated and 3D momentum lineshapes were constructed for all three 6H SiC samples. The major conclusions of the research and future work are summarized in Chapter 6.

2 Theory

2.1. Overview

In order to employ PAS techniques, it is important to understand the underlying physics of positrons. This section starts with a brief overview on the discovery of positrons. Next, the discussion dives into how positrons are produced and the mechanisms by which they interact with matter. Following that, the topic turns to a review of the state-of-the-art PAS techniques pertinent to this research: DBAR and ACAR. Then, electronics used for signal acquisition and processing and their operation are explained. Once that is complete, pulse processing basics is introduced by examining induced charge, pulse formation and transient charge. This is followed by post acquisition pulse shaping processing pertinent to these PAS techniques. Finally, the chapter concludes with a solid-state review of SiC.

2.2. Positrons, the Discovery

In 1928, P. Dirac first hypothesized the existence of a positively-charged electron in his discussion of the quantum theory of the electron [3]. Dirac's solutions to the relative wave equation, which included the electron with negative charge and a particle of equal mass but with a positive charge, overcame several difficulties associated with the accepted quantum mechanical theories at that time. Even though the theory seemed mathematically sound, the physics community was uneasy with this new theory due to the absence of experimental proof of the particle's existence. This was overcome,

however, when in 1932, Carl Anderson experimentally verified the existence of the anti-electron, the positron.

During Anderson's experiments of photographing cosmic-rays in a Wilson chamber, tracks were visible that could only result from a particle of positive charge having the same mass as an electron; hence, the positron was discovered [4]. Both scientists' contributions to the physics community were so monumental that Dirac and Anderson were awarded the Nobel Prize for their work.

2.3 Positron Production

Positrons are produced by many processes, but the most economical manner is from the natural decay of radioactive isotopes. Sodium-22 (^{22}Na), which has a half-life of 2.606 years, is the most commonly used positron source throughout the scientific community. Commercially available ^{22}Na is typically produced by the bombardment of aluminum with energetic protons [5]. The natural decay of ^{22}Na is written as



where ν is the neutrino and Ne^* is the excited neon atom (Figure 2).

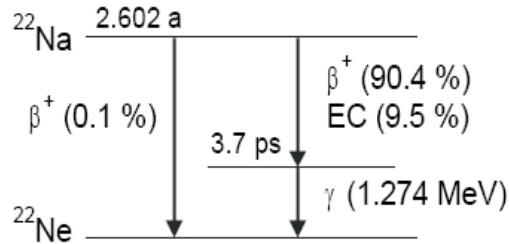


Figure 2. Decay scheme of ^{22}Na . 90.4 % decays by emission of a positron and neutrino to the excited state of ^{22}Ne . The ground state is reached after 3.7 psec by emission of a γ release of 1.274 MeV [6:7].

Neutrinos have a small probability of interaction with matter [6], so they are undetected and neglected for most practical gamma detection applications. The energy is shared by the β^+ particle and the ν and is not constant. The fixed decay constant, i.e. the energy shared by the β^+ particle and the ν , can range from zero to the beta endpoint energy; which for ^{22}Na is 546 keV, with an average energy of 215 keV [7:529]. Figure 3 is an example of a positron emission spectrum. The energy of the positron can be moderated using various techniques to a desired energy window, as illustrated in Figure 3, as well. SiC itself has been demonstrated to be an effective moderator [8]. Stormer et al [9] measured 6H SiC's positron work function (Φ^+), -3.0 ± 0.2 eV, which is the same value for the most commonly used positron moderator, well-annealed tungsten.

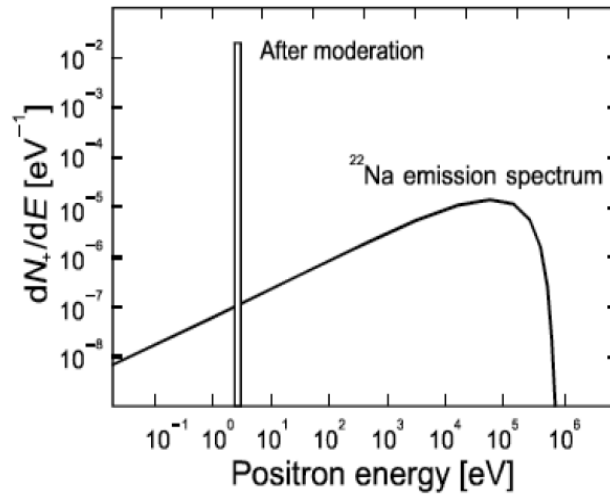


Figure 3. Positron emission spectrum of a ^{22}Na source. dN_+/dE is the number of positrons per energy channel E . The narrow curve centered at 3 eV displays the energy distribution after moderation in tungsten [10].

2.3.1 Lifetimes

The lifetime of a positron is defined as the time between the birth of a particle until its death by annihilation. The positron lifetime is specifically the time from when the positron is emitted from the β^+ decay of ^{22}Na , for example, until the positron annihilates with an electron. ^{22}Na decays by β^+ to an excited state of neon-22, ^{22}Ne , 90% of the time. The ^{22}Ne de-excites in 3.7 psec by emitting a 1.27 MeV photon. The 3.7-psec lifetime is short enough that it can be considered to be emitted simultaneously with the β^+ particle, making it a suitable birth-indicator, the start pulse.

Lifetimes are a function of the local electron density which is highly influenced by the material's electrical, magnetic, chemical and physical properties. Positron lifetimes are inversely proportional to the local electron density in which the positron exists and interacts. In theory, the intrinsic lifetime of a positron in a vacuum should approach the limit of that of the electron, which is 4×10^{23} years. The longest a positron has been trapped, however, is approximately 3 months. In condensed matter, where the local electron density is much greater than that of a vacuum, positron lifetimes are on the order of 500 psec. [11:4]

2.4. Positron Interactions

A positron can interact with a material by a variety of mechanisms before and after it thermalizes in material. Many models have been developed to describe this behavior. Only the fundamental interactions pertinent to this research will be covered in this section. Three fundamental mechanisms exist for thermal positron interactions: colliding with a free or bound electron in matter and annihilating, formation of

Positronium and subsequent annihilation, or the formation of a positron bound state with an atom or molecule in matter.

2.4.1 Positron Annihilation

Annihilation occurs when matter and antimatter combine and transform into energy, governed by the equation $E = mc^2$ in Einstein's theory of relativity, as show in Figure 4.

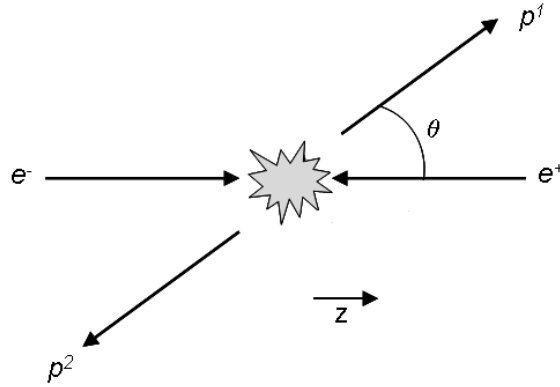


Figure 4. Positron-electron annihilation in the center-of-mass frame of reference.

In Figure 4, e^- is the electron, e^+ is the positron and p^1 and p^2 are the photons emitted from the annihilation event.

Annihilation is a process which conserves energy and momentum, which can produce a spectrum of possible events to include a radiationless process, a one-photon emission, a two-photon emission, a three-photon emission, and so on. The two-photon emission process is the most probable result from e^-e^+ annihilations. In fact, Ore and Powell [12] discovered the cross-sections for annihilation for the three-photon emission

process was $1/370^{\text{th}}$ of that for the two-photon process. Higher order photon emission processes have even a lower probability of occurrence.

In the two-photon emission, the e^-e^+ pair annihilate and two photons of exactly 511 keV are emitted, exactly collinearly, in the center-of-mass (COM) frame-of-reference due to the conservation of energy and momentum. In the laboratory frame of reference, however, due to the conservation of momentum, the momentum of the e^-e^+ pair prior to their annihilation results in the emission of the two 511-keV photons in directions that deviate slightly from exactly π radians. The deviation from collinearity is typically on the order of mrad. This deviation will be discussed in more detail in later sections.

2.4.2 Positronium Formation and Annihilation

Positronium (Ps) formation is a competing process with direct annihilation discussed above. The positron can combine with an electron to form a quasi-stable neutral bound state, the Ps “atom”. Two types of Ps exist—ortho- (o-Ps) and para- (p-Ps) which differ only in the spin combination of the positron and electron. If the spin is parallel, p-Ps forms (the triplet state where $S = 1$) and the combination of an electron with a positron with anti-parallel spin forms o-Ps (the singlet state where $S = 0$). The reduced mass of Ps is half that of the hydrogen atom, thereby, reducing the binding energy of the ground state of Ps to 6.8 eV.

Several models have been developed to describe the formation of Ps at the microscopic level. This research will not attempt to detail these models, except to describe the basic spur model. Basically, as a positron loses its kinetic energy through scattering a material and slows down to thermal energies, it has a high probability of

reacting with one of the electrons liberated by ionization of the media. This typically occurs at the end of the positron track, termed the terminal spur, which consists of ~30 ion pairs, making conditions favorable for Ps formation [11:73].

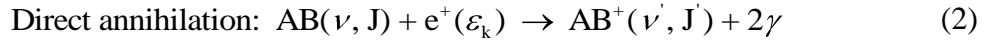
Eventually, the positron in Ps will annihilate with an electron. The annihilation processes for both types of Ps differ. Free p-Ps undergoes intrinsic annihilation (i.e., annihilation occurs between the electron and positron composing the Ps atom) into an even number of photons, most probabilistically two-photons. Free o-Ps, on the other hand, annihilates into an odd number of photons, assuming it annihilates without external influences. In matter, however, the positron in o-Ps can pick off an electron with an opposite spin from within the material and annihilate only via the two-photon annihilation process. This is called pick-off annihilation. The lifetimes of free p-Ps and o-Ps are 0.125 ns and 142 ns, respectively, and for pick-off annihilation, the lifetime is on the order of several nanoseconds [11:3].

2.4.3 Positron Interaction with Matter

When a positron is emitted from the decay of ^{22}Na , it can possess energy from a wide spectrum, as shown in Figure 3. As a result, a positron's interaction with matter is also a spectrum and a function of the positron's energy. At high energies, typically in the range of keV to MeV, positrons interact with matter similarly as electrons. The primary mechanisms for energy deposition are inelastic collisions and molecular and atomic excitation. At lower energies, however, positrons interact differently than electrons.

For low positron energies, typically less than one keV, elastic scattering and annihilation are the only possibilities. As the positron energy increases, Ps formation

becomes probable, then molecular/atomic excitation, then ionization, then inelastic channels open. Direct annihilation of a positron with a target electron is possible at all positron energies, but the cross section for annihilation is usually smaller than the other process outlined above. Direct annihilation is described by the following formula:



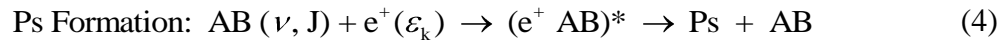
where AB is the molecule prior to annihilation with vibrational energy level ν and rotational energy level J and ε_k is the energy of the positron.

If the energy of the positron exceeds the ionization energy of Ps and is less than the ionization energy of the molecule, then Ps can form. The probability of Ps formation increases as the energy of the positron above the ionization energy of Ps increases. The formation threshold for Ps is:

$$E_{Ps} = E_i - \frac{6.8(eV)}{n_{Ps}^2} \quad (3)$$

where E_i is the ionization potential of the target material and E_{Ps} is the binding energy of the Ps state with principal quantum number n_{Ps} .

Ps may be formed in any allowed excited state, but is typically (and most probably) formed in the ground state, or $n_{Ps}=1$. The primary reaction for Ps formation is preceded by the positronic molecule in an excited rovibronic state as shown in Equation (4):



where $(e^+ AB)^*$ is the positronic molecule in an excited rovibronic state.

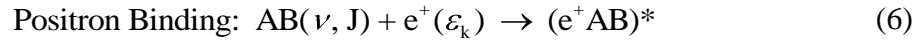
If the positron possesses energy greater than the ionization energy of the molecule, then Ps formation is less probable because the positron interaction with the

molecule by electronic excitation or ionization begins to dominate. A positron with less energy than the ionization energy of the molecule minus the binding energy of the ground state of Ps in a vacuum cannot pick up an electron from the molecule to form Ps. This is expressed as the Ore Gap which is defined by:

$$I_{molecule} - \frac{Ry}{2} < E_p < I_{molecule} \quad (5)$$

where $I_{molecule}$ is the ionization energy of the molecule, E_p is the energy of the positron and $Ry/2$ is the binding energy of the ground state of Ps in a vacuum.

If Ps does not form, i.e. the energy of the positron is just above the ionization energy of the molecule, then the positron just binds to the molecule and the excess energy excites the positronic molecule in an excited rovibronic state. The reaction is:



A positron with sub-ionization energy can also combine with an electron within the terminal spur to form Ps. “Quasi-free” Ps atoms can be trapped by the crystal lattice of a material. This process may be inefficient in a salt, however, because the electron/positron attraction can be shielded by the ions.

Ps formation is minimal in metallic and semiconductor materials, since the electron density must be extremely low for this to occur. If no open-volume defects are present in the semi-conductor, which could provide an adequate location for Ps formation, Ps typically will only form on the surface. Ps formation is more probable in molecular solids, where the electron density is much lower.

A thermalized positron may also become localized or “trapped” in a negatively-charged site in a material’s lattice such as a vacancy. The trapping rate is dependent on

the concentration of vacancies (the positron must encounter such a site within the 100-nm diffusion length since this is the average length a positron travels in bulk material). Also, the positron's lifetime in a trapping site is inversely proportional to the electron density at the site.

2.5 Positron Annihilation Spectroscopy Techniques

Three types of positron annihilation spectroscopy (PAS) are prominently used in the scientific community today: PALS, DBAR and ACAR. This research will focus on the integration of two PAS momentum techniques: CDBAR and 2D ACAR. The next few sections will give a discussion on the physics of these two momentum techniques, including a brief summary of PALS, as well as, discuss current state-of-the-art characteristics.

2.5.1 Positron Annihilation Lifetime Spectroscopy

PALS relies on the measurement of the time between the birth signal from the radioactive decay of ^{22}Na and the stop signal resulting from detection of one or both annihilation photons. Numerous PALS systems have been documented in the literature but only the system used in this research will be discussed. PALS measurements reported in this document used the fast-fast system assembled by Ross [13], incorporating analog NIM electronics. The system's schematic is shown in Figure 5.

The detectors consist of a scintillator crystal made of barium fluoride, BaF_2 , manufactured by Saint-Gobain Crystals and a photomultiplier tube (PMT). BaF_2 has a very fast component in its scintillation decay (0.7 ns) and a high atomic number which make it suitable for applications requiring both high efficiency and fast response [6]. The

BaF₂ crystal is optically coupled to a Hamamatsu PMT that changes the optical signal from the detector into an electronic current pulse via a photocathode coupled to an electron multiplier cascade. The cascade is relatively short, though, in order to reduce time contributions to the incoming fast signal.

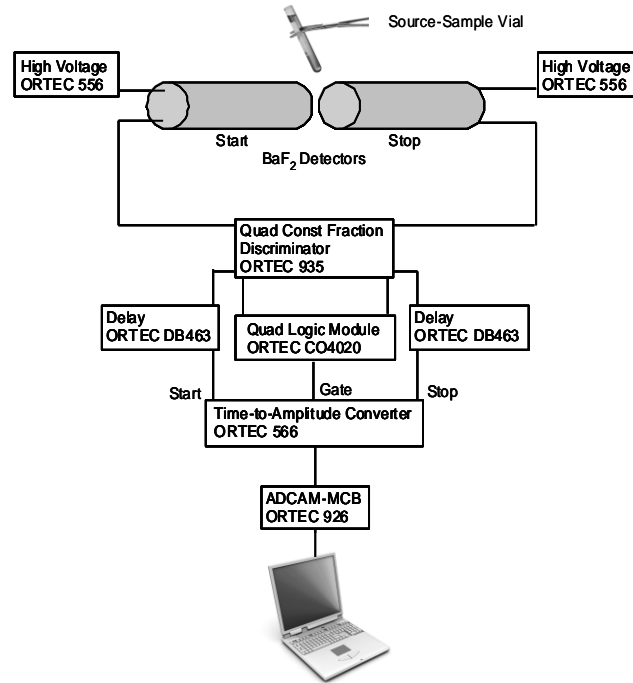


Figure 5. Ross' fast-fast PALS hardware layout used for the PALS measurements in this research.

The crystal on the start detector is 2-in in diameter and 3-in thick and the stop detector crystal size is 2-in thick. The larger crystal size on the start detector is more efficient at capturing the higher energy 1.27-MeV photons of the start pulse. Bias voltage was set to -2300 V on each detector.

The timing resolution of the system was determined to be 197 psec by directly measuring the full-width at half maximum (FWHM) of a ⁶⁰Co timing spectrum and

multiplying by the time-per-channel. ^{60}Co was used to characterize the time resolution of a PALS system because it emits two photons during its decay (1332 and 1173 keV) nearly simultaneously. This results in a coincidence timing peak of a single channel, or a delta function. Any peak broadening observed is a direct result of the noise induced during the signal's processing through the electronics suite and represents the inherent timing resolution of the system.

2.5.2 Doppler-Broadening of Annihilation Radiation

The DBAR technique, has been gaining increasing popularity for defect identification and characterization in materials. DBAR was born in 1949, when DuMond, Lind and Watson were measuring the wavelength of the annihilation radiation from a ^{64}Cu source using a curve-crystal spectrometer. During their measurements, a broadening of the peaks associated with the annihilation radiation was observed, which they could not associate with the spectrometer's inherent resolution from electronic components. They concluded the observance was due to Doppler-broadening and primarily resulted from electronic momentum [14]. This began the interest in DBAR.

Recall, in the COM frame of reference, annihilation radiation emitted from the e^-e^+ pair annihilation event results in collinear photon emission. The motion of the e^-e^+ pair prior to annihilation creates the Doppler shift in the annihilation radiation measurement. Since the electron is bound, it typically has a larger momentum contribution to the e^-e^+ pair's momentum, relative to the positron. In most published research, the positron's momentum is neglected and therefore, any Doppler-broadening is associated solely with the electron in the direction parallel to the motion of the e^-e^+ pair

prior to annihilation. In materials with weakly bound electrons, however, the electron's momentum prior to annihilation may only be marginally larger than that of the positron. Therefore, it is prudent to always include the positron's momentum contribution in momentum measurements involving e^-e^+ annihilation.

The DBAR technique involves measuring the energy of the annihilation photons. The energy of the annihilation photons is $511 \text{ keV} \pm \Delta E_\gamma$, where ΔE_γ is the Doppler shift. The shift in energy from 511 keV is described as:

$$\Delta E_\gamma = mc v_{cm} \cos \phi = \frac{c p_{\parallel}}{2} \quad (7)$$

where v_{cm} is the velocity of the center of mass of the e^-e^+ pair, c is the speed of light, and ϕ is the angle between the propagation of the e^-e^+ pair and the direction of one of the emitted photons and p_{\parallel} is the momentum component parallel to the annihilating pair's motion [15]. Typically, ΔE_γ is on the order of approximately 1.2 keV [16:14]. Therefore, a measurement of the Doppler shift results in quantification of the momentum distribution of the e^-e^+ pair prior to annihilation.

In early DBAR experiments, a one-dimensional (1D) apparatus was used. In this configuration, the DBAR spectrometer observed only one of the annihilation photons. Therefore, the intrinsic resolution of the single detector was an extremely important factor for resolving features in the DBAR spectrum. Background in the spectra using this type of system is typically large and masks structure in the base of the peak. As the resolution of spectrometers have improved in the last few decades and development of lower noise electronics, structure in the base of the annihilation photon's photopeak

representing positron interactions with high momentum core electrons bound to the atoms in the sample interrogated were observed.

As structure in the base of the photopeak became more defined, contributions to electron momentum distributions from core electrons in material were revealed. The large Gaussian-shape in the center of the photopeak is attributed to a positron annihilating with an outer-shell valence electron in a metal, which occurs with high frequency. Outer-shell electrons generally have low momentum compared to core electrons since they are more weakly bound to the atom. The portion of the photopeak which reflects this is depicted in left window in Figure 6. Lower frequency events are attributed to positrons

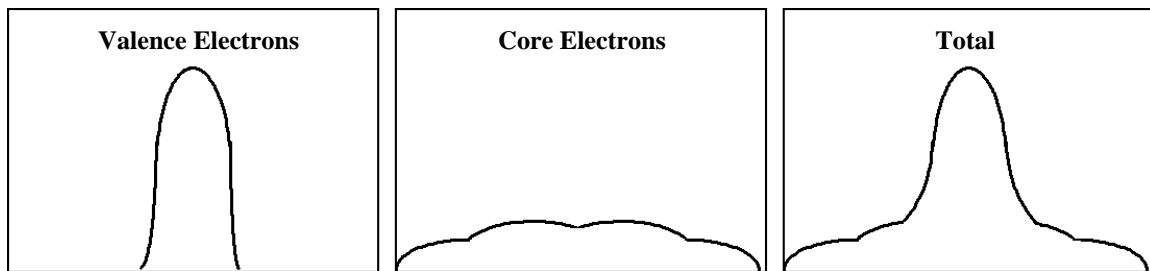


Figure 6. Valence and core electron contributions to annihilation photopeak [11:54].

annihilating with core electrons. These are higher momentum events as due to the overlap of the positron's wave function with the core electron's, which are more tightly bound to the atom. To reach these inner-shell electrons, positrons must overcome the nucleus' coulomb repulsion and interact with the much higher momentum core electrons. Since the core electrons' momentum is higher than that of the valence electrons, the Doppler shift is greater. The intensity is much lower than annihilations with valence electrons, however, resulting in low frequency components in the high momentum

regions of the DBAR spectrum [17]. This is depicted in the center window in the above Figure 6. Summing up the contributions from core and valence electrons produces the photopeak that is visible in the DBAR spectrum, illustrated in the right window in Figure 6. Therefore, deconvolution of the components in the DB broadened photopeak can be used to deduce details of the electronic structure of a material, if the spectrometer's resolution can resolve the components. Several research groups investigated this observation. Nascimento et al experimentally collected a DBAR spectrum from an aluminum sample and developed an algorithm to fit the collected 511-keV Doppler-broadened photopeak [18]. The model's predicted intensities for the interactions of thermalized positrons with the aluminum's band, 2p, 2s, and 1s electrons fit the experimental data they collected fairly well.

In 1976, Lynn and Goland, realized by utilizing a two-dimensional (2D) CDBAR spectrometer, a system with two detectors in coincidence, and thereby looking at both annihilation photons in coincidence, a drastic reduction in background resulted. In fact, Baranowski et al compared the photopeak from a 1D to a 2D DBAR spectrum and achieved more than a 10^3 reduction in background, as shown in Figure 7. This background reduction revealed structure in the base of the photopeak previously described, indicating it was experimentally possible to examine momentum distributions in the high momentum regions by using a 2D CDBAR spectrometer [19].

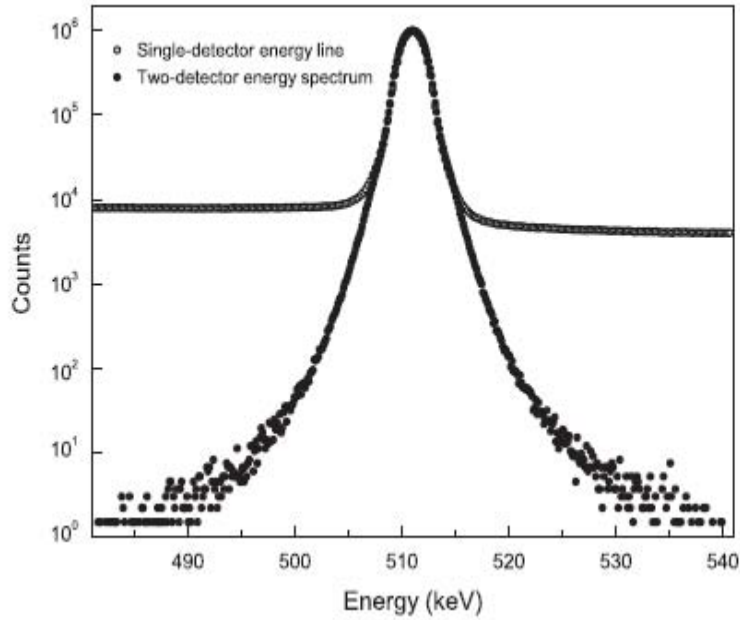


Figure 7. 511-keV annihilation photopeak using 1 and 2 detector DBAR [22].

Detectors most often used in single detector 1D DBAR experiments are coaxial Germanium (Ge) or High Purity Germanium (HPGe) semiconductor detectors with a resolution of ~ 1.1 keV at 514 or 478 keV (the calibration peaks of sources of ^{85}Sr or ^7Be , respectively) [20]. Most two-detector geometries also incorporate Ge or HPGe detectors, as in the case of Nagai et al, which benefits from exceptional resolution from the Ge crystal but suffers from poor efficiency [21]. Jean et al suggested that a HPGe detector in coincidence with a more efficient detector, like NaI(Tl), would combine the good resolution of the semiconductor detector with that of the good efficiency of the scintillator [11:56].

While most detectors used in state-of-the art DBAR spectrometers achieve a resolution of ~ 1.1 keV, digital electronics have not been widely used to further improve the spectrometer's resolution. Even in 2004, with the increased affordability of digital

electronics, Baranowski et al, forwent the benefits of digital electronics for a large cascade of analog electronics modules for a two detector DBAR system [22].

Incorporation of digital electronics in this type of PAS system is a simple engineering technique that can greatly increase throughput and post-acquisition data processing.

Data resulting from a DBAR spectrum is fairly straight forward to analyze. In the 1D DBAR example photopeak shown below in Figure 8, the only information available is the standard spectral result, a plot of the number of counts per channel, calibrated to energy.

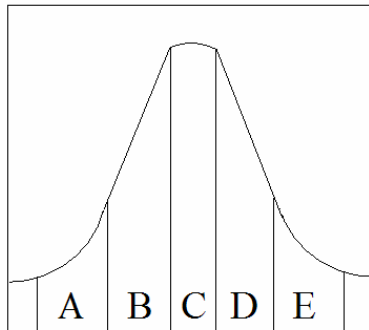


Figure 8. Regions of interest for 1D DBAR annihilation photopeak [11:55].

Typically, the annihilation photopeak, also referred to as the Doppler-broadened (DB) lineshape is described by 2 parameters: the sharpness (labeled S) and the wing parameter (labeled W). Six multi-channel analyzer (MCA) channels are chosen symmetrically about the annihilation photopeak to define five regions of interest, labeled A, B, C, D and E. Two constraints are usually applied. First, the areas of A and E must be approximately equal and the wing parameter should be as follows:

$$W = \left(\frac{A+E}{T} \right) \approx 0.25 \quad (8)$$

where T is the total area (A + B + C + D + E) of the photopeak. The second constraint is the sharpness should relate as follows:

$$S = \frac{C}{T} \approx 0.5 \quad (9)$$

First, a 1D DBAR spectrum is measured on a defect-free (or virgin) material. The regions of interest are determined and set and S and W are determined (the non subscripted parameters refer to the defect-free material's parameters). Then, bulk material with defects is analyzed and the regions of interest, using the same channel numbers as in the defect-free material, are added. S_{bulk} and W_{bulk} are subsequently determined. As material samples with varying concentrations of defects are analyzed, the ratios of S/S_{bulk} and W/W_{bulk} are compared.

Several research efforts have been published detailing 1D DBAR experiments on SiC. Dekker et al used a two Ge detector DBAR system and analyzed how the S and W parameters varied as a function of positron energy and as a function of location on a SiC sample with oxide layers [23]. Additionally, Karwasz et al examined the S parameter as a function of positron energy in 6H SiC. They observed a slow fall of the S parameter from the surface to the bulk value, indicating a long diffusion length, i.e. absence of positron-trapping defects [24]. Finally, Maekawa et al was able to distinguish the interface layer between the SiO₂ and SiC layers using S and W parameter correlation [25]. While 1D DBAR measurements can lead to a qualitative understanding on the structure of the material interrogated, the 2D DBAR configuration can provide more

information based on the increased capability of resolving interactions with core electrons.

In the 2D CDBAR configuration, the data is handled different, but the conclusions from the analysis can be substantially improved than 1D DBAR. The data consists of a count, represented by a coincidence event detected by both detectors and an energy recorded in each detector. The spectrum transitions from a two-dimensional arrangement (counts as a function of energy in one detector) to three-dimensional (counts as a function of energy in two detectors). The x and y axis of the spectrum indicates the energies recorded in each detector for the coincident annihilation event and the z axis reflects the frequency of counts with those energies. Figure 9 displays an example of a 2D DBAR spectrum for well-annealed aluminum [22]. E_1 and E_2 are the energies recorded by each detector, which in this case, are both planar HPGe detectors. The shaded regions in the spectrum indicate the number of counts above background, where the darker contrast indicates increased counts. The advantage to populating the spectrum in this fashion is to identify processes which decrease the resolution of the spectrum, like pile-up events on the high-energy side of the photopeak and incomplete charge collection in the detectors on the low energy side of the photopeak. Finally, the diagonal area highlighted in the figure is the area of interest, displaying the coincident Doppler-broadened lineshape.

The DB lineshape is extracted from the spectra and analyzed just like the S/W method for the 1D DBAR outlined above. Typically, the DB lineshape is extracted by examining the diagonal that is one bin-unit wide (based on the bin dimension of the 2D DBAR spectrum) or is taken as a width defined by a predetermined parameter. In the case of the 2D spectrum by Baranowski et al [22], their DB lineshape was 4 keV wide.

That was approximately the binding energy of the electron in aluminum, which is the material they interrogated. They neglected the positron's kinetic energy, assuming the kinetic energy was approximately zero. As variously defected material is subsequently analyzed, the contrasting areas will change relative to each other based on the quantity and types of defects present due to their influence on the momentum on the e^-e^+ pair.

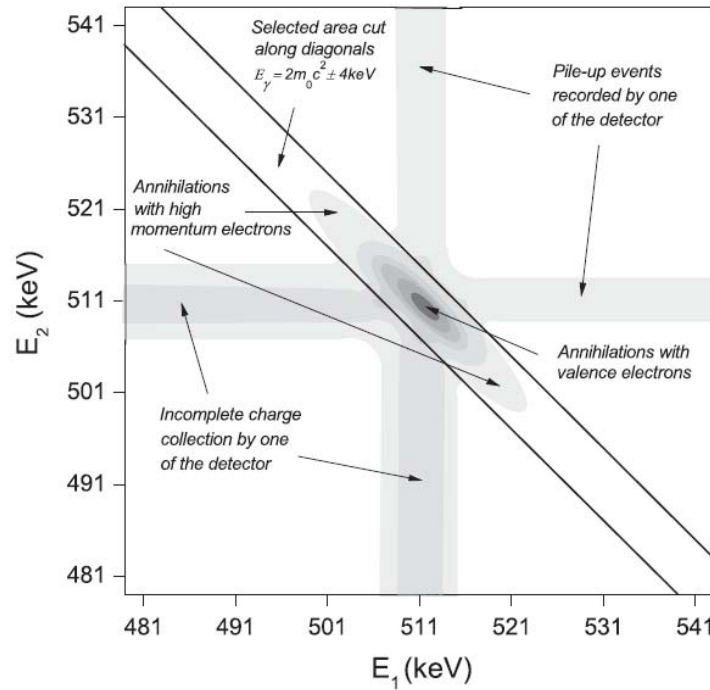


Figure 9. Example 2D DBAR spectrum for well-annealed aluminum [22].

Another analysis gaining popularity over the S/W method is the use of ratio curves. This method provides a semi-quantitative evaluation of changes in momentum distributions as a function of defect types and concentrations. DB lineshapes from samples with defects are compared with lineshapes of defect-free material samples by simply normalizing the DB lineshape count distribution to the lineshape of the defect-free

spectrum. The resulting comparison reveals the momenta characteristics of the defects, when combined with another technique, like PALS, the defects can be identified and their concentration calculated. This will be discussed later in the SiC PAS research.

The spectral analysis in Figure 9 above was conducted by Baranowski et al using similar, planar HPGe detectors. Using Jean et al's suggestion of combining the good resolution of a semiconductor detector with that of the good efficiency of a scintillator in a two detector DBAR application would not have the same benefits as the system described above in Figure 9. The efficiency of the scintillator can be up to an order of magnitude greater, or more, than that of a semiconductor. The energy resolution, however, for a standard 3 x 3 in NaI detector is on the order of 7% at 662 keV [26], versus ~0.3% for coaxial germanium detectors [27]. This large difference in resolution causes a widening of the scintillator's contribution to the 2D spectrum and results in only an order of magnitude background reduction compared to the 1D DBAR technique [28]. Even with the addition of the scintillator's efficiency, the 2D representation of the spectrum is not likely feasible when using one semiconductor and one scintillator in the two detector arrangement.

2.5.3 Angular Correlation of Annihilation Radiation

The other PAS momentum technique relevant to this research, ACAR, has also been gaining popularity as a non-destructive defect characterization tool. From Section 2.4.1, in the laboratory frame, there is a slight deviation in collinearity, where the angle is no longer π radians. In 1942, Beringer and Montgomery first observed a slight deviation from collinearity using a coincident counting apparatus, but the system's resolution was

too poor for any significant conclusions, on the order of a half of a degree [29]. By 1949, however, DeBenedetti et al had achieved an angular resolution on the order of 4 mrad using two anthracene detectors in coincidence. They observed up to a ± 15 mrad deviation from collinearity while examining a sample of gold [30].

The deviation from collinearity in the laboratory frame is due to the fact the e^-e^+ pair has momentum, primarily provided by the electron. As shown in Equation (10), performing a simple transformation from the COM to the laboratory frame-of-reference and solving for the angle, the deviation from collinearity can be expressed as a function of the electron momentum prior to annihilation, as displayed in Figure 10:

$$\theta = \frac{p^{x,y}}{(mc)} = \frac{p^\perp}{(mc)} \quad (10)$$

where $p^{x,y}$ and p^\perp are both the momentum component in the plane perpendicular to the direction of the annihilation photons' emission and is θ the angular deviation from collinearity [12:16].

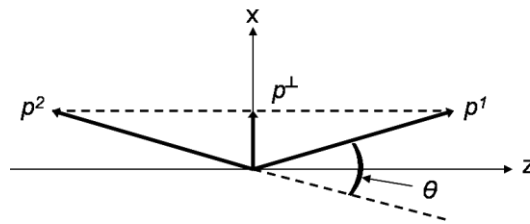


Figure 10. Exaggerated relationship between annihilation photons (p^1, p^2) and the transverse electron momentum prior to annihilation [16:15].

Therefore, a direct measurement of the angular deviation using the annihilation photons will provide information on the momentum component in the plane perpendicular to the motion of the e^-e^+ pair prior to annihilation.

Two types of ACAR geometries are used, 1D and 2D. The 1D ACAR apparatus is typically referred to as the slit geometry, and was predominantly used up until the end of the 90's. In this configuration, collimators are used to define the angular resolution of the system. In Figure 11 below, the right detector (B) is held stationary and is collimated by two parallel collimators, separated by a distance d . The left detector (A) is collimated by two parallel collimators also separated by d . The left detector and parallel collimators are rotated thru an angle of $\pm \theta$ while the spectrum is acquired. Using simple geometry, the angular resolution of the system can be set as a function of the distance between the sample and the moving detector and d between the parallel collimators. Since the angular resolution of the spectrometer is a function of the slit produced by the parallel collimators, detector selection is not extremely critical. Typically, a detector with good resolution is used for the stationary component, like Ge or HPGe since these usually require liquid nitrogen cooling, and a highly efficient detector is used as the rotated component, like NaI(Tl). This was the exact setup utilized by Singru in 1973 while examining single-crystal Cu with a 1D ACAR spectrometer [31].

An important limitation of 1D ACAR is the technique limits the detection of higher-momentum components by only looking in one dimension. As a result, 1D ACAR cannot resolve complicated structure of the Fermi surface, the surface of constant energy in momentum (or k) space which separates occupied levels from unoccupied levels in electronic energy bands [32]. Therefore, 1D ACAR is most useful for substances without

a periodic lattice or symmetry, like gasses, liquids, and amorphous solids. Single-crystal metals, semimetals, and doped semiconductors, however, would best be analyzed using the 2D ACAR technique [12:16], [11:57].

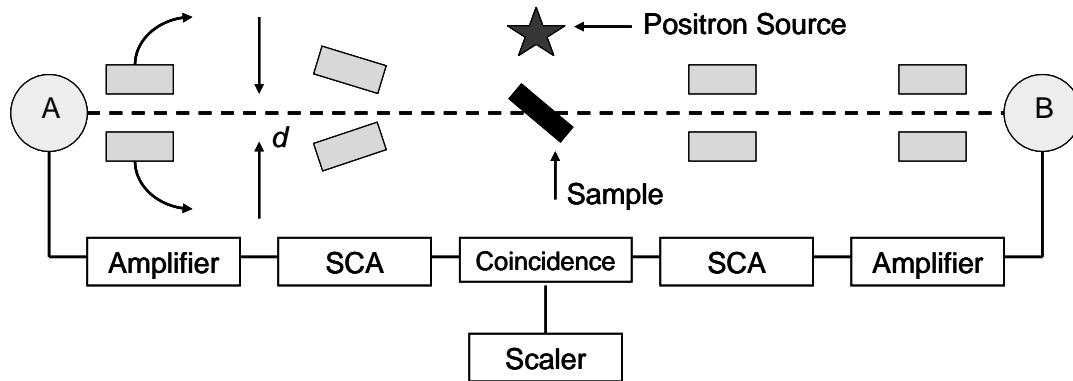


Figure 11. Sample 1D ACAR spectrometer (not to scale) [11:37].

The 2D ACAR technique is slightly different. 2D ACAR spectrometers started to become common in PAS research starting in the end of the 90's. The operation of this type of ACAR spectrometer relies on position-sensitive detectors. Position-sensitive detectors function by the photons interacting with the detector material which is sampled by multiple, discrete PMT's (or pixels) or position-sensitive PMT's. The location of the event is triangulated in electronics or software as a function of which PMTs sampled the event and the relative intensities of the event in each PMT. Since the detector's surface geometry is a major factor contributing to the angular resolution of the spectrometer, careful consideration must be taken in detector selection. Detector characteristics to consider for use in a 2D ACAR system are spatial resolution, detection efficiency, time and energy resolution and detector surface area and shape. Some common detectors used

in 2D ACAR are discrete scintillation detector arrays, multi-wire proportional counters, and Anger cameras. A typical 2D ACAR spectrometer is illustrated in Figure 12.

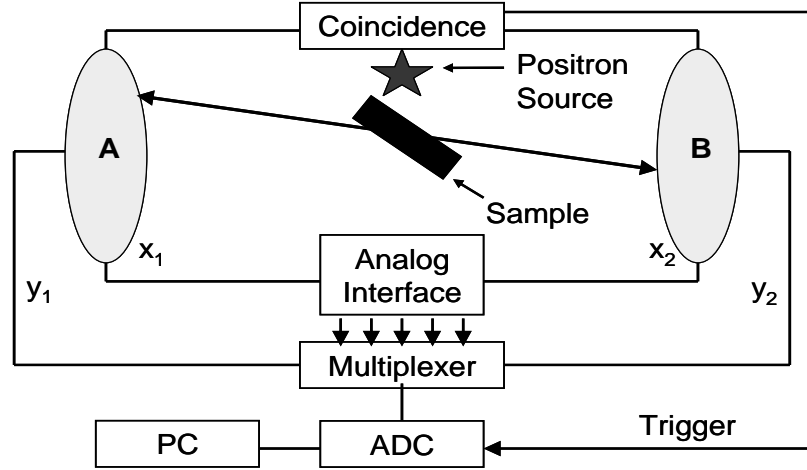


Figure 12. Sample 2D ACAR spectrometer (not to scale) [11:58].

2D ACAR, in contrast to the 1D technique, provides two-dimensions of the momentum distribution which can reveal the directionality of momentum anisotropies from core or valence electron influences, if it is present in the material interrogated. Additionally, 2D ACAR does not limit the detection of higher-momentum components, since two dimensions are examined. Therefore, 2D ACAR is very useful for materials with a periodic lattice structure and a high degree of symmetry, like metals, semimetals and semiconductors. With sufficient angular resolution and multiple spectra collected along planes orthogonal to the lattice's axes, 2D ACAR data can reconstruct the Fermi surface of these types of materials using a number of techniques transforming the ACAR momenta distributions into the Fermi momentum [33,34,35,36]. This research will not attempt to reconstruct the Fermi surface from the momentum data.

With the increasing popularity of 2D ACAR in research and the drive to improve angular resolution, detectors for 2D ACAR spectrometers have become an enterprising market all by themselves. Inoue et al developed a 2676 element $\text{Bi}_4\text{Ge}_3\text{O}_{12}$ (BGO) scintillation array detector with 7 x 7 blocks of BGO elements optically coupled to PMT's [37]. Each BGO crystal had a surface dimension of 2.6 x 2.6 mm, which given the right spectrometer configuration, could give excellent angular resolution. Burks et al developed a segmented, 39 x 39 orthogonal strip planar Ge detector [38]. This detector not only could locate a photon interaction within the area of the detector, but also determined the depth in the crystal at which the photon interaction occurred, using the relative timing of the signals induced by the drifting electrons and holes. In theory, this detector could break into the realm of 3D ACAR spectroscopy, but the crystal's thickness is negligible compared to the distance between the sample and the detector, so this dimension's utility is severely limited.

2.6 Electronics

Both the 1D and 2D ACAR spectrometers illustrated above incorporate analog electronics. Digitizing the detector's signal directly from the output of the detector or PMT has several advantages over processing the detector's signal and converting the analog waveform to digital just prior to data collection. First, depending on the complexity of the detectors, i.e. individual detector elements, position sensitive PMT's, etc, the number of analog electronic modules could grow rapidly. This cascade of analog modules can potentially cause instability and allow significant drift. Per Knoll, any drift that arises in the course of signal processing could result in peak broadening or spectral

distortion [6:700]. Secondly, all that is required for digital acquisition is a module containing the number of inputs equal to the number of signals. Some state-of the-art digitizers are capable of accepting up to 32 inputs, drastically reducing the real estate required to perform the experiment. Thirdly, digital signal processing is simply a matter of user defined parameters in software versus hardware-enabled analog signal processing. In fact, several possible digital pulse shapes, like the flat-top with cusp-like rise and fall, cannot even be attained in analog circuitry [6:648]. Finally, the amount of data accumulated during an ACAR experiment is extremely large. In a 1D ACAR experiment, required counting times can be upwards of 100 hours due to scanning through an angular range. In a 2D ACAR data set, each detection event contains x and y coordinates for each detector, the energy in each detector, the timing of each event in each detector, and θ , assuming this is determined during data acquisition, which amounts to long data streams for individual events. Regardless, since the signal is already digitized, digital electronics have the capability of storing data to a host of buffers and transferring to a computer when necessary with little impact to active data collection, even at high count rates. Analog-to-digital converters (ADC) in analog circuits, however, are limited to identifying individual events by its intrinsic clock speed. If multiple pulses arrive quicker than the ADC clock, the events will not be differentiated [6:648].

2.7 Pulse Processing Basics: Pulse Formation and Transient Charge

One of the objectives of this research is to accurately determine the location of the annihilation photons interactions within the detectors' crystals. Transient charge analysis allowed for the location of the photon's interaction within the detector to within a fraction

of the width of the charge collection strips in the detectors. Transient charge, also known as image charge, is a phenomenon common to segmented or pixelated detectors where transient signals may be induced on more than one segments or pixels from a single event within the detector [6:793]. Before a discussion on transient charge can occur, a foundation on pulse formation and induced charge within the detector must be introduced.

In a standard semiconductor detector, electron-hole pairs are the fundamental information carriers. A pulse formed in a semiconductor starts when incident radiation interacts with a thin disk of the semiconductor material, in this experiment, it was planar germanium, by either photoelectric absorption, Compton scattering or pair production based on the photon's incident energy. All three processes result in an electron which, as it travels through the semiconductor material, deposits energy, through various mechanisms. This causes valence electrons in the semiconductor's lattice structure to excite, and if the energy overcomes the band gap, the valence electron excites across the band gap into the conduction band, also creating a hole in the valence band. As the electron produced by the photon's interaction with the semiconductor deposits energy, N_o number of electron-hole pairs are produced in its track, with a total energy of eN_o , where e is the electron energy. Applying an electric field to the semiconductor will cause these electron-hole pairs to migrate parallel to the electric field vector. The electrons move in the direction opposite to the electric field vector; whereas, the holes move in the same direction of the electric field vector. The migration of electrons and holes each induce a current which continues until they stop migrating or are collected. Two ohmic contacts (or electrodes or charge collection strips), one on each end of the semiconductor will

collect both the electrons and the holes, summing to the induced charge. Both the electron and hole of each pair and all electron-hole pairs must be collected for the pulse to accurately describe the energy of the electron resulting from the photon's interaction with the semiconductor material, as shown in Figure 13. [6]

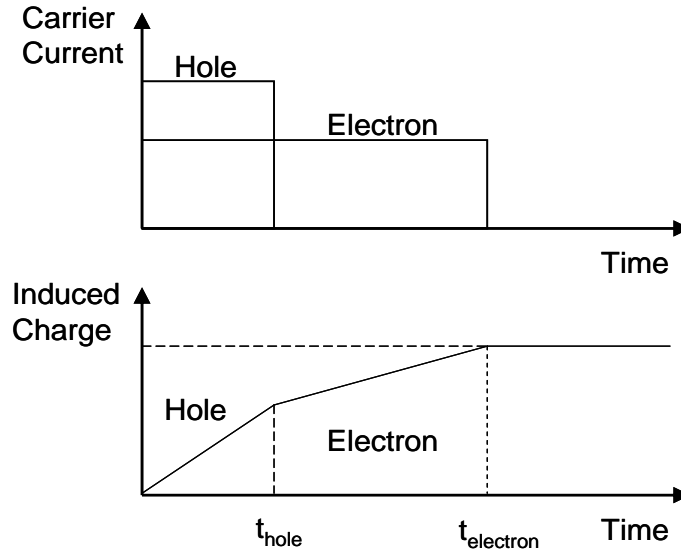


Figure 13. The top plot diagrams hole and electron migration current as a function of time. The bottom plot shows the collection of the holes and electrons and their contributions to the induced charge (not to scale) [6:367].

Several models have been developed to simulate pulse shapes in planar Ge detectors. Knoll [6:421] and Alberigi Quaranta et al [39] modeled these pulses by examining how charge carriers moved through the detector material. From Knoll's model, the energy absorbed by the motion of a charge, in this example, a positive charge; though a potential difference is given by:

$$dE = -q_o d\phi \quad (11)$$

where dE is the energy absorbed, q_o is the positive charge and φ_o is the potential difference. Since an electric field results from a difference in electrical potential, the electric field is defined as the change in potential as a function of distance:

$$\mathcal{E}(x) = -\frac{d\varphi(x)}{dx} \quad (12)$$

where $\mathcal{E}(x)$ is the electric field and x is distance. Substituting and simplifying reduces the expression of change in energy absorbed per unit distance as:

$$\frac{dE}{dx} = q_o \mathcal{E}(x) \quad (13)$$

Assuming the sides of the planar material to which the charge collecting electrodes are attached are parallel and the equipotential surfaces are uniformly spaced planes parallel to the electrodes, then the constant electric field intensity \mathcal{E} is:

$$\mathcal{E} = \frac{V}{t} \quad (14)$$

where V is the voltage across the electrodes on the sides of the detector and t is the distance between the electrodes, or the thickness of the detector. Substituting in Equation (13), the change in energy absorbed as a function in the change distance or ΔE can be expressed as:

$$\Delta E = q_o \frac{V_o}{t} \quad (15)$$

Integrating over a distance traveled, the energy absorbed as a result of the motion is:

$$\Delta E = \int_{x_o}^{x_1} q_o \frac{V_o}{t} dx = q_o \frac{V_o}{t} (x_1 - x_o) \quad (16)$$

where x_o is the initial location and x_l is the distance traveled. The voltage of the signal describing the motion of the charge, V_R , is simply a function of the energy required to move the charges, which is a function of the capacitance, C , of the detector material and the applied voltage V_o and is expressed as:

$$V_R = \frac{E}{CV_o} \text{ or } \Delta V_R = \frac{\Delta E}{CV_o} . \quad (17)$$

Substituting into Equation (16),

$$\Delta V_R = \frac{q_o}{C} \frac{(x_l - x_o)}{t} . \quad (18)$$

Since charge, Q , is simply CV , induced charge can be deduced as:

$$\Delta Q = C \Delta V_R = q_o \frac{(x_l - x_o)}{t} . \quad (19)$$

Equation (19) simply expresses the induced charge for one type of carrier, either the electrons or the holes. The complete charge collection would sum the induced charge for both types of carriers and would resemble:

$$\Delta Q_{total} = q_o \frac{((x_l - x_o)_{electrons} + (x_l - x_o)_{holes})}{t} . \quad (20)$$

The above pulse formation and modeling for a standard semiconductor can be applied to a segmented detector. The current associated with migration of the charge carriers in the electric field induces charge in the collecting electrode. For a strip detector, a transient current is induced in electrodes other than the collecting electrodes. If a hole or electron is formed a large distance from the collecting electrode, relative to the thickness of the detector, effects of the induced charge can be distributed over several electrodes. As a charge carrier migrates closer to the collecting electrode in its path, the

contribution of the induced charge in that electrode increases, and the contribution of induced transient charge in the adjacent electrodes decreases [40]. This trend continues until the carrier is collected by the collecting electrode in the carrier's path and results in a net-charge collected. No net charge is collected on the adjacent electrodes, since they do not collect any carriers. The charge collection strip which collects all of the holes and the strip that collects all of the electrons produced by the primary event accurately describe the energy of the primary fast electron resulting from the photon's interaction with the semiconductor material [6].

The transient signal observed in the adjacent electrodes, with no net-charge collection, is useful for determining the position of the primary interaction event across the width of the charge collecting electrode. Cooper et al [41] observed this while utilizing a double-sided Ge strip detector with 5-mm thick electrodes to construct and characterize a small-animal Positron Emission Tomography (PET) system. Figure 14 displays the transient and full-charge pulse observed from a single event in all five strips. Using the relative area of the transient signals in adjacent strips to the left and the right, Cooper et al was able to triangulate the photon's interaction with the detector material to within 1 mm^3 in the charge-collecting electrode, even though the electrode strips of the system were 5-mm wide.

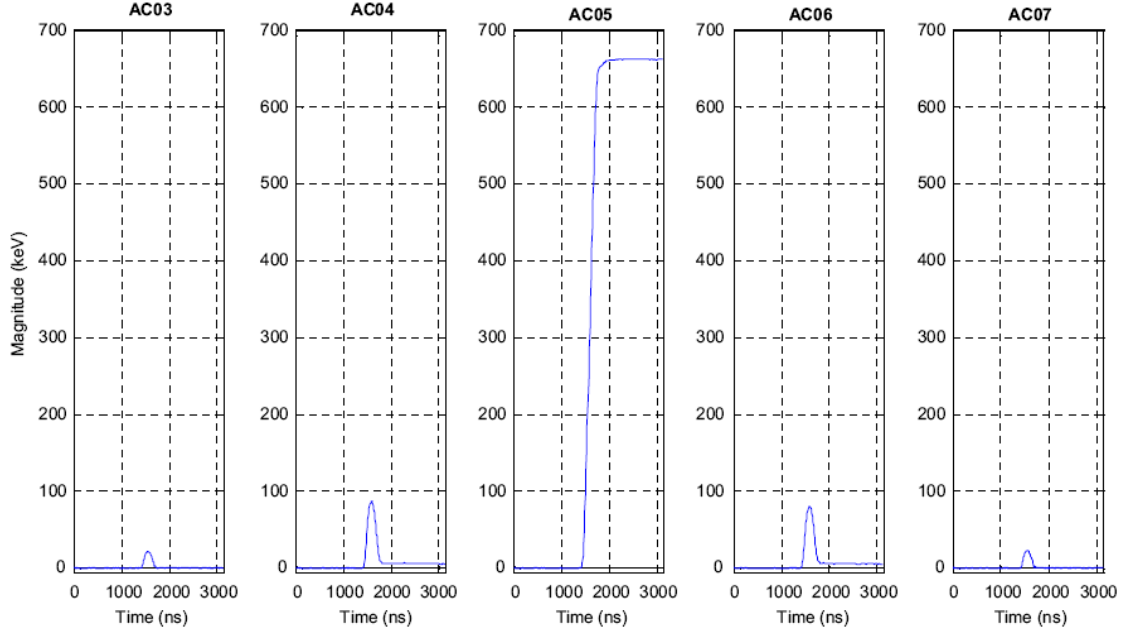


Figure 14. Transient charge (AC03, AC04, AC06, and AC07) and full-charge (AC05) signals from 662-keV photon interaction within Cooper et al’s detector [41].

While using transient charges to triangulate position in segmented detectors seems promising, a potential concern, however, is charge sharing between adjacent electrode strips. Charge sharing between adjacent electrode strips in segmented semiconductor detectors can be significant for ionizing events near strip boundaries. Even though the tracks of the electrons produced from a photon’s interaction with the semiconductor material is relatively short, the electrons and holes created in the track may be collected by more than one electrode on the same side of the crystal face. As a result, collection of charge carriers for full-energy events occurs on two strips. Amman and Luke [42] and Inderhees et al [43] demonstrated that summing the charge collection of carriers over adjacent electrodes in coincident events close to their boundaries efficiently recovered most of the energy of the event. They observed that the summation over the charge

collection strips did not fully recover the photon's energy and a correction factor was modeled to compensate for that trend. Another important observation Amman and Luke noted was charge-sharing between strips was dominated by shallow interactions in regions corresponding to strip gaps on the opposite side of the detector that was irradiated. They associated this with the long drift times towards the opposite face of the detector. Rossi et al [44] further demonstrated that the probability of charge-sharing is a function of photon energy and the location of energy deposition relative to the electrode's edge. They concluded that charge-sharing is statistically negligible, except near the boundaries of charge collection strips and for events located within the gap between electrodes.

2.8 Pulse Shape Analysis

A signal pulse, resulting from the induced charge, begins its development once the charge carriers produced within the semiconductor material begin to migrate and ends once the last of the carriers are collected on the electrode. This is when the maximum pulse height is achieved. The time necessary to collect the charge carriers is primarily a function of the detector material itself and is dependent on the mobility of the charge carriers in that material and the applied potential across the width of the detector. This collection time correlates to the leading edge or rise time portion of the signal pulse. While rise times vary with semiconductor material, the rise time for most semiconductor detectors is on the order of 100 nsec [6:385]. The decay of the pulse is the trailing edge of the signal pulse when the pulse falls back to zero. This portion of the pulse is a function of the time constant of the charge collection circuit, typically dominated by the

preamplifier in the circuit, although the inherent capacitance inside the detector plays a role. For accurate energy applications where complete charge collection is paramount, the time constant of the charge collection circuit is usually much larger than the charge collection time. As a point of reference, an Ortec Model 113 preamplifier has a fall time constant, the trailing edge of the pulse, of 50 μsec [45]. Figure 15 shows a hypothetical pulse shape resulting from the combination of the rise time and trailing edge from a HPGe detector.

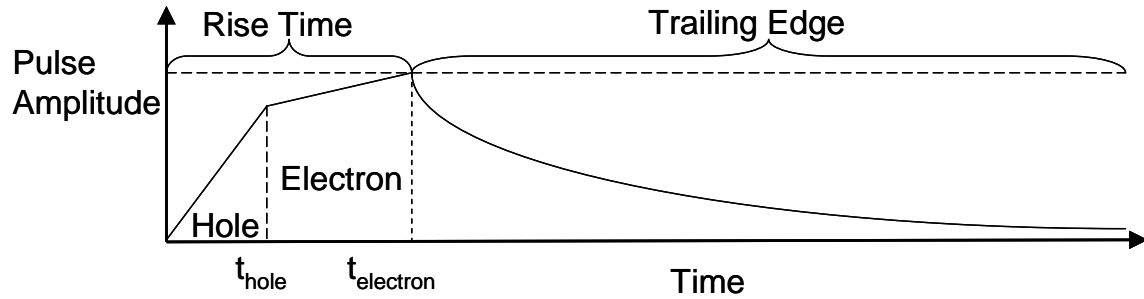


Figure 15. Hypothetical pulse shape from a HPGe detector (not to scale).

The signal pulse's leading edge shape is therefore a function of the migration time of the charge carriers. Assuming the mobility of electrons and holes remains constant throughout the material, the migration time of the charge carriers from the location of their origin to the charge collecting electrode is a function of the distance traveled through the thickness of the semiconductor material in planar geometry. As a result, by analyzing the rise time, i.e. pulse shape analysis, sufficient timing resolution of the leading edge of the pulse could allow for determination of the depth at which the carriers originated. Several articles examined this phenomenon for planar and coaxial Ge

detectors [46], [47], [48], [49], and [50], and concluded that the variations in the leading edge of the pulse shape can be analyzed and characterized to determine the depth in the crystal where the primary event occurred.

In order to achieve spatial resolution on a segmented detector, however, the critical parameter is the event's lateral position relative to the detector face and not its depth. Cooper et al [41] demonstrated the ability of achieving 1 mm² spatial resolution in the x-y plane of the detector surface by examining the transient charges' area and shape. They calculated the asymmetry of the area under the transient charge, and showed how the distribution of the asymmetry for a specific location relative to the electrode edge changed as the interaction location was changed. The asymmetry parameter, A, was calculated by:

$$A = \frac{Q_{left} - Q_{right}}{Q_{left} + Q_{right}} \quad (21)$$

where Q_{left} and Q_{right} refer to the areas underneath the transient charge pulses for the electrodes to the left and right of the full-charge electrode, respectively. The distribution of the asymmetry parameter for a single location is located in the left portion of Figure 16 and the distribution as the location is shifted in increments of 1 mm in the right portion. It is clear that the image charge asymmetry distribution shift is a function of location and can be used to improve spatial resolution.

Additionally, Burks et al [51] observed transient signals on all charge collection strips, with the closest neighboring strips producing the largest signals. They observed mostly unipolar signals like other investigators, but they also observed sporadic bipolar signals. They attributed the bipolar signals to partial cancellation of electron and hole

contributions to the transient signal for interactions that occurred far from the full-charge collection strip. They also developed a useful calibration tool derived from a simple electrostatic model to characterize the behavior of the unipolar-only transient signals as a function of depth in the crystal. Burks et al showed there was a linear relationship between the difference of the transient signal areas in the adjacent strips and the depth of energy deposition. Their method could prove useful to triangulate three-dimensional event locations.

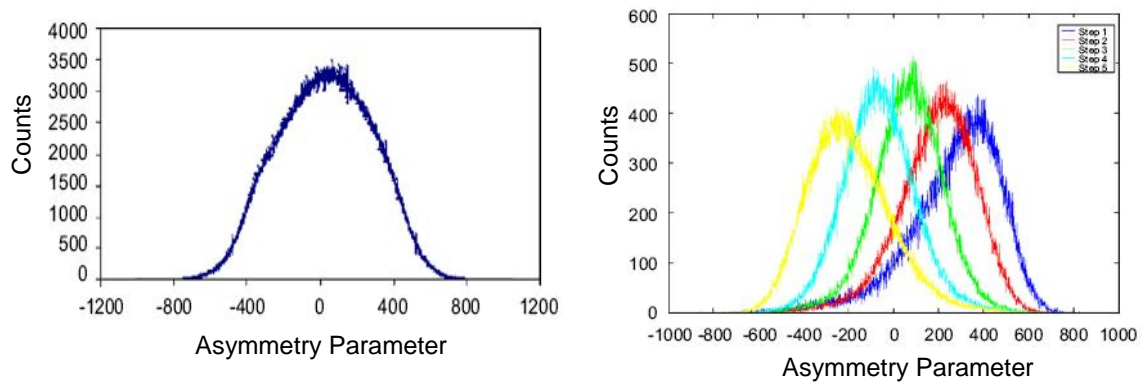


Figure 16. Left: Image charge asymmetry parameter distribution for an event location relative to the electrode. Right: Image charge asymmetry parameter distribution as a function of an event location relative to the electrode. [41]

Techniques incorporating transient charges to determine location typically relied on a relative measure of transient charges on charge collection strips on both sides adjacent to the full-charge collecting electrode. Therefore, edge strips on the detector surface cannot be used for location. A recent method by Cooper et al [52], used a parameter which was defined by the energy deposited from the photon's interaction with the detector material, the rise time components corresponding to the electron and hole

collection times and the area of a single transient charge on either side of the full-charge collecting strip. Then, by determining the depth of the interaction, the lateral location was triangulated in the full-charge collecting electrode. Cooper et al was able to effectively demonstrate this relationship and triangulate the event's location to within 1 mm^3 , similar to the results they observed using transient charges on both sides adjacent to the full-charge collecting strip. Now, with appropriate electronics, all strips can be utilized to triangulate lateral position using either one or two adjacent transient charges.

2.9 Spatial Resolution

The spatial resolution of a strip detector reflects the uncertainty in locating the charge deposition of a detected event. For this research, the spatial resolution was degraded by several mechanisms: by error in the measurement of transient signals, determining the location from those signals, and variability in the charge deposition physics, as discussed in Williams et al [53]. Error associated with the measurement of the transient signal is significantly influenced by the sampling rate of the electronics suite for the short-lived transient signals. Variance associated with the method to derive location from the transient charges is the inherent variability in correlating the transient signal measurement with event location. The uncertainty in event location due to the charge deposition physics results from the inherent variability of electron-hole charge distributions produced by competing deposition mechanisms.

To illustrate the variability in location measurement due to the charge deposition mechanisms for 511-keV annihilation photons incident normal to the detector surface, three deposition events within a volume of detector material with charge collection strips

on both the front and rear of the detector surfaces were considered. First, photoelectric absorption of the incident photon produces charge dispersion due to random asymmetry of the ion pair distribution produced by the slowing recoil electrons [54]. The second deposition mechanism, Compton backscattering of the incident photon followed by a photoelectric event produces negligible variability in the charge dispersion. The energy of the Compton scattering corresponds to the most probable single-scattering full-energy event [55]. Lateral spreading of this charge distribution by diffusion during charge mobility introduces some variability, especially near strip edges [56]. For backscatter Compton events with scattering angles greater than 90° , the energy of the recoil electron is 343 keV and the energy of the Compton scattered photon is 171 keV, which happens to be the energy for which the Compton and the photoelectric cross sections in germanium are approximately equal [6]. Above this energy, the probability of depositing energy in the detector by photoelectric absorption decreases dramatically compared with Compton scattering. The third deposition mechanism considered was Compton scattering at photon scattering angles smaller than backscatter, which can significantly degrade spatial resolution. The variability of distance through which the scattered photon penetrates before producing an ion pair track by a photoelectron (or another scatter event) can produce significant charge asymmetry around the initial Compton scatter event. The charge deposition asymmetry due to the variable penetration of Compton scattered photons may significantly contribute to the variance in measuring the event location. However, detection of these events are rare especially if the mean free path of the Compton scattered photon, which is on the order of 1.3 cm for a 170-keV scattered photon [57], is larger than the most planar HPGe detector thicknesses. In this case, the

probability of the photon Compton scattering out of the detector without depositing its full energy is significant. Because the energy dependence of the photoelectric cross section is much greater than that for Compton scattering, this charge deposition asymmetry is dominated by photon absorption. Based on these three deposition events, it follows that the uncertainty in locating the charge deposition of a detected event is minimally affected by the variability in the charge deposition physics and dominated by the error in the measurement of transient signals and determining the location from those signals. This allows development of the following model to quantify the spatial resolution of a detection system.

Nothing was found in the literature to model data from a pixelated, position-sensitive detector in order to derive and quantify the spatial resolution; however, a model developed for astronomical applications provided a good starting point. Bailey and Sparks [58] developed a model based on a 2D Gaussian point-spread function with a circular aperture which they applied to the light distribution in the center of a galaxy. The novelty of this derivation is the model reduced the 2D function to a single integral as a function of the dispersion, σ . Their modeled dispersion is analogous to the spatial resolution of the detection system this research effort hopes to quantify. The model Bailey and Sparks developed required the system's location-dependent seeing-convolved profile, tailoring the model to their astronomical application, which made the model unsuitable for this application. Their approach, however, did aid in the development of the model that follows.

First, starting with the 2D Gaussian function in Cartesian coordinates located away from the origin:

$$G(x, y; x_o, y_o) = \frac{1}{2\pi\sigma} \exp \left\{ -\frac{1}{2\sigma^2} [(x - x_o)^2 + (y - y_o)^2] \right\} \quad (22)$$

where x_o and y_o are the coordinates of the distribution's origin and σ is the variance.

Then, transforming Equation (22) to polar coordinates, the function translates to:

$$G(r, \theta; r_o, \theta_o) = \frac{1}{2\pi\sigma} \exp \left\{ -\frac{1}{2\sigma^2} [r^2 + r_o^2 - 2r_o r \cos(\theta - \theta_o)] \right\}. \quad (23)$$

To determine the frequency of events (I) of the Gaussian distribution as a function of radius (r), the following double-integral was evaluated.

$$I = \int_0^{2\pi} \int_0^{r_a} G(r, \theta) r dr d\theta. \quad (24)$$

$I(r_o)$ is the radial intensity distribution for distance r_o due to uniform illumination of a circular aperture of radius r_a with both radii centered at zero. To evaluate Equation (24), let

$$\xi = \frac{r}{\sqrt{2}\sigma}, \lambda = \frac{r_a}{\sqrt{2}\sigma}, \text{ and } \alpha = \frac{r_o}{r_a}. \quad (25)$$

Then, substituting Equation (23) into (24), the distribution function I reduces to

$$I = \frac{1}{\pi} \int_0^\lambda \int_0^{2\pi} \exp -[\xi^2 + \alpha^2 \lambda^2 - 2\xi \alpha \lambda \cos(\theta - \theta_o)] d\theta d\xi. \quad (26)$$

Assuming the illumination over the aperture is axi-symmetric, there is no angular, θ_o , dependence. Using the integral representation of the zero order modified Bessel function,

$$I_o(z) = \frac{1}{\pi} \int_0^\pi \exp z \cos \theta d\theta \quad (27)$$

Equation (27) is reduced to

$$I(\alpha, \lambda) = 2e^{-\alpha^2 \lambda^2} \int_0^\lambda e^{-\xi^2} I_o(2\alpha \lambda \xi) \xi d\xi. \quad (28)$$

Replacing I_o with the series representation and integrating term-wise results in

$$I(\alpha, \lambda) = 2e^{-\alpha^2 \lambda^2} \sum_{k=0}^{\infty} \frac{\alpha \lambda^{2k}}{k!} \int_0^\lambda e^{-\xi^2} \xi^{2k+1} d\xi. \quad (29)$$

The final integral is expressed in terms of incomplete gamma functions to produce

$$I(\alpha, \lambda) = 2e^{-\alpha^2 \lambda^2} \sum_{k=0}^{\infty} \frac{(\alpha \lambda)^{2k}}{k!} \Gamma(k+1, \lambda^2). \quad (30)$$

The incomplete gamma function for integer values of k can be written as

$$\Gamma(k+1, \lambda^2) = 1 - e_k(\lambda^2) e^{-\lambda^2} \quad (31)$$

with $e_k(x) = \sum_{m=0}^k x^m / m!$. Finally, after recognizing the exponential series, and

substituting, the function reduces to

$$I(\alpha, \lambda) = 1 - e^{-(\alpha^2 + 1)\lambda^2} \sum_{k=0}^{\infty} \frac{\alpha \lambda^{2k}}{k!} e_k(\lambda^2). \quad (32)$$

This function is used to fit the experimental count distribution from a pixelated detector to quantify its spatial resolution. The novelty is the model is reduced to two parameters, λ and α , which are a scaled measurement of the radial location and a scaled measure of spatial resolution, respectively.

Application of Equation (32) to experimental results relies on three assumptions. First, the experimental distributions and variances are the same in both axial directions. Second, the experimental distribution is uniform across the projection of the circular aperture. The third assumption is that a single Gaussian distribution accurately describes

the spatial resolution which is a convolution of the physics and error associated with measuring and processing the transient charge. These assumptions were validated experimentally and discussed in Chapter 4. Within this context, fitting (32) to the experimental count distribution produces a measure of the standard deviation corresponding to the spatial resolution point for a pixilated detector applied to positron annihilation radiation.

That concludes the underlying physics associated with the techniques used to measure the e^-e^+ momentum distributions. Next, the materials that will be measured are discussed.

2.10 SiC Material Characteristics

SiC is a wide band-gap semiconductor becoming more commonly used due to its innate crystalline structure characteristics, making it suitable for use in devices in harsh environments. The crystalline structure of SiC results from the tetrahedral arrangement of either a Si or C atom bonded to four C or Si atoms, respectively. The Si-C bond is 88% covalent and 12% ionic with a length of 1.89 Angstroms, where the C atom is more electro-negative than the Si atom [1]. SiC's crystalline structure is arranged by the stacking of two single layers of Si and C atoms. SiC has 170 variations of the stacking sequence of these double layers, known as polytypes [59]. The most common polytypes of SiC, using the Ramsdell notation, is 3C, 4H and 6H SiC, of which, all three have distinct stacking sequences of layers described using three relative stacking positions, labeled A, B, and C. The following figure visually depicts the structure for each polytype's layering structure.

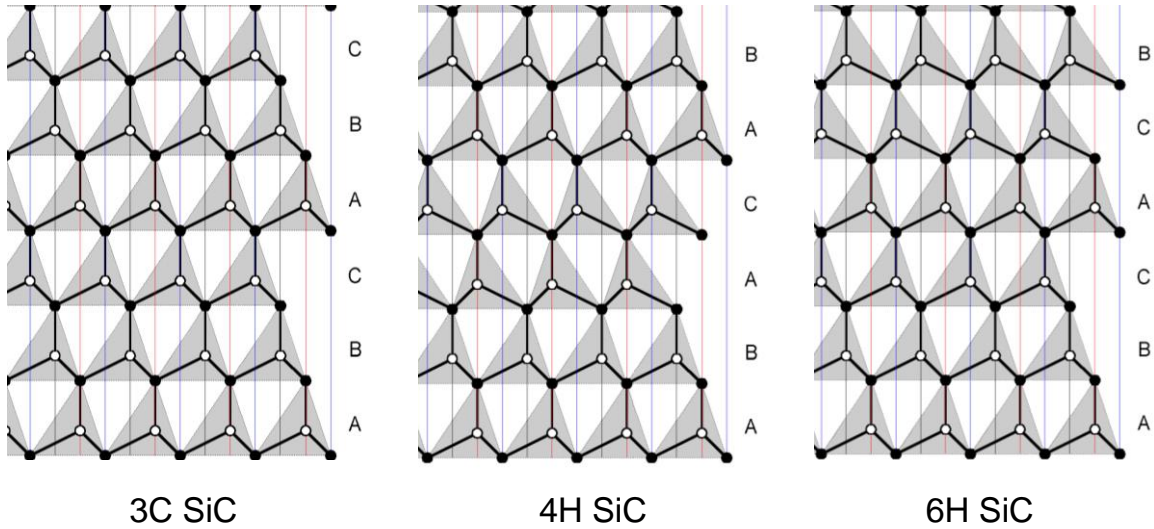


Figure 17. Single layer tetrahedral bond structure for SiC polytypes [60].

The bravais lattice type for the three polytypes vary. 3C SiC uses a cubic Bravais lattice type; whereas, 4H and 6H SiC are of a hexagonal type with varying degrees of hexagonality. Hexagonality is defined by Harris [1] as the ratio of the number of biplanes with hexagonal coordination to the total number biplanes in the layering sequence of the SiC polytype. Below is a table listing some basic physical properties of these three polytypes of SiC.

Table 2. Physical properties of SiC polytypes [1].

Polytype	Stacking Sequence	% of Hexagonality	# of Atoms per Unit Cell
3C	ABC	0	2
4H	ABAC	50	8
6H	ABCACB	33	12

For the most part, all three polytypes can be n-type or p-type doped. Nitrogen and phosphorous have been successfully used for n-type doping with carrier concentrations as high as 10^{20} cm^{-3} . Aluminum, boron, gallium, and scandium have been demonstrated as

p-type dopants with carrier concentrations as high as 10^{20} cm^{-3} , as well. It should be noted, however, that even though p-type doping has been relatively successful, it is difficult to perform and usually requires a high-temperature anneal. [2]

Defects in SiC can result in undesired performance and characterization of these defects is an area of interest to the community. The 3DPAMM technique this research developed will investigate the influence of deep-level material defects on the momentum distribution in the SiC. The primary defects found in SiC are vacancies, interstitials, and antisites [60]. These defects can be induced by a variety of mechanisms like electron, proton, neutron and ion irradiation. When SiC is bombarded with neutrons, the neutrons collide directly with the Si and C nuclei. If enough energy is imparted to the nucleus due to the collision, the nucleus can move from its original location in the lattice to a new location, thereby producing a vacancy and an interstitial. Ions, on the other hand, can be implanted into SiC, and if the energy is large enough, create similar defects listed above in a single track as the ion slows down. Additionally, the ion may become lodged within the lattice structure and perturb the local electronic environment, to which a diffusing positron can be sensitive, depending on distance between the ion and diffusing positron. This research will investigate the effects of oxygen ion implantation into 6H SiC.

2.11 Oxygen in SiC

Few studies have been conducted to investigate O defect characterization in SiC. Most studies on oxygen in SiC related to either O impurities resulting from the SiC growth process or by surface or layer oxidation of the SiC. Vlaskina et al [61] examined O effects in 4H and 6H SiC that they attributed to impurities used in device fabrication to

make junctions, contacts and Shottky barriers. They annealed the SiC samples in oxygen at 1700°C for two hours. Using Hall effect measurements, they were able to determine the electrical characteristics of the samples as a function of the diffusion of the O from the annealing. They observed SiO₂ effects resulting from the annealing but they did not note any O atom effects.

Next, Dalibor et al [62] examined O implanted 6H SiC chemical vapor deposition epilayers using Hall effect, admittance spectroscopy, deep level transient spectroscopy and photoluminescence. They determined the implanted O formed two types of O-related centers: shallow donors in the energy range of 129-360 meV below the conduction band edge and deep acceptor-like defects at 480, 560 and 610 meV.

Finally, Bermudez [63] studied the room temperature adsorption of pure O₂ on the surface of SiC using x-ray photoemission and electron energy loss spectroscopies. He concluded the O₂ did not adsorb well when compared to similar conditions on Si samples. While this research investigated O in SiC, O atom interactions with the Si and C atoms in the SiC lattice were not studied.

Research relevant to an O atom interaction with the Si and C atoms in the SiC lattice was performed by Duan. Duan [64] calculated the optimized geometry for an O atom interstitially residing inside of bulk SiC using Surface Integrated Molecular Orbital / Molecular Mechanics (SIMOMM). The SIMOMM method is a two step process which first computes electrostatic forces of large molecular clusters of the bulk crystal onto a small molecular cluster using molecular mechanics (MM) and then uses those forces as the boundary conditions to solve for the wavefunctions of the small cluster using quantum mechanical (QM) calculations carried out at the Møller-Plesset perturbation

(MP2) theory level. Duan determined the O atom infuses into the Si-C bond thereby increasing the distance between the Si and C atoms. Additionally, he observed the 180° Si-C bond reduced to 171° with the infusion of the O to form Si-O-C. These results were used during the analysis of the O^+ implanted 6H SiC measured using 3DPASS.

2.12 Investigation of SiC Using PAS Techniques

Several papers have documented PALS, DBAR and ACAR measurements on 6H SiC. These published findings were compared to the PALS, DBAR and ACAR results from using the 3DPAMM technique in Chapter V. First, Lam et al [65] compiled a comprehensive list of lifetimes for the bulk, V_C , V_{Si} , and the $V_{Si}V_C$ divacancy from numerous sources in the literature detailing PALS measurements on 6H SiC. Table 3 lists the lifetimes for the 6H SiC components outlined from both predictions from theoretical calculations and reported experimental results. This compilation was useful for comparison to lifetime measurements on virgin and ion-irradiated 6H SiC samples in this research.

Table 3. 6H-SiC Bulk, V_C , V_{Si} , and $V_{Si}V_C$ theoretical and experimental lifetimes.

Component	Method Determining Lifetime	Lifetime (psec)
Bulk	Theoretical Calculation	141
	Experimental	136-148
V_C	Theoretical Calculation	153
	Experimental	152-160
V_{Si}	Theoretical Calculation	194
	Experimental	175-260
$V_{Si}V_C$	Theoretical Calculation	214
	Experimental	225-232

Few documents were found in the literature addressing DBAR measurements in 6H SiC. Only one document was found to provide the DB lineshape for un-irradiated 6H SiC. Rempel et al [66] investigated vacancy-type defects in 6H SiC, diamond and Si using two HPGe detectors with an energy resolution of 1.2 keV at 511 keV to measure the 2D DBAR spectra. They sandwiched their ^{22}Na source of unknown activity between two identical samples. Their un-irradiated DB lineshape for 6H SiC is shown in Figure 18. They observed a greater than 10^4 improvement in peak-to-background ratio. Rempel et al was able to use the DB lineshape and subsequent PALS analysis to distinguish C vacancies observed at electron energies below 500 keV and Si divacancies produced from the electron irradiation at energies above 2.5 MeV.

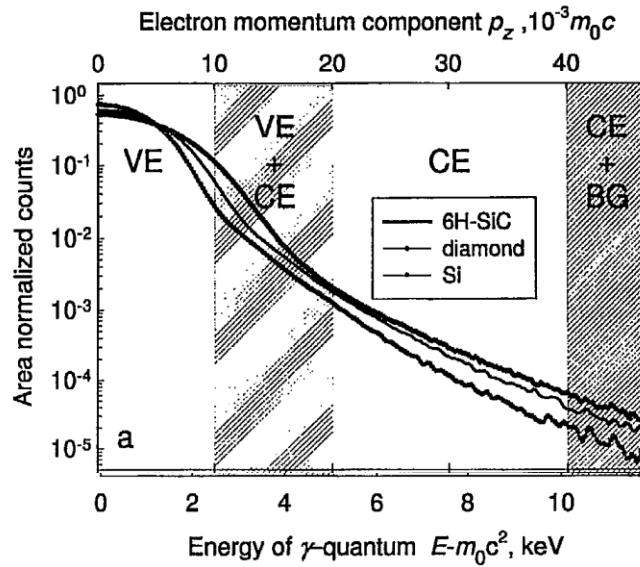


Figure 18. Rempel et al's DB lineshape for 6H SiC, diamond and Si.

Only one paper was found to measure and present ACAR spectra for 6H SiC. Kawasuso et al [67] collected 2D ACAR spectra for virgin and electron-irradiated 6H SiC samples. The 6H SiC they used was orientation (0001) and nitrogen-doped to a carrier density of $1 \times 10^{17} \text{ cm}^{-3}$. They measured lifetimes and 2D ACAR spectra on as-grown samples and samples irradiated with 2-MeV electrons. Before the irradiated samples were measured, they were annealed in dry argon at 1000°C for 30 min. Kawasuso et al obtained a bulk lifetime of 140 psec on the virgin sample and measured two lifetime components on the electron-irradiated samples: 110 and 210 psec. 2D ACAR spectra were then collected using a spectrometer composed of two Anger cameras each located 7 m from the source/sample, resulting in an angular resolution of $\sim 1 \text{ mrad}$. First, two orientations of the virgin samples were measured: the planes perpendicular to (0001)-(1100) and (0001)-(1120). Then, ACAR spectra were collected for the annealed, electron-irradiated samples. The resulting spectra are shown in Figure 19. They compared these spectra with a theoretical prediction of the electron momentum density for a defect-free 6H SiC lattice and a defect complex composed of a carbon vacancy, a carbon antisite ($V_C C_{Si}$) and a silicon vacancy nitrogen pair ($V_{Si} N$) along the same orientations listed above. The $V_{Si} N$ were visibly indistinguishable from the $V_C C_{Si}$ defect complex. The $V_C C_{Si}$ calculations are displayed in Figure 20. As a result of the measured lifetimes and anisotropies present in the 2D ACAR spectra, Kawasuso et al concluded the dominant defects produced from the 2-MeV electron-irradiation were $V_C C_{Si}$ and $V_{Si} N$.

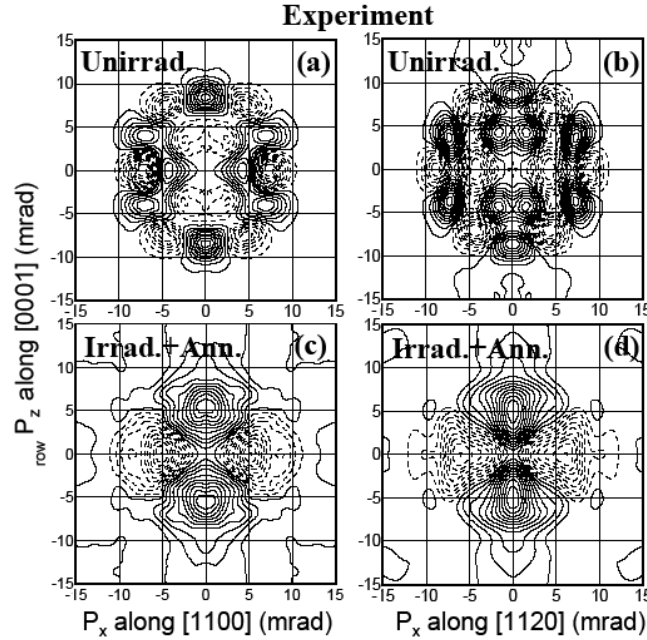


Figure 19. 2D ACAR spectra for 6H SiC for (a) virgin sample for the plane perpendicular to (0001)-(1100), (b) virgin sample for the plane perpendicular to (0001)-(1120), (c) electron-irradiated sample for the plane perpendicular to (0001)-(1100) and (d) electron-irradiated sample for the plane perpendicular to (0001)-(1120).

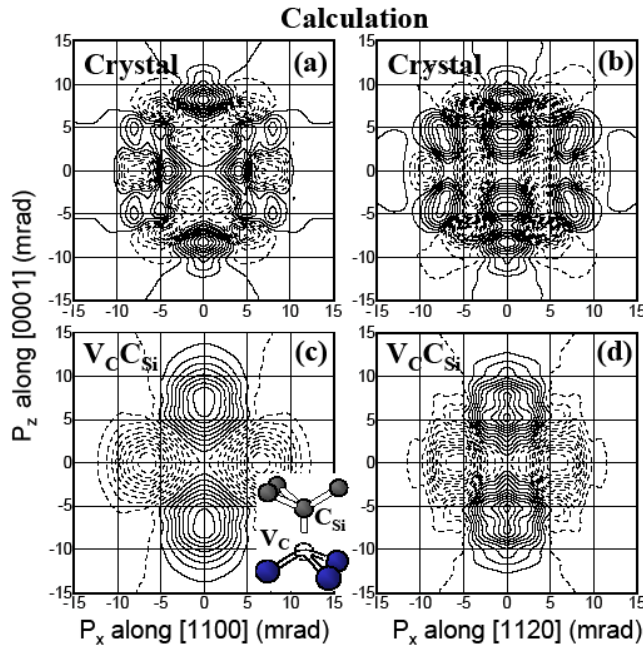


Figure 20. Theoretical prediction for 6H SiC for (a) virgin sample for the plane perpendicular to (0001)-(1100), (b) virgin sample for the plane perpendicular to (0001)-(1120), (c) $V_C C_{Si}$ defect complex in the plane perpendicular to (0001)-(1100) and (d) $V_C C_{Si}$ defect complex in the plane perpendicular to (0001)-(1120).

In the virgin 6H SiC ACAR spectra, the direction of the high-frequency momentum features, denoted by the peaks at the (7,4), (7,-4), (-7,-4), (-7,4), (0,8) and (0,-8), correlate well with the direction of the covalent bonds between the Si and C in the SiC when the correct projection of the lattice is overlaid on the ACAR spectra. This indicates the direction of perpendicular component of the e^-e^+ pair's momentum prior to their annihilation lies in the same direction of the bonding's projection between the atoms themselves. Therefore, ACAR spectra for 6H SiC with O atoms implanted in the lattice may be interpretable if this observation holds true for various orientations of the lattice structure. This is discussed more in depth in Chapter 5.

2.13 Investigation of Ion Irradiated SiC

A plethora of articles have examined defects induced by electron, proton, and photon irradiation on SiC using PAS techniques, but few were found to address ion irradiation. Three papers were found in the literature that examined ion implantation into 6H SiC using PAS techniques. In the first paper, Zhu et al [68] inspected near-surface vacancy-type defects in 5- μm thick 6H SiC samples from the implantation of He ions with energies ranging from 55 to 840 keV. Using a slow positron beam, they observed the trend of the DBAR spectral parameters, S and W, as a function of positron energy in the range of 1 to 35 keV and also as a function of the annealing temperature in an argon environment which ranged from as-implanted at room temperature to 1600°C. Zhu et al concluded that the He ion implantation produced predominantly vacancy-type defects. Additionally, they concluded that three annealing regions, annealing below 900°C, from

900 to 1600°C and above 1600°C. Each produced different sizes of the damage region and the size of the vacancy-type defects, themselves.

Uedono et al also [69] studied near-surface vacancy-type defects in 6H SiC samples, but they implanted 10^{13} and 10^{15} 150-keV O^+ and 200-keV N_2^+ ions. Using a slow positron beam from 0 to 50 keV, they observed the trend of the S parameter from the DBAR spectra as a function of positron energy and also as a function of annealing temperatures, which ranged from 200 to 1600°C, for 20 min in an argon environment, which. Analyzing the S parameter as a function of positron energy using the VEPFIT tool developed by van Veen et al [70], Uedono et al concluded the mean size of the vacancies they observed were approximately the size of a $V_{Si}V_C$ divacancy for all three ion doses. They noted four regions of vacancy-type defect agglomerations due to the migration of mono and divacancies due to the N_2^+ ion implantation. The agglomerations were suppressed when subsequently implanted with O^+ ions which they accredited to the formation of vacancy-oxygen complexes. This implied the oxygen suppressed the formation of secondary defects in the ion-implanted SiC.

The paper by Gentils et al [71] addressed ion implantation into 6H SiC examined by PAS techniques and sub-surface defects in 6H SiC irradiated with 20-MeV Au ions. The SiC samples were irradiated with 10^{12} , 10^{13} , 10^{14} , and 10^{15} -cm⁻² ions. The S and W DBAR spectral parameters were examined as a function of positron energy in the range of 1 to 25 keV. They concluded two types of defects resulted from the Au ion irradiation: $V_{Si}V_C$ divacancies, which dominated in samples irradiated at fluences below 10^{13} -cm⁻² ions and nano-clusters of Si which dominated at fluences greater than 10^{14} -cm⁻² ions.

2.14 Investigation of Cu Using PAS Techniques

Cu has been extensively studied using all three relevant PAS techniques. Therefore, the performance of 3DPASS was compared with results from comparable PAS systems' measurements on Cu. In contrast to the limited number of 6H SiC DBAR related publications, there is a plethora related to single-crystal Cu. For DBAR measurements in single-crystal Cu, Szpala et al [72] provided raw DBAR spectra for single-crystal Cu using a coincidence system composed of a HPGe detector and BiGeO scintillator detector. They acquired CDBAR spectra for Cu, Si, Sb, Ni and Ge, extracted the annihilation lineshape and computed ratio curves with spectra normalized to the Si data, shown in Figure 21. The novel aspect of the work by Szpala et al is two-fold. First, they degraded the resolution of their Ge detector to ascertain the influence on the extracted annihilation lineshape. Degrading their detector's energy resolution to 1.6 keV, (0.4 keV greater than the resolution for a standard HPGe at 511 keV) resulted in no statistical change in the annihilation lineshape. The second novel aspect was they provided the algorithm they used to smooth the annihilation lineshapes, which was not discussed in other CBAR papers found in the literature. Szpala et al performed a variable averaging where they averaged the counts over several channels on both sides of the averaged channel, if the statistical error in the frequency of counts at a given channel was greater than 3%. The channels used for the averaging were not re-used. Therefore, the spacing between energy values increased for larger energy values in the raw data shown in Figure 21a as a direct result of the variable averaging smoothing algorithm.

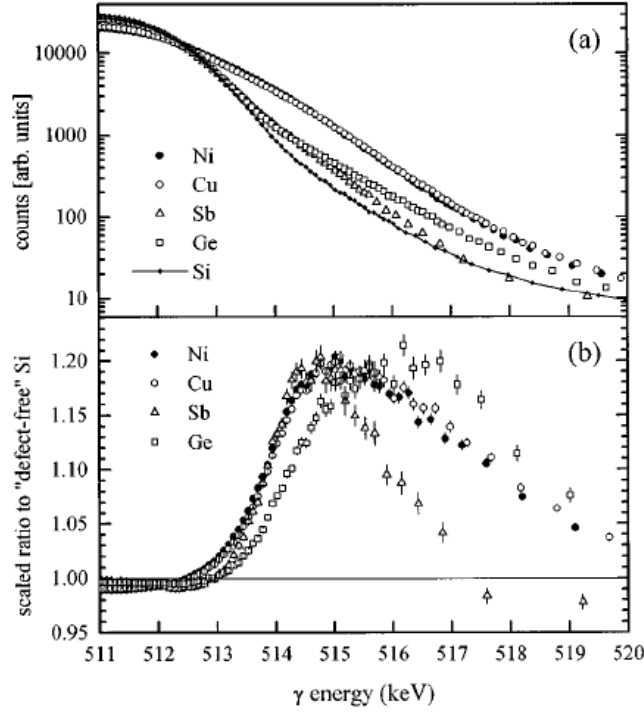


Figure 21. Top (a): Annihilation lineshape extracted from CDBAR spectra for Ni, Cu, Sb, Ge, and Si. Bottom (b): Ratio curves from annihilation lineshapes normalized to Si for Ni, Cu, Sb, and Ge.

Several papers addressed ACAR measurements for single-crystal Cu. For 2D ACAR Cu measurements, Howell et al [73] measured the near-surface electron momentum density of single-crystal Cu. Using 740 eV and 18 keV positrons, 2D ACAR spectra were collected in the (100) plane using a spectrometer consisting of two position-sensitive Anger cameras positioned 13.67 m from the source/sample, producing an angular resolution of 0.9 mrad. Figure 22 displays the 2D ACAR spectra for the single-crystal Cu.

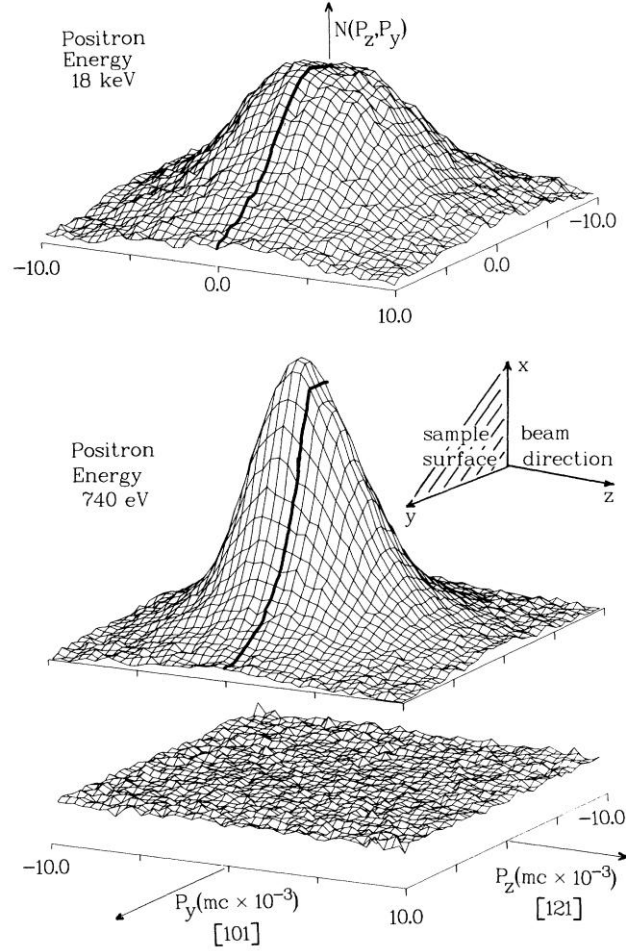


Figure 22. 2D ACAR spectra for single-crystal Cu, top: injected with 18 keV positrons, middle: injected with 740 eV positrons, bottom: background spectra.

Senicki et al [74] also measured the e^-e^+ momentum in single-crystal Cu using the 1D ACAR long-slit method. They used four sets of coincident detectors spaced 140 in from the sample, behind collimators with 1/8-in diameter holes. They acquired spectra for virgin and neutron irradiated (of unknown fluence) Cu. The 1D spectra for the (100) plane are shown in Figure 23. The 1D spectra were Gaussian-shaped with a smooth, featureless profile. The lack of features was due to the large contribution of annihilations with valence electrons which are negligibly affected by the core

polarization of the Cu atoms. The experimental data was compared to theoretical predictions made by using two different models (the Wigner-Seitz and crystal symmetry models) for positronic wavefunctions. The predictions did not compare well with the experimental results, attributed to the models' inadequate representation of the varying core electron contributions to the wavefunctions.

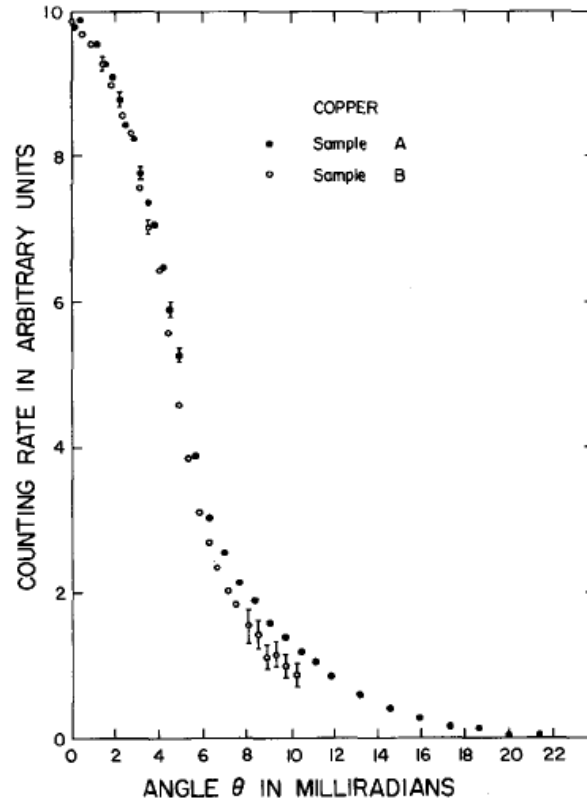


Figure 23. 1D ACAR spectra for (100) annealed, virgin Cu (sample A) and neutron-irradiated Cu (sample B) of unknown fluence.

Tanigawa et al [75] also measured the e^-e^+ momentum density of single-crystal Cu using the 2D ACAR technique. As-grown single-crystal Cu and samples bent to a radius curvature of 3 cm were analyzed with a 2D ACAR spectrometer containing a

series of $64\text{-Bi}_4\text{Ge}_3\text{O}_{12}$ detectors with an angular resolution of 0.5 mrad in one direction and 1 mrad in the other. Their results are similar to those presented by Howell and Senicki et al, with the exception of a neck feature at the top of the peak when the crystal orientation was (111). This neck feature is not present in the ACAR spectra for (100), (010), or (001) crystal orientations.

3 Equipment

3.1 Overview

Several key components were required to create a combined 2D ACAR and CDBAR spectrometer which will be discussed in this section. First, two position-sensitive detectors with the ability to fully scan a typical angular range used to perform coincident CDBAR and 2D ACAR is detailed. Second, the electronics suite which accepted the signals from the detectors and were capable of processing and transferring large amounts of data is discussed. Then, a vacuum chamber is presented which maximized the number of positrons reaching the sample material. Next, the sources and the samples used in the research and the source/sample configuration design, critical to ensure the maximum number of photons reach the detectors, are detailed. Finally, the shielding arrangement to reduce noise from scattering is discussed.

3.2 Position-Sensitive Semiconductor Detectors

Two position-sensitive detectors were used for this research, one manufactured by Ortec and the other by PHDS. They are referenced by the manufacturer.

3.2.1 Ortec Detector

One of the detectors used for this research is a two-dimensional, position-sensitive, single-crystal, planar HPGe semiconductor, double-sided strip detector (DSSD), manufactured by Ortec, serial number 42-WPAFB-01. The detector is 25-mm square and has 5, 25 x 5 mm charge collection strips on front and rear sides of the detector, orthogonal to each other. The front strips are horizontal and labeled F1 - F5

with F1 being the top strip and F5 the bottom. The rear strips are vertical and labeled R1 - R5 with R1 being the left-most strip and R5 the right. The orthogonal orientation of the front and rear strips effectively creates 25 pixels, with a total active surface area of 25 x 25 mm. The detector has an active depth of 9 mm. The layout of the detector and the charge collection strips is illustrated in Figure 24 below.

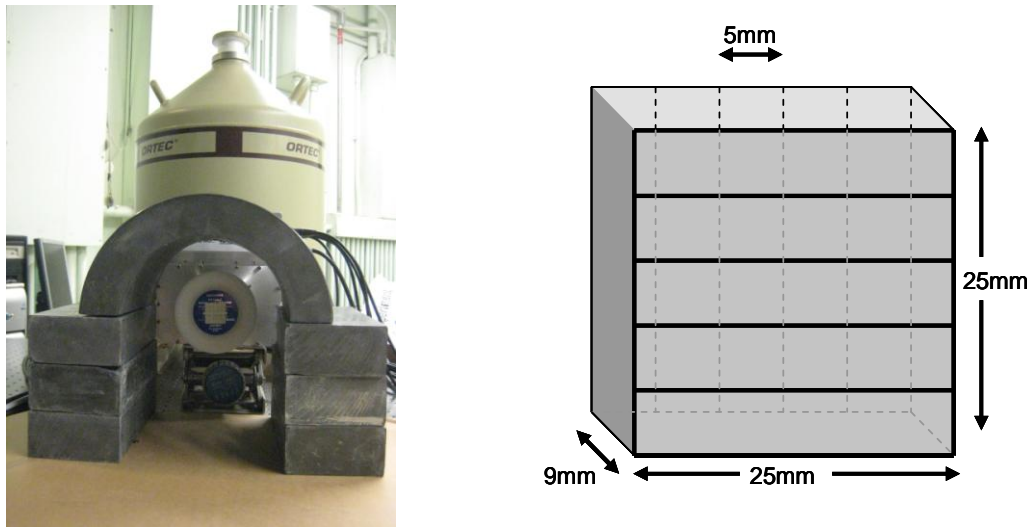


Figure 24. Left: Ortec HPGGe DSSD. Right: Ortec DSSD electrode layout (not to scale).

The face of the Ge crystal is located 10 mm behind the face of the detector, centered within the endcap diameter, which contains a 0.5 mm beryllium entrance window, as well as a 0.3 μm thick film of inactive germanium. The detector is normally operated at +1000 volts bias. The charge collection strips attached to the back face of the crystal are lithium and operate at +1000 V bias; whereas, the charge collection strips attached to the front face of the crystal are boron and operate at about +1 V. Each of the strips is electrically separated from one another. [76]

This detector, as well as the PHDS detector, is position-sensitive by measuring front and rear strip coincident events. If one of the front strips and one of the back strips detect an event coincident in energy and time, the orthogonality of the strips map the location of the interaction. As an example, if strip F2 (*F*ront strip) and strip R3 (*R*ear strip) both record an event within a specified coincidence timing window and are the same energy to within a small difference, then the intersection of the two strips is the location of the event, as illustrated in Figure 25 below.

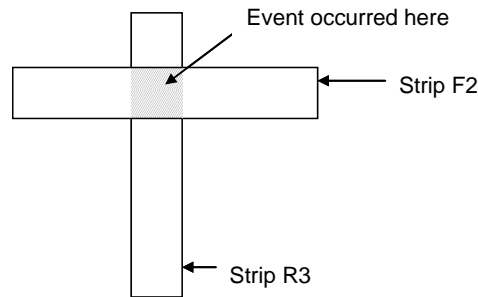


Figure 25. Event location using intersecting front and rear strips (not to scale) [76].

3.2.2 PHDS Position-Sensitive Semiconductor Detectors

The other detector used for this research is also a two-dimensional, position-sensitive, single crystal, planar HPGe semiconductor DSSD, manufactured by PHDS, serial number AFIT-01. The crystal is 9 cm in diameter and has an active depth of 11 mm. The detector has 16, 5-mm wide charge collection strips on each of the front and rear faces of the detector, orthogonal to each other. Since the crystal is curved, only the 8 center strips on each side have a length of 8 cm. The strips outside of these 8 center strips are shorter the further they are from the center of the crystal, effectively creating

220 pixels. The rear strips, denoted as the AC side, are vertical, and are labeled 0 - 15 with 0 being the left-most strip and 15 the right. The front strips, denoted as the DC side, are horizontal and are labeled 16 - 31 with 16 being the top strip and 31 the bottom. The layout of the detector and charge collection strips is illustrated in Figure 26.

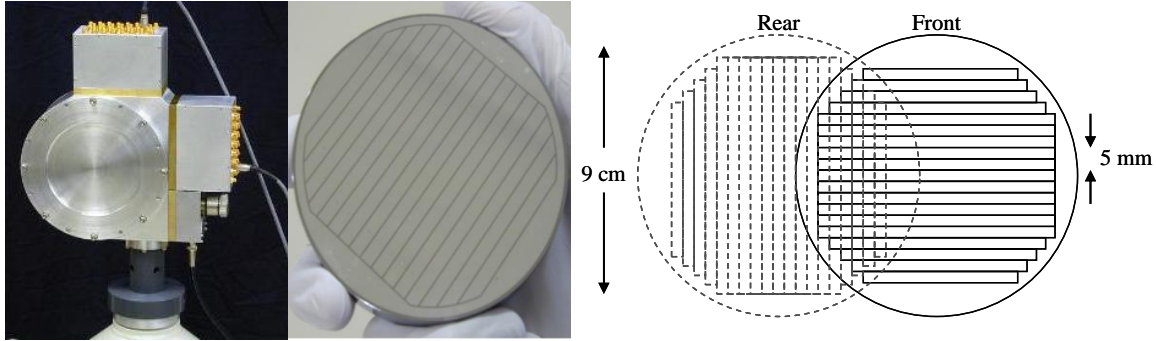


Figure 26. Photograph of PHDS detector sitting on LN₂ dewar. Middle: Photograph of PHDS detector's Ge crystal with electrode masking. Right: PHDS detector's electrode masking layout (not to scale).

The detector is normally operated at +700 V bias. The charge collection strips attached to the front and back face of the crystal are metallized, amorphous Ge with a thickness of $\sim 2 \mu\text{m}$. Each of the strips is electrically separated from one another. [77]

3.3 Electronics

Two different digital electronic suites are used in this research: the XIA digitizers using the CAMAC protocol and the self-contained Spec32 system. The Spec32 digital system was used to perform the simultaneous 2D ACAR and CDBAR measurement. The XIA digitizers were used to verify the results of the intrinsic functions built into the Spec32 system. Equipment settings and their description for the Spec32 used in this research are listed in Appendix A.

3.3.1 XIA Digitizers

Digital Gamma Finders-4 Channel (DGF-4C) are the electronics used to primarily verify the output of the Spec32 system. The DGF-4C, shown in Figure 27, is an all-digital waveform acquisition spectrometer card with four input channels and an input and output clock of 40 MHz. It possesses a sampling rate of 5 Msamp/sec. The pre-amplified analog signals from the detectors are immediately digitized by the DGF-4C's 14-bit ADC's. The DGF-4C can accept a maximum rate of 200,000 counts per second from all four channels. Once the signal is digitized, the real-time processing unit (RTPU) utilizes a digital trapezoidal filter with independent, user-defined variable settings for the rise time and flat top and inspects for pulse pileup. Once the pulse has passed the pileup inspection, the RTPU issues a trigger. The digital signal processor (DSP) observes the triggers and processes the raw pulses. The DSP calculates pulse heights, time stamps each pulse and stores the data to the buffer for output to the controlling computer.

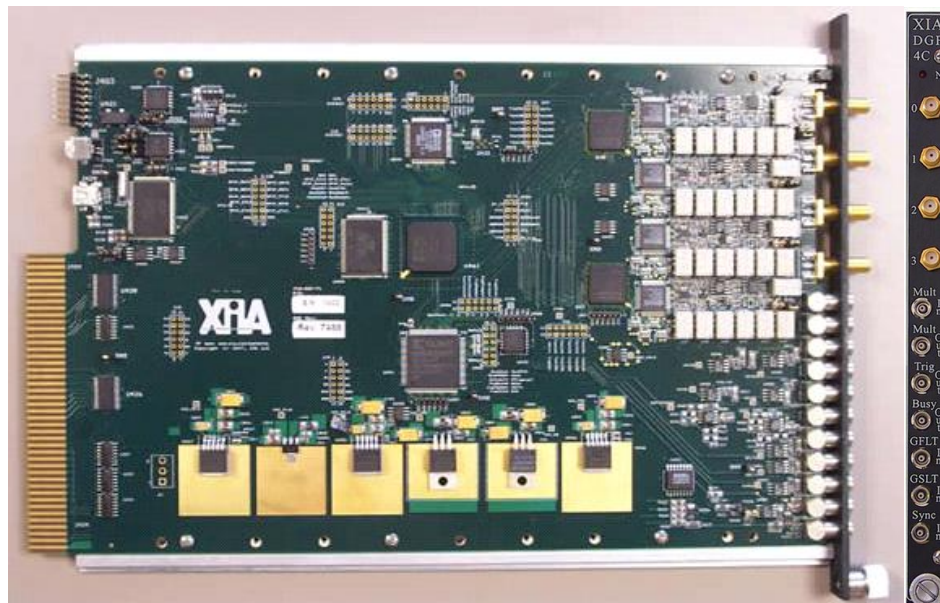


Figure 27. Picture of DGF-4C digital waveform acquisition/spectrometer card [78].

Output data is stored in two formats: MCA and list mode. MCA mode bins the data into 1,024 to 32,768 channels, depending on user settings. Using the software supplied by the manufacturer, DGF-4C Viewer, the data is displayed in a typical spectrum, frequency of counts as a function of channel number. The list mode, however, lists the energies, timestamps and waveform data for each event in a binary file for data processing. The data from the list mode from DGF-4C Viewer is loaded to an output buffer and then fed to a computer where the data for multiple channels and modules is used to reconstruct the events, post acquisition. The list mode will be predominantly used in this research. [78],[79]

3.3.2 Spec32

The Spec32 digital electronic system, shown in Figure 28, is a 32-channel, 50-MHz digitizer. The system contains four independent electronics boards, each with two 12-bit ADCs, 8 input channels and two Alterra Cyclone field-programmable gate arrays (FPGAs) [80]. Like the DGF-4C, the waveform from the detector's preamplifier is immediately digitized and the user defines the trapezoidal filter settings (flat top, and rise time) within the Spec32's software, Imager. The hardware for Spec32, however, operates differently than the DGF-4Cs. The DGF-4C digitizes the waveform and if the option is selected, saves the waveform in the list mode output file for further user-defined functions. The Spec32 system was designed specifically for imaging. As a result, the FPGA performs its programmed functions on the digitized waveform. For these experiments the FPGA's were programmed to determine the energy collected in the full-charge collecting strip and the figure-of-merits (FOM's) proportional to the area of the

transient charges in the strips directly adjacent. Then the FPGA clears the waveform data. This saves valuable memory in the buffer and decreases the number of buffer spills to the host computer.



Figure 28. Photograph of Spec32 digitizer system. The black wires are from the Ortec DSSD's preamplifier outputs and the gold are from the PHDS'.

Output data is stored in two data files: raw data and raw event logs. In the raw data file, energy data is stored for each of the 32-channels for a single trigger from a recordable event, either full-charge or transient charge, on any channel. The data is recorded in ADC units for each 20-ns clock tick. This type of file can be extremely large if there are a large number of triggers. In the raw event file, only events, in energy units based on the channel's calibration, are stored that pass the trigger threshold for only those channels that contain a signal above the trigger threshold. The FOMs for the transients charges in the strip to the left, denoted the predecessor, and the strip to the right, denoted the successor are also listed, as well as the time stamp. Since the Spec32 is only a 12-bit

system, the time stamp is reset every 256, 20-ns clock ticks. This means multiple events must trigger within a 5.12 μ sec window to positively know their time difference before the timestamp resets. No counter is available to list the time between timestamps.

There is an input limitation to the Spec32. Each FPGA will only accept pulses of the same polarity, as specified in the Imager software. Therefore, only groups of 4 inputs of the same polarity are allowed on each FPGA; specifically channels 0-3, 4-7, 8-11, 12-15, 16-19, 20-23, 24-27, and 28-31 on the Spec32 must have the same input pulse polarity.

3.4 Sources Used

Several radioactive sources were used for this research. The source of the positrons derived from the natural radioactive decay of ^{22}Na AFIT source T-132. T-132 is a ^{22}Na source with an activity of 106.5 mCi assayed on 15 August 2009 manufactured by Eckert & Ziegler, Isotope Products [81]. This radionuclide is encapsulated in a 25.4-mm diameter disk with a thickness of 3.18 mm, part of which is a 0.254-mm thick aluminized mylar cover. The active diameter of this ^{22}Na source is 3 mm. Two sources were used for the 514-keV photons, both ^{85}Sr sources. Both ^{85}Sr sources, T-128 and T-133 are manufactured identically by Eckert & Ziegler, Isotope Products as above, and their activities are 101.9 μ Ci and 96.79 μ Ci, assayed on 1 August 2008 and 15 August 2009, respectively. Sources in this document are identified by their AFIT source numbers.

3.5 Samples Used

Two types of samples were used: Cu and SiC. The Cu used in this experiment was purchased from MTI Corporation. Three samples of single-crystal Cu were procured with (100), (110), and (111) crystal orientations. The samples dimensions were 10.0 x 10.0 x 1.0 mm with one side highly polished. The AFIT model shop sliced the samples in half, in the 1-mm dimension which resulted in thicknesses of 0.40 ± 0.05 mm.

The SiC used in this experiment was W6NRDOX-0000 from CREE Incorporated [82], serial number AY1634-14. The sample is a research-grade, on-axis, N-type 6H-SiC wafer with orientation (0001). It is a 254.0 μm , 50.8-mm diameter disc with a single-side polished, with no epitaxial layer. The sample was doped with nitrogen with a net doping density of $1.3 \times 10^{18}/\text{cm}^3$. The wafer was cut into 12, 1-cm² squares by Larry Callahan from the Air Force Research Laboratory Sensors Directorate's Devices for Sensing Branch.

3.6 Vacuum Chamber and Pump

The positrons emitted from the ^{22}Na source can interact with air as they travel towards the sample material. Therefore, in order to minimize positron annihilation with air and maximize the number of positrons reaching the material sample, the source and sample were housed in a vacuum chamber. This chamber, fabricated by the AFIT model shop, was mated to a Varian type 949-9411 diaphragm vacuum pump designed to operate at 1 torr. This vacuum system, pictured in Figure 29, significantly reduced the amount of air in the chamber and minimized the positrons annihilating between the source and sample. The vacuum chamber was constructed of an aluminum shell. The front and rear

windows which face the DSSDs were constructed of 0.075 mm stainless steel, thin enough to minimize the attenuation of the annihilation photons travelling to the DSSDs but thick enough to maintain the vacuum. The sample was secured by a polyethylene holder, centered on the removeable source/sample tray, rotated 45° relative to the front window to minimize source attenuation of the annihilation photons and maximize the material sample's surface area facing the source, also shown in Figure 29. The source is identically secured but it is perpendicular to the front and rear windows. The heights, from the top of the tray to the centers of both the source and sample harnesses are equal.

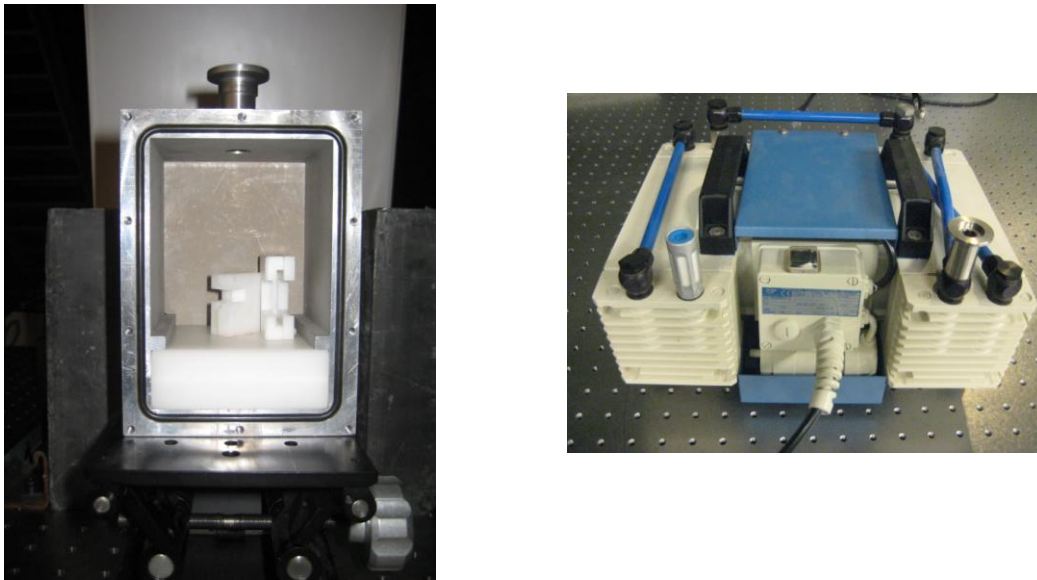


Figure 29. Left: Vacuum chamber with front window removed (removable source /sample tray in white). Right: Vacuum pump.

3.7 Source Shielding

One of the most important objectives in this experiment was to maximize the detection of the annihilation photons originating from the positrons' interactions within

the sample. At the same time, photons originating outside of the sample needed to be stopped from reaching the detectors in an effort to reduce dead time and extraneous data. The source/sample required adequate shielding from the detectors to reduce this potentially large scatter contribution. Therefore, the source/sample combination located in the vacuum chamber was externally shielded. A cage of lead bricks was machined by the AFIT Model shop to ensure flat, square surfaces and they were arranged around the vacuum chamber to provide extra shielding to reduce secondary and tertiary scattering. The lead cage was positioned to provide shielding coverage but not to interfere with the angle between the sample and the face of both detectors.

3.8 Collimator Fabrication

To determine the DSSDs' spatial resolution, a collimator with a small aperture was required. The collimator was constructed using AIM 70TM. This material, consisting of 50% bismuth, 27% lead, 13% tin, and 10% cadmium, has a density of 9.58 g/cm³, a photon attenuation 80% of that of lead, and a melting temperature of 70°C [83]. A 1-in² x 3-in long aluminum mold was fabricated with two, 0.25-mm diameter holes drilled in the center of each end. The collimator length was selected to attenuate 99% of the 514-keV photons. A nylon monofilament with a diameter of 0.18 mm was placed in the holes at both ends of the mold. Raw AIM 70TM material was melted by oven-heating to 80°C and poured into the pre-heated mold. The monofilament was put under tension as the material cooled, causing the monofilament to stretch somewhat. The estimate for the final collimator hole diameter is 0.15 ± 0.05 mm, determined from measuring the thickness of the monofilament after it was removed from the cooled collimator.

3.9 Translator

For the spatial resolution determination, the collimator and source required precise translation over an intrinsic pixel on the DSSDs. A Newport M-562 ULTRAlign Precision Multi-Axis Positioning Stage attached to a motorized Newport ILS-250 High Performance Linear Stage was used to translate the source/collimator combination. The M-562 provided linear translation in the vertical direction (denoted as y) to within $5\text{ }\mu\text{m}$ and the ILS-250 provided translation in the horizontal direction (denoted as x) to within $7\text{ }\mu\text{m}$ [84].

4 Procedure to Finalize Spectrometer Layout and Sample Preparation

Before the final spectrometer layout specifications could be determined, several items had to be quantified. This was accomplished by several experiments and analysis of the results. First, detector resolution was measured. Secondly, the relative method for determining location was evaluated. The feasibility of an absolute method was also examined. Following that, the spatial resolution of both DSSDs was determined. Next, a transient charge analysis was conducted with the intent of using them to improve the detectors' energy resolution. Then, the average relative efficiency for each DSSD was measured and the procedure to compensate the ACAR spectra for efficiency is detailed. After these items were completed, the final spectrometer layout is discussed. Once the layout was established, the procedure for collecting the simultaneous CDBAR and ACAR measurements is detailed. Finally, the procedure and methodology of the ion irradiation of the samples is discussed.

4.1 Resolution Characterization of Ortec and PHDS DSSDs

The energy resolution of both DSSDs, which is a function of the energy of events in the full-energy peak (FEP) and the noise in the electronics employed, is critically important to the CDBAR measurements. ^{22}Na cannot be used to accurately quantify the DSSDs' energy resolution due to the innate Doppler-broadening of the annihilation photons; therefore, 514-keV photons from ^{85}Sr source number T-133 were used. To estimate the energy resolution of each detector at 511-keV, a 72-hour data set was taken using both DSSDs, the Spec32 electronics, and the ^{85}Sr source. The centers of the detectors were axially aligned and the source was positioned 12.0 in from the face of each

detector. An in-house MATLAB code was used to process the raw event log from the Spec32. The code first discarded all full-energy events outside of the range 514 ± 30 keV. Then, coincidence between the front and rear strips in both detectors in both time and energy, was examined. Only coincident events were accepted. 514-keV FEPs were constructed for each strip and intrinsic pixel for both detectors. The resulting resolutions are located in Table 4. The average FWHM for the Ortec and PHDS DSSDs' intrinsic pixels was calculated as 1.76 ± 0.24 keV and 1.49 ± 0.17 keV, respectively.

Table 4. FWHM of each strip in Ortec (left table) and PHDS (right table) DSSDs.

Front Strip #	FWHM in keV	Rear Strip #	FWHM in keV	Front (DC) Strip #	FWHM in keV	Rear (AC) Strip #	FWHM in keV
F1	1.47	R1	1.51	20	1.23	4	1.62
F2	1.62	R2	1.66	21	1.31	5	1.54
F3	1.39	R3	1.49	22	1.55	6	1.78
F4	1.88	R4	1.99	23	1.42	7	1.29
F5	1.95	R5	2.01	24	1.44	8	1.37
				25	1.36	9	1.45
				26	1.68	10	1.51
				27	1.50	11	1.30

4.2 Relative Interpolation Method for Determining Full-Charge Event Location

Using Transient Charge Analysis

The relative method that derives the location of the annihilation photons' interaction with the detector crystal using the transient charges adjacent to the full-charge charge collection strip is called interpolation. The Spec32 raw event log lists the energy, in keV, of a triggered event in the full-charge collecting electrode and the transient charges in both adjacent strips. The transient signals are transformed into a FOM to

interpolate the full-charge event's location in its collecting electrode. This is done automatically in the FPGAs in the Spec32 and must be done post data acquisition for the DGF-4Cs. Although the method to calculate the FOM is proprietary, developed by PHDS Co., the FOM is proportional to the area of the transient signal as used by other researchers and is calculated only for the transient charges present in each of the two directly adjacent charge collection strips. The right adjacent strip is denoted as the successor and the left strip is the predecessor. Once calculated, a simple ratio of the left adjacent strip's FOM (FOM_{Pred}) to the sum of the left and right FOM yields the location relative to the left side of the strip. Equation (33), adapted for this application from Burks et al [51], is used to calculate the distance the event occurred relative to the left side of the Ge crystal.

$$\text{Distance} = \left(\text{Strip \#-1} + \left(\frac{FOM_{left}}{FOM_{left} + FOM_{right}} \right) \right) * \text{strip width} \quad (33)$$

Equation (33) yields the spatial location in the horizontal dimension which is combined with a similar determination using the upper and lower strips and their respective FOMs to obtain the location within a single DSSD. The distance from the left edge within a single charge collection strip is the second term in Equation (33). This interpolation method for subpixel location assumes that the ratio of the areas of the successor and the predecessor transient charges is proportional to the distance across the charge collection strip. More specifically, the area of the successor transient waveform increases relative to the area of the predecessor transient waveform as the distance increases from the left side of the charge collection strip [51]. In the next section, the

interpolation method was applied to determine the spatial resolution of the DSSDs and the validity of the method's assumptions were investigated.

4.3 Spatial Resolution Determination

In order to characterize the subpixel resolution of the DSSDs, photons were finely collimated onto subdivisions of the intrinsic pixel formed by the orthogonal intersection of F3 and R3 on the Ortec and the intersection of strips 24 and 8 on the PHDS DSSDs. These represent the center most strips on both DSSDs. These pixels were divided into a 5 x 5 array of subpixels, each denoted by pairs of numbers between one and five indicating their relative location, as shown in Figure 30.

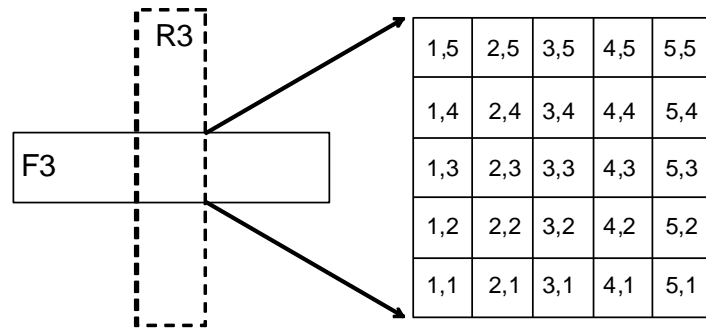


Figure 30. Subpixel irradiation pattern on Ortec's F3/R3 pixel by translation of source/collimator assembly.

⁸⁵Sr source number T-128 was centered over the collimator's aperture. The 514-keV photons were collimated onto the center of each subpixel using the collimator detailed in section 3.8, and the source/collimator combination was translated in 1-mm increments in the x and/or y direction to scan the entire subpixel array.

All of the Ortec DSSD's preamplifier outputs were fed into 4 XIA DGF-4C modules. The data set for determining Ortec DSSD's subpixel resolution was analyzed using an in-house developed code. This code reconstructed each event's waveform from the DGF-4C's list mode data file and calculated the FOM for the predecessor and successor transient charge of each charge collection event observed. The FOM was calculated using the same process as the Spec32's FPGAs, which is proportional to the area of the transient charges. The PHDS DSSD's preamplifier outputs corresponding to strips 4 – 11 and 20 - 27 were fed into the Spec32. The raw event file already contained the FOM for both transient charges for each event observed. Prior to inclusion in the spatial resolution characterization, each observed event was screened to ensure they met two criteria: (1) full-charge (514 keV) collection in both the front and rear strips, and (2) coincident predecessor and successor transient charge signals on neighboring front and rear strips corresponding to the full-energy event. This was required in order to interpolate events locations. The data set for each subpixel location was limited to the first 1,000 full-energy events which met the above criteria. Due to increased charge-sharing between strips and Compton scattering out of the pixel, longer counting times at subpixel locations near the edge and corners of the intrinsic pixel were required. Additionally, to estimate the background contribution from the 514-keV photons that leaked through the collimator, another data set was collected with the ^{85}Sr source placed directly over a 1-in² x 3-in long solid piece of AIM 70TM.

Transient signals were observed only in charge collection strips directly adjacent to strips detecting the full-charge event in both DSSDs. Examples of the signals resulting from irradiation of several locations within the Ortec DSSD's intrinsic pixel are shown in

Figure 31. The top row in the figure depicts the predecessor, full-charge and successor transient waveforms for a single event occurring near the left side of the pixel on the rear charge collection strip. The second and third rows show similar signals for events near the center and right side of the pixel, respectively. Relative differences in areas and pulse heights of the predecessor and successor transient waveform as a function of event location were observed. For the event near the left edge of the pixel, the predecessor transient charge is considerably larger than the successor transient charge; whereas near the right edge, the opposite occurs. For the center of the pixel, both transient charges are relatively equal in height and area.

Each data set, consisting of 1,000 full-energy events that met the criteria previously identified, were analyzed to locate each event within the pixel using the FOMs and Equation (33). Each subpixel was divided into 20 bins in each direction producing spatial intervals of 0.05 mm and the frequency for each bin was counted and displayed in a histogram. Figure 32 shows the histogram for all of the subpixel locations in the entire pixel for the Ortec DSSD, the results for the PHDS DSSD were similar.

It is evident from Figure 32 that the count distribution differs slightly from subpixel to subpixel, but all have the same general shape: a high-frequency peak corresponding to the location of the projected aperture of the collimator hole onto the surface of the germanium crystal with radially decreasing, symmetric tails. Viewing the data in a contour plot, Figure 33, supports the conclusion that both DSSDs' datasets are approximately radially symmetric with respect to the center of the experimental distribution.

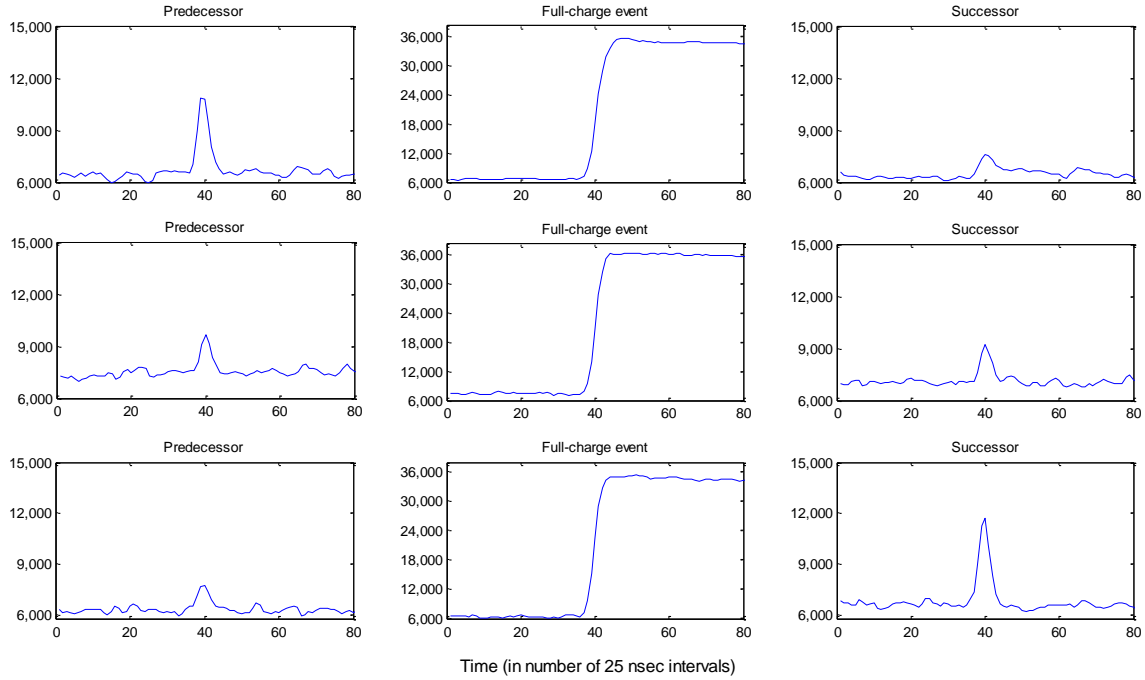


Figure 31. Top row: Full-charge and transient waveforms (in ADC units) for a single full-energy event near pixel's left edge on rear charge collection strip. Middle row: waveforms for event near pixel's center. Bottom row: waveforms for single event near right edge.

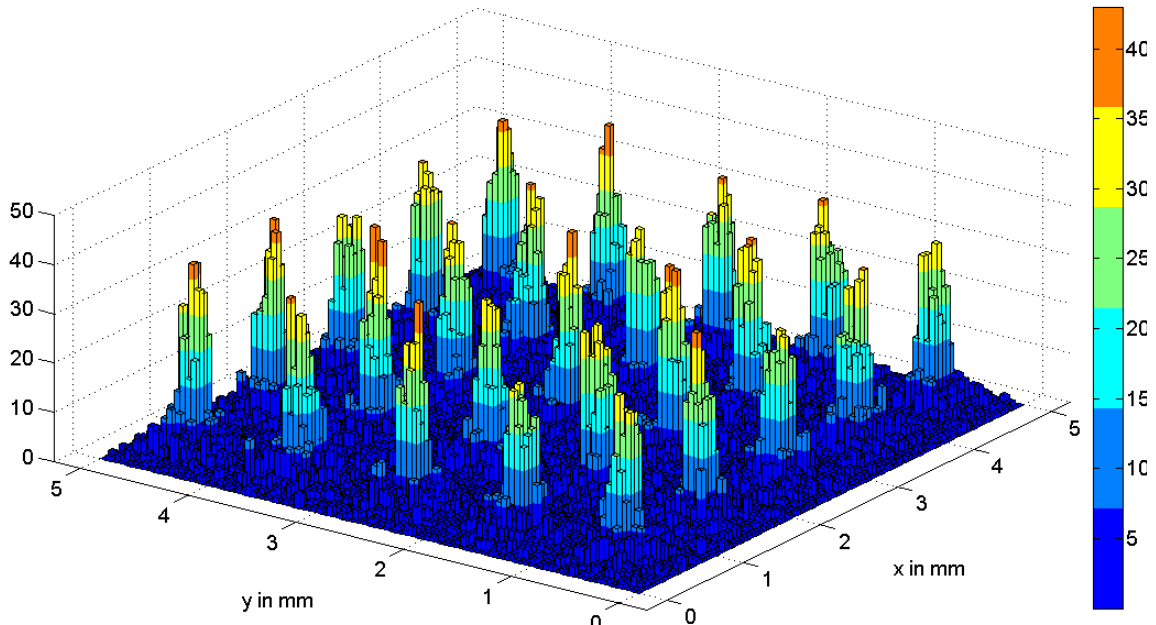


Figure 32. 2D histogram of count data for all 25 subpixel locations within the Ortec DSSD's F3/R3 intrinsic pixel. X and y coordinates were binned in 20 x 20 square 0.05-mm bins for each subpixel data set. Each subpixel contains 1,000 full-energy events, for a total of 25,000 counts.

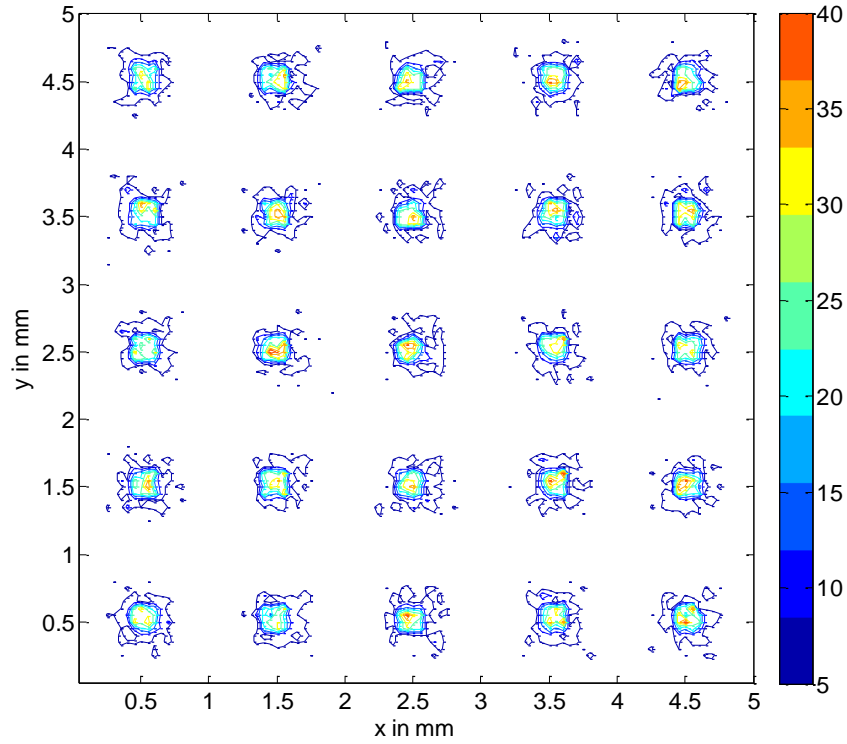


Figure 33. 2D contour plot of count data for all 25 subpixel locations within the Ortec DSSD's F3/R3 intrinsic pixel. X and y coordinates were binned in 20 x 20 square 0.05-mm bins for each subpixel data set. Each subpixel contains 1,000 full-energy events, for a total of 25,000 counts.

In order to fit this model to the count distribution derived from the processed data sets for both DSSDs, the location data for all 25 subpixels for each DSSD were combined and transformed from Cartesian coordinates to polar, assuming no angular dependence for location. The coordinates of each event were calculated relative to the measured center of the subpixel. The experimental count distributions for the 25 subpixels were summed and then counts were averaged for like radii to produce the average response of the detector as a function of distance from the subpixel center. As a result of the geometry, some radii had more numerous sampling points than others.

Next, the radii were transformed into α by dividing by the radius of the collimator's projection (r_a). Since the radius of the collimator's projection onto the surface of the crystal was estimated at 0.085 ± 0.025 mm (due to the distance between the collimator and crystal), 10 count distributions were created using collimator radii from 0.06 to 0.15 mm in increments of 0.01 mm to calculate α . The background contribution, estimated by measuring the 514-keV photons that leaked through the solid collimator, was subtracted from the experimental count distributions. The background-corrected, average number of counts for each radius was normalized to the area of data's distribution, as a result of the unevenly spaced radii. Equation (32), representing the model of a pixilated detector's spatial resolution, was plotted along with the background-corrected, normalized count distribution. The infinite series was expanded to a number of terms necessary to accurately estimate λ . The value of λ was varied to find the value that minimized the residuals in the least squares fits for all of the varying collimator radii data sets. The minimized least squares fits showed that the collimator projection's radius was actually larger than estimated, 0.10 ± 0.01 mm, and λ was 0.32 for the Ortec DSSD and 0.37 for the PHDS. Figure 34 displays the least squares fit of the data normalized to the area of the experimental count distribution as a function of α . Using the relationship for λ in Equation (25), the spatial resolution of the Ortec DSSD is ± 0.22 mm and ± 0.19 mm for the PHDS. This value is much less than the mean free path for a 170-keV photon in Ge (3 cm) suggesting that the error in location determination is associated with the measurement and processing of the transient waveforms, as well as, the method used to determine event location, as hypothesized. Additionally, as shown in Figure 32 and Figure 33, only a small residual background, attributed to the Compton scatter events that

degrade the spatial resolution are observed on the outer portions of the subpixel. Hence, the location uncertainty due to the physics of charge deposition is also a small factor when compared to the measurement and processing of the transient waveforms.

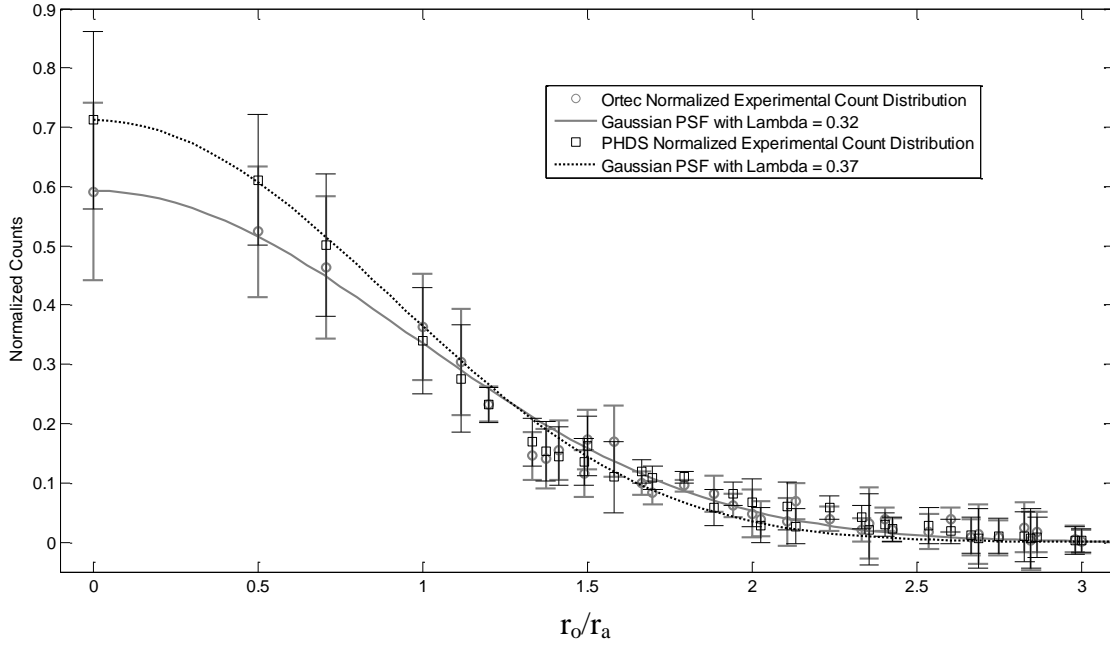


Figure 34. Gaussian point-spread function with circular aperture (solid line for Ortec DSSD and dashed line for PHDS) and normalized count distribution (corrected for background), averaged over all subpixels, as a function of α , which itself is a function of radius from the center of each subpixel location ($r = 0$) for collimator radius of 0.10 mm.

4.3.1 Validity of FOM Proportionality Assumption

In order to incorporate the transient charges in the interpolation method, the ratio of the predecessor and successor transient charges' areas must be proportional to the location across the charge collection strip. This was assumed the case when the interpolation method was applied in Section 4.3 and will now be examined. For this

assumption to be valid, the experimental count distribution for each subpixel should be centered on each subpixel's known center location, which is accurately known from the precise collimator translation. To test this assumption, the center of each subpixel's count distribution was determined using a contour plot of the data, shown in Figure 33. The observed x- and y-coordinates of the center of the experimental distribution for each subpixel resulting from application of the interpolation method were averaged for like coordinates and compared with the known location of the center of each subpixel derived from the precise translation. The results are shown in Table 5.

Table 5. Comparison of actual and observed subpixel location. The x- and y-coordinates of the actual subpixel location are known to within 7 μm and 5 μm , respectively.

Coordinate	Actual Subpixel Location (mm)	Observed Subpixel Location (mm)	Observed Subpixel Location Standard Deviation (mm)
x	0.500	0.514	0.015
	1.500	1.502	0.019
	2.500	2.474	0.023
	3.500	3.532	0.015
	4.500	4.496	0.019
y	0.500	0.532	0.019
	1.500	1.524	0.015
	2.500	2.534	0.022
	3.500	3.542	0.036
	4.500	4.510	0.021

The observed subpixel locations were only slightly different from the actual location; on the order of several hundredths of a millimeter. The standard deviations in the observed subpixel locations were on the order of several hundredths of a millimeter.

This demonstrates that the subpixels' count distributions were centered very closely to the center of the subpixel. Based on this analysis, the assumption of the interpolation method that the ratio of the predecessor and successor transient charges' areas are proportional to the location across the charge collection strip is valid.

4.3.2 Efficiency of the Interpolation Method

The number of useable events was reduced due to discarding bipolar signals and events which did not meet the interpolation criteria described in Section 4.2. As a result, the efficiency as a function of distance from the center of each subpixel was examined for both DSSDs. This relative subpixel efficiency for each DSSD was estimated from a second series of data sets using a constant measurement time of two hours per subpixel with the same collimator and source arrangement from the subpixel resolution measurement as discussed in Section 4.3. Since each data set's collection time was fixed to two hours, the relative efficiency of each subpixel location was determined by tallying the number of events that met the criteria at each subpixel location and then normalized using the value of the center subpixel (3,3).

In order to transform the data set for this analysis, the Cartesian coordinates for the center of each subpixel, relative to the center of the intrinsic pixel, were converted to radii. Count tallies with the same radial distance from the center of subpixel (3,3) were averaged and plotted. Figure 35 displays the relative average efficiency normalized to the center subpixel (3,3) as a function of distance from the center of the intrinsic pixel for both DSSDs.

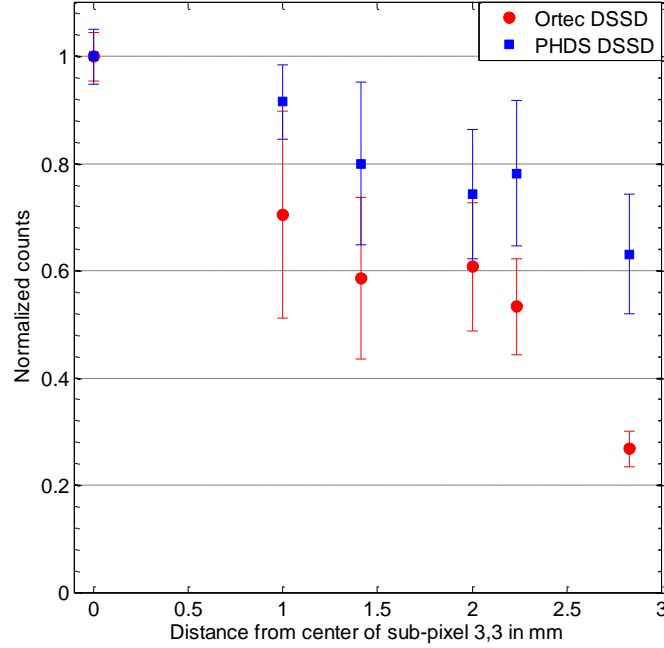


Figure 35. Relative average efficiency normalized to the number of counts in the center subpixel (3,3), a total of 943 counts for the Ortec and 1292 counts for the PHDS, as a function of distance from the center of the intrinsic pixel for both DSSDs.

As hypothesized, the relative average efficiency is highest in the center of the intrinsic pixel and decreases toward the edges with the minimum concentrated at the corner subpixels. The corner subpixels, which are farthest from the center, have the least relative efficiency. This is most likely due to their position on the edges of both the front and rear charge collection strips, the increased probability of not observing a transient charge in the electrode furthest from the event, and the increased probability of the Compton scattered photon scattering out of the pixel. Violation of any of these criteria resulted in rejection of that event for interpolation, sacrificing the detection efficiency for improved spatial resolution. Additionally, the PHDS DSSD has a higher relative efficiency across the strip. This is most likely due to two factors: crystal thickness and

detector age. Recall the PHDS' crystal is 2 mm thicker, and therefore more efficiently interacts with the 514-keV photons. Also, the PHDS detector is only 1 year old whereas the Ortec is approximately 10. Therefore, the ohmic contacts are fresher on the PHDS DSSD and most likely have not degraded as much as the 10-year old Ortec.

4.4 Absolute Interpolation Method

Since the relative interpolation method of using the FOMs from the predecessor and successor strips worked well for determining the location of the event, an absolute method was investigated by examining the following question: Could the FOM from either the successor-only or the predecessor-only charge collection strip be used to ascertain the event's location? If this method were to prove promising, all strips on the detector could be used for location analysis, to include the edge strips, enabling a larger angular range to be measured at the same angular resolution. Recall Cooper et al used only a single transient charge to determine event location within the charge collecting electrode. Unfortunately, the Spec32's sampling rate was not fast enough to adequately detail the leading edge of the waveform to use their method, so another potential absolute method was investigated.

To determine the feasibility of using the FOMs as an absolute method, only the events calculated to have occurred within 0.025 mm of the center of each subpixel from the data set collected in Section 4.2 for the Ortec DSSD were examined. The successor and predecessor FOMs were determined for each event. The successor-only and predecessor-only FOM values were averaged and the standard deviation determined for each subpixel, shown in Figure 36 and Figure 37.

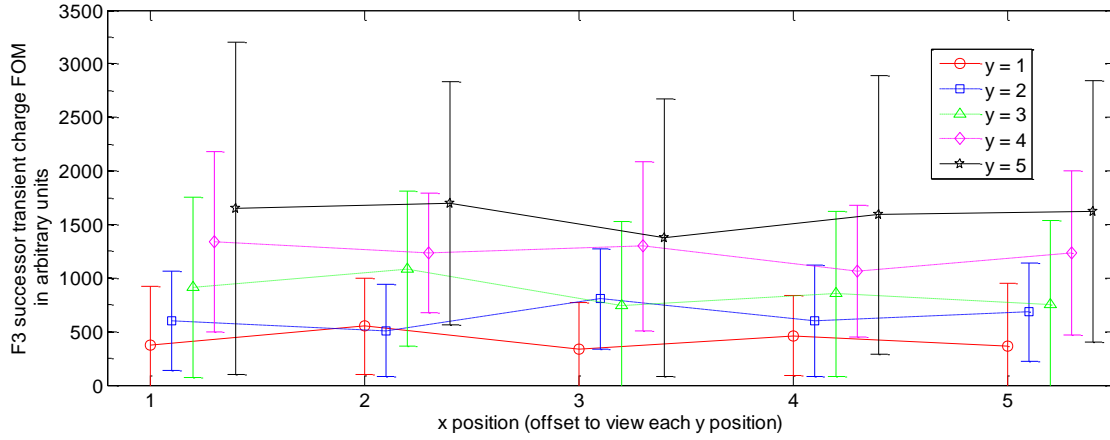


Figure 36. Successor-only FOM values at each subpixel location across F3/R3 intersection.

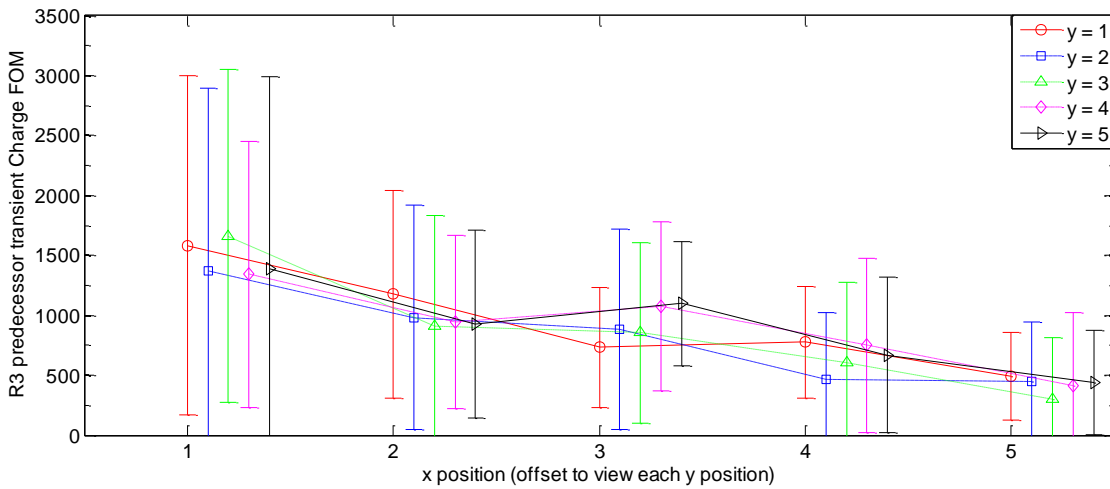


Figure 37. Predecessor-only FOM values at each subpixel location across F3/R3 pixel.

The FOM averages for subpixel centers, using either predecessor or successor-only transient charges, were relatively uniform across the subpixels in the strip in either direction, but there was a large range in the FOM values at each location, indicated by the error bars. To quantify the significance of the error, the relative standard deviation for both predecessor-only and successor-only transient charge FOM average values were

determined at each subpixel location center. The average relative standard deviation of the FOM averages was 0.90 ± 0.23 for successor-only events and 0.93 ± 0.26 for the predecessor-only events. Since the variability was large compared to the FOM average as shown in Figure 36 and Figure 37 and the large relative standard deviation, the single transient charge data was not useful to permit subpixel imaging. Therefore, an absolute method using only one FOM was not feasible.

4.5 Compensation for Subpixel Efficiency

The efficiency of a subpixel, as shown in Section 4.3.2, is a function of its location relative to the center of a charge collection strip. This correlation will bias the 2D ACAR measurements and must be compensated for in the final ACAR data. In order to compensate for a subpixel's relative efficiency, the efficiency of each subpixel across each detector must be determined. To quantify the efficiency, a data set was acquired for the PHDS and Ortec DSSDs.

The detectors were placed 2.0 m apart with ^{85}Sr source number T-133 centered between them. A 96-hr data set was taken using the Spec32 electronics. The data set was analyzed by examining only $514 \pm 15\text{-keV}$ events coincident in both time and energy with the front and rear strips for each detector, independently of each other. Since 514-keV photons were examined and not the near collinearly-emitted annihilation photons, coincidence between detectors was not considered. The location of each coincident event was determined using the interpolation method (Equation (33)) for each detector. Each intrinsic pixel recorded $\sim 120,000$ and $\sim 100,000$ counts and each subpixel

recorded between 4,000 - 62,000 and 2,600 - 5,600 for the PHDS and Ortec DSSDs, respectively. Figure 38 displays the count distribution for each subpixel in each DSSD.

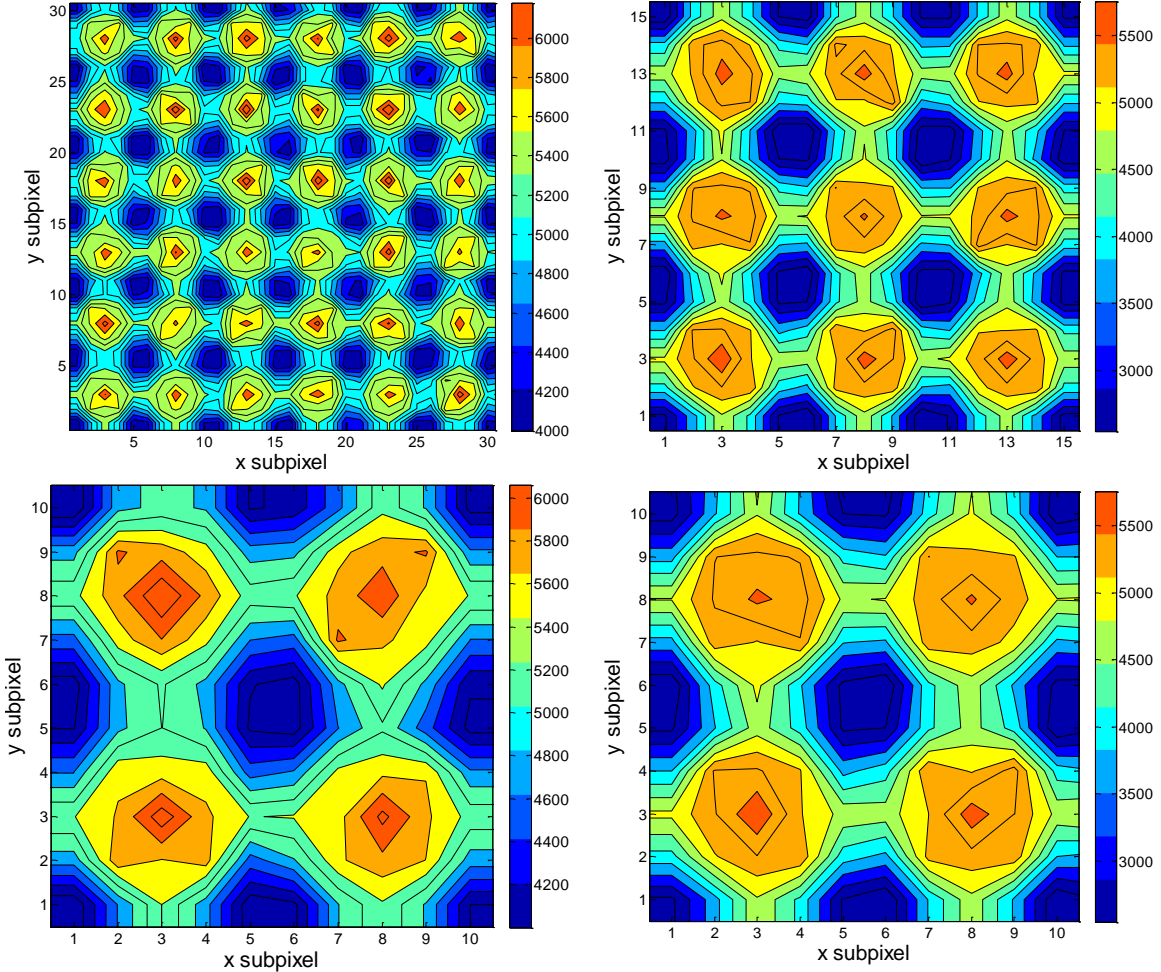


Figure 38. Top left: 2D count distribution in PHDS DSSD over entire active charge collection strips. Top right: 2D count distribution in Ortec DSSD over active charge collection strips. Bottom left: 2 x 2 intrinsic pixel array from bottom left of PHDS count distribution. Bottom right: 2 x 2 intrinsic pixel array from bottom left of Ortec DSSD count distribution. (1:5 subpixels in both x and y indicates one intrinsic pixel).

If the efficiency for detecting full-energy events was constant across an intrinsic pixel, the count distribution should be relatively flat, which was not the case. It was clearly evident the efficiency varied systematically as a function of distance from the

charge collection strips' edges. This result compared well with the data presented in Figure 35, where efficiency was the greatest in the center of an intrinsic pixel and decreased radially outward with corner subpixel's possessing the poorest efficiency.

Compensation for the efficiency of the detectors and the interpolation method varies with the location of the subpixels which detect each annihilation photon in each DSSD. The average relative efficiency for each subpixel was determined by normalizing each subpixel's count tally to the center of each intrinsic pixel and then averaging for like subpixels, using the data presented in Figure 38. This data is shown in Table 6.

Table 6. Average relative efficiency of each subpixel type in each DSSD.

Subpixel Location	Ortec DSSD Average Relative Efficiency	PHDS DSSD Average Relative Efficiency
Outside Corner	0.39 ± 0.04	0.59 ± 0.03
Outside Edge	0.54 ± 0.03	0.71 ± 0.03
Inside Corner	0.71 ± 0.03	0.80 ± 0.03
Inside Edge	0.86 ± 0.03	0.91 ± 0.02
Center	1.00 ± 0.02	1.00 ± 0.02

In order to compensate for the efficiency, the cumulative count distribution in each bin in the final ACAR spectra was scaled using each recordable event using the following expression:

$$\frac{1}{Eff_{PHDS} \times Eff_{Ortec}} \quad (34)$$

where Eff_{PHDS} is the relative efficiency of the subpixel recording one annihilation photon in the PHDS DSSD and Eff_{Ortec} is for the Ortec DSSD. Therefore, if both DSSDs detected both annihilation photons in the subpixel in the center of intrinsic pixels, then no adjustment was made; one count was added to the respective ACAR spectral bin. If

either or both DSSDs detected the photons in any subpixel other than the center, the count distribution in the ACAR spectrum's bin correlating to the relative location of the two subpixels was increased by more than 1 count.

The average relative efficiency for each DSSD was mapped into every active intrinsic pixel. The average relative efficiency of each subpixel used to compensate for the varying efficiency over the subpixel using Equation (34), is shown below in Figure 39.



Figure 39. Subpixel average relative efficiency for Ortec (left) and PHDS DSSD (right).

Since the efficiency of each subpixel in both DSSDs was not directly mapped, instead the average over all intrinsic pixels, some uncertainty was introduced. To quantify this uncertainty, the expected increase in each ACAR bin resulting from compensating for the varying efficiency across the width of the charge collection strips in the DSSDs was determined. The expected increase in the number of counts was simply calculated by multiplying the expected average relative efficiency for each DSSD flowing the expression in Equation (34). Using the data presented in Table 6 and propagating the error, the expected average efficiency for each DSSD was 0.62 ± 0.03 and 0.74 ± 0.02 for the Ortec and PHDS DSSDs, respectively. Therefore, the increase in

each ACAR bin using Equation (34) to compensate for the varying efficiency across the width of the charge collection strips in the DSSDs was increased by a factor of 2.18 ± 0.09 . The error contribution in the expected increase averaged out across the ACAR spectrum assuming a statistically significant number of counts are recorded in each ACAR bin before the compensation. Regardless, any error induced from mapping the average subpixel efficiency onto all pixels relative to mapping every subpixel's efficiency in both DSSDs was extremely small compared to not compensating for the efficiency.

4.6 Potential Correlation Between Event Energy and Associated FOMs

Correlation between an event's FEP energy and its associated FOMs for events which passed the interpolation criteria was investigated. The intent was to use the FOMs to improve the energy resolution for the CDBAR application. To quantify any potential correlation, the energy of each recorded coincident event from the data set collected in Section 4.5 was plotted against their associated FOMs, both successor and predecessor, in varying relationships, and fitted to linear, quadratic, and cubic functions. The data and subsequent fit to the functions are shown in Figure 40. The resulting best fits, which were linear with slopes on the order of 0.04, indicated poor correlation between event energy and FOM values. Therefore, FOMs were not useable to improve the energy resolution for the DBAR application.

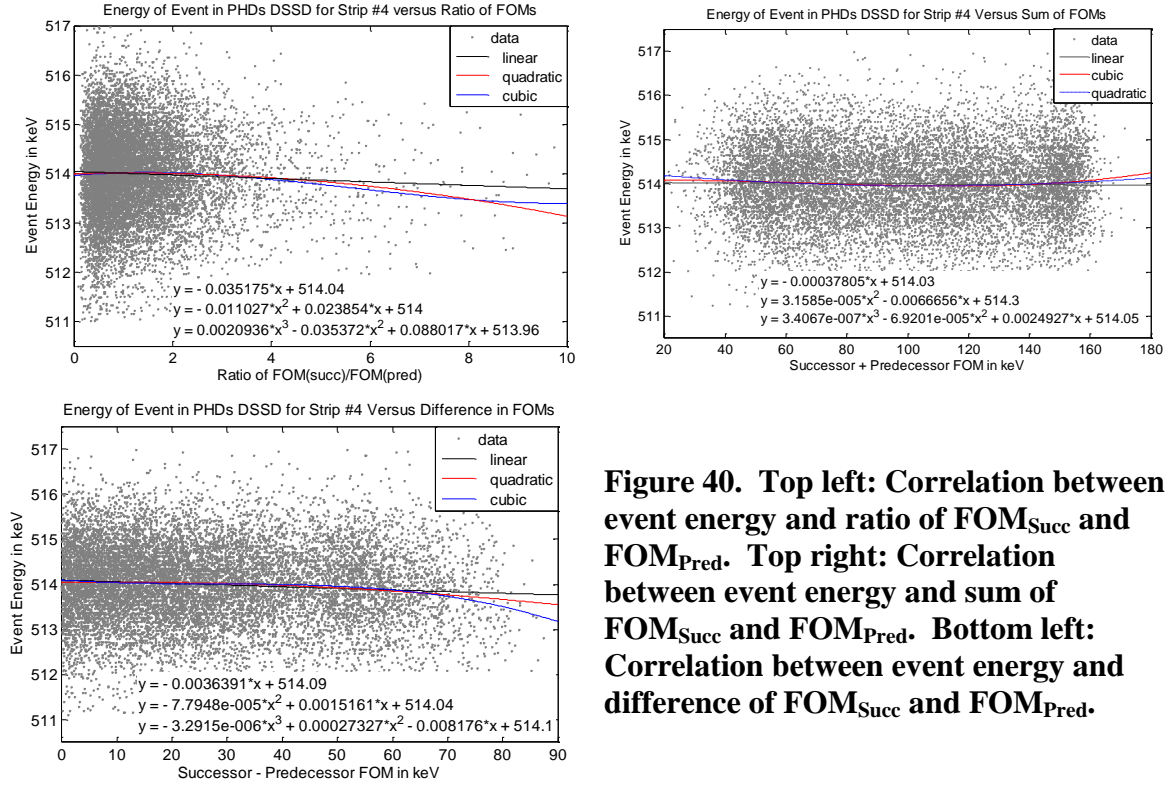


Figure 40. Top left: Correlation between event energy and ratio of FOM_{Succ} and FOM_{Pred}. Top right: Correlation between event energy and sum of FOM_{Succ} and FOM_{Pred}. Bottom left: Correlation between event energy and difference of FOM_{Succ} and FOM_{Pred}.

4.7 Spectrometer Layout

Based on the measured subpixel spatial resolution analysis of both DSSDs outlined in 4.3, the dimensions of subpixels for ACAR analysis were established as 1-mm² squares, corresponding to two standard deviations of resolution error associated with the interpolation method. Having defined the subpixel dimensions, the layout of the spectrometer was finalized. The distance between the DSSDs to the center of the interrogated sample was calculated using simple geometry. Desiring an angular resolution of 0.5 mrad and using the width of a pixel (1 mm established from the transient charge analysis), the distance between the DSSDs from the sample (denoted as Z_{DSSD}) was the following:

$$Z_{DSSD} = \frac{1 \text{ mm}}{\tan^{-1} 0.0005 \text{ rad}} = 2.000 \text{ mm} . \quad (35)$$

Since the spatial resolution of both the Ortec and DSSD were very similar, the distance between the both DSSDs and the sample were identical which ensured spectral symmetry. The final physical layout of the spectrometer is displayed in Figure 41.

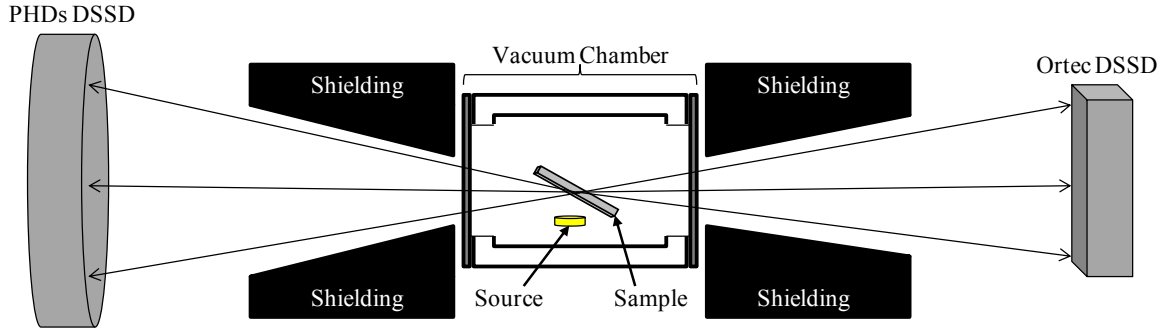


Figure 41. Top view of final spectrometer configuration with PHDs and Ortec DSSDs, each 2.00 ± 0.01 m from the center of sample, located in vacuum chamber (not to scale).

The DSSDs were coupled together with the Spec32 digital electronics system. The Spec32's FPGAs were programmed to provide trigger time, event energy and the predecessor and successor FOMs. The FOMs were used to properly interpolate the location of annihilation photons' interactions within intrinsic pixels of the DSSDs. This allowed measurement of the ACAR response without having to record the entire waveform, like the DCF-4C cards required, which greatly reduced the size of the data file. The sampling rate of the Spec32, however, limited the simultaneous measurement technique. Since the leading edge of the waveform was not reconstructed to determine the relative difference in the collection times of the electrons and holes, as discussed in Section 2.7, the depth of the annihilation photon's interaction in the DSSD could not be

determined. Additionally, interpolation requires transient charges on both sides adjacent to the full-charge collection strip. Edge strips, were not used in interpolating the location of a full-charge event, since one FOM was missing. Therefore, the edge strips were used only for observing and recording transient charges. Furthermore, the Spec32 only accepts 32 inputs, which limited the number of inputs from the PHDS DSSD. For that reason, all 10 of the Ortec (F1-F5 and R1-R5) and only 16 of the center-most strips of the PHDS (4-11 on the AC side and 20-27 on the DC side) DSSD's outputs were used.

4.8 Code Development

The primary goal for this experiment was to design and develop a single spectrometer composed of two HPGe DSSDs used in coincidence with an appropriate digital electronics suite to extract CDBAR and 2D ACAR spectra from a single measurement. In order to extract DBAR and ACAR spectra from a single data set, a post-acquisition code was developed that accomplished several functions. The code was written in the MatlabTM environment and due to its length, is included in the digital copy of this document.

The code read in the raw event file from the Spec32 into a large matrix. All recorded events outside of the energy range 511 ± 30 keV were discarded so as to identify and subsequently process only un-scattered annihilation photon interaction events, since only full-energy events were considered by the interpolation method. This reduced the data file size by over 99% and greatly increased data processing efficiency.

The code examined all events within a single clock cycle of 5.12 μ sec, composed of 256 - 20 nsec clock ticks. Clock cycles not containing a full charge event on a charge

collection strip on each side of each detector occurring within a 60 ns coincidence timing window were discarded. This resulted in a matrix containing sequential clock cycles with each cycle containing four, coincident full-energy events in charge collection strips on each side of each DSSD. Each row of the matrix listed each full-charge event's energy, timestamp, channel number (corresponding to the charge collection strip recording the annihilation photon's interaction with the DSSD) and successor and predecessor FOMs for the event.

The location of annihilation photon's interaction within each DSSD was determined using the event's FOMs in Equation (33). The location was determined within the center three charge collection strips (on both the front and rear faces) for the Ortec and center six (on both the front and rear faces) on the PHDS DSSD. The location was determined relative to the center of each DSSD. This was accomplished both vertically and horizontally in each detector, resulting in X and Y coordinates for each event in each DSSD. (Locations to the right of DSSDs' centers were positive values for the X direction and negative to the left and locations above the DSSDs' centers were positive values for the Y direction and negative below). Once the location of the annihilation photon's interaction with a subpixel was determined, the relative efficiency for that subpixel was selected based on the analysis presented in 4.5. This was accomplished for all events in the matrix. Then, a single row in a new matrix was written listing the following data for both coincident annihilation photons produced in the annihilation event: the energy of the photon detected in the Ortec DSSD, the energy of the photon detected in the PHDS DSSD, the X and Y coordinates for the photon interaction in the Ortec DSSD, the X and Y coordinates for the photon interaction in the

PHDS DSSD, the average relative efficiency of the subpixel recording the event in the Ortec DSSD and the average relative efficiency of the subpixel recording the event in the PHDS DSSD. This matrix was then used to reconstruct the 2D ACAR and CDBAR spectra. Since MatlabTM could only process raw event files smaller than 2 GB, the code read in a single raw event file and wrote to the final matrix, read the next raw event file, wrote to the final matrix, etcetera until all raw event files from a complete measurement were processed. The complete, final matrix was used to reconstruct the 2D ACAR and CDBAR spectra.

4.9 Simultaneous 2D ACAR and CDBAR Experiment

In order to demonstrate the advantages of simultaneous 2D ACAR and CDBAR, one simultaneous momentum data set was measured for one virgin Cu and one virgin and two ion irradiated 6H SiC samples. Each data set was collected until 10^6 coincident events that passed the energy and time criteria for the interpolation method were accumulated. The live-time varied from 12-14 days to collect momentum data sets for the virgin samples and 24 days for the irradiated samples. 2D ACAR and CDBAR spectra were populated from each sample's data set using the complete, final matrix of qualified coincident events.

The 2D ACAR spectra were binned according to the angular resolution, in 0.5×0.5 mrad bins, and the CDBAR spectra were binned into 0.1-keV intervals. The CDBAR bin-size was selected using 2.5 times the largest slope measured from the analysis correlating event energy and FOM values performed in Section 4.6. This resulted in a $0.5 \times 10^{-3} m_0c$ and $0.4 \times 10^{-3} m_0c$ momenta resolution in the 2D ACAR and

CDBAR spectra, respectively. Two 2D ACAR spectra were reconstructed from each measurement: one with the ACAR data corrected to compensate for the varying subpixel efficiency and one with no efficiency correction. CDBAR spectra were reconstructed by plotting the energy of each of the coincident annihilation photon's energy collected by each DSSD. The DB lineshape was extracted and analyzed. The DB lineshape represented the constraint governed by the following equation:

$$E_{Ortec} + E_{PHDS} = 1022 \text{ keV} \pm \Delta \quad (36)$$

where E_{Ortec} and E_{PHDS} is the energy collected by the corresponding detector for each of the coincident pairs of annihilation photons detected and Δ is the width of the lineshape extracted from the CDBAR spectra. Recall from Baranowski et al, they used a Δ of 4 keV, correlating to the binding energy of an electron in the material interrogated. There was no previous analysis documented in the literature, however, that examined the influence of Δ on the features of the DB lineshape. It was hypothesized that as Δ is varied, the fluctuations at the base of the DB lineshape reached a minimum without degrading any observed features in the spectrum. To prove this hypothesis and minimize fluctuations at the base of the DB lineshape, Δ was varied from 0 keV to 5 keV in increments of 0.1 keV. The final Δ used was the width that minimized the DB lineshapes' width at $1/100^{\text{th}}$ the maximum number of counts in the peak. This analysis minimized the uncertainty in the counting statistics of the DB lineshape's intensity without degrading the energy resolution of the lineshape.

Virgin, single-crystal Cu was the first sample analyzed to evaluate and compare the spectrometer's ACAR and CDBAR performance to published results. Cu was chosen

for calibration for two reasons: Cu has been extensively studied and its 2D ACAR distribution perpendicular to the (100) orientation is approximately symmetric. Then virgin, single-crystal 6H SiC was analyzed and compared to published results. Finally, samples of the 6H SiC were bombarded with varying fluences of O^+ ions and analyzed.

4.10 Ion Irradiation

Ions create varying kinds of defects in their track as they slow down and interact. The purpose of this research effort is to examine the effect of the implanted O^+ ion on e^-e^+ annihilation in SiC. To examine the effect of the ions rather than the damage they created, ions were directed into one side of a sample, and the positrons entered from the other side. This allowed the positrons to sample the O^+ ion distribution's perturbation of the lattice structure, rather than the plethora of defects produced during the ions' interactions.

In order to determine the range of the positron in SiC, a simulation was executed in GEANT4 [85], [86] by 2Lt Robert Slaughter as part of his Master's Thesis work. GEANT4 is a software program written in C++ which utilizes a Monte Carlo simulation to model the transport and interaction of particles in matter. Based on that simulation, positrons annihilate at a median depth of approximately 105 μm in 6H SiC. Therefore, the O^+ ions must have a range of 149 μm in order to for the positrons to interact directly with the O^+ ions through the 254- μm thick sample.

The samples were bombarded at the Ion Beam Laboratory (IBL) at Sandi National Laboratory (SNL). The beam was operated at maximum power and produced 24 MeV

O^{3+} ions at 20 particle-nanoamps. This resulted in 1.25×10^{11} O^+ ions/sec implanted normal to the surface.

The O^+ ion beam spot-size measured $0.5 \text{ cm} \times 0.5 \text{ cm}$. Four, 1 cm^2 6H SiC samples were irradiated with different irradiation times, 1.0, 10.0, 100.0 and 1000.0 sec, resulting in the following fluences: 3.12×10^{11} , 3.36×10^{12} , 3.13×10^{13} , and 3.12×10^{14} ions/ cm^2 . The damage induced into the 6H SiC samples was clearly visible on the higher three fluence irradiated samples as a dark brown region, which decreased as the O^+ ion fluence decreased. These fluences were similar to what Uedono et al [69] used when they studied near-surface vacancy-type defects in 6H SiC samples as discussed in 2.11. They implanted 1×10^{13} and 10^{15} 150-keV O^+ ions and observed significant changes to the S parameter from their DBAR analysis.

To determine the depth at which the O^+ ions were implanted, the Stopping and Range of Ions in Matter (SRIM) 2008 [87] software program was used to calculate the stopping and range of ions for this research using the energy of the O^+ ions as the parameter to control the range of the ions. Using the Transport of Ions in Matter (TRIM) set up window, simulations were conducted to calculate the energy required to achieve the necessary range. The ion selected was O with an energy of 24,000 keV. No. 590 Silicon Carbide, with a width of $254 \text{ }\mu\text{m}$, was selected from the compound dictionary for the target data for the SiC. The number of simulated ions was set at 10,000 to provide a statistically meaningful result. The 24-MeV O^+ ions were deposited at a depth of $10.8 \pm 0.5 \text{ }\mu\text{m}$, just a small fraction of the depth through the SiC sample. According to TRIM, each ion produced 1,796 vacancy-type defects in the SiC lattice in the ions' tracks. Additionally, the lateral spreading of the ions was minimal, on the order of $3 \text{ }\mu\text{m}$

from the beams focus on the sample. The output from SRIM for the simulation is displayed in Figure 42.

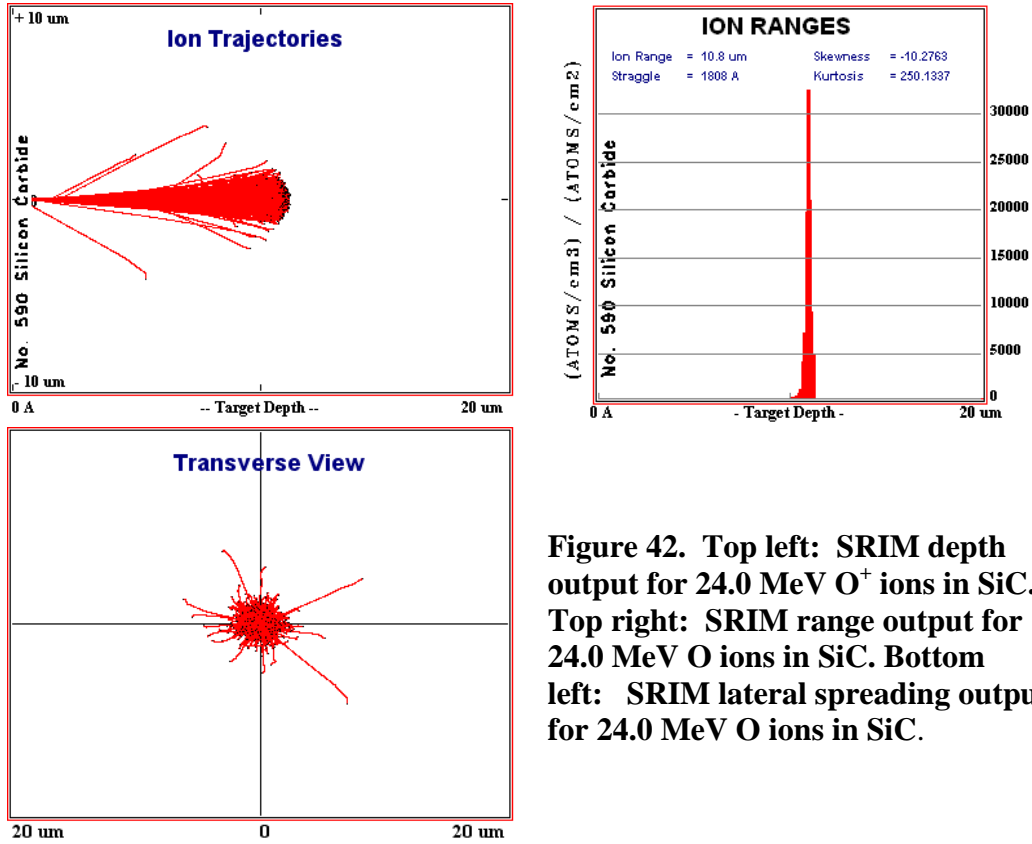


Figure 42. Top left: SRIM depth output for 24.0 MeV O^+ ions in SiC. Top right: SRIM range output for 24.0 MeV O ions in SiC. Bottom left: SRIM lateral spreading output for 24.0 MeV O ions in SiC.

Since the O^+ ions implanted by the SNL IBL were only deposited 10.8 μm into the 6H SiC, the samples were dry etched by the Air Force Research Laboratory, Sensors Directorate to remove $140 \pm 5 \mu\text{m}$ of the 6H SiC from the sample side opposite to the one the ions were implanted. Therefore, the layer of O^+ ions was $\sim 100 \mu\text{m}$ from the etched surface. This allowed for simultaneous 2D ACAR and CDBAR measurements with the O^+ ions at the median depth the positron will penetrate.

4.11 Sample Annealing and Diffusion of O Atoms

The 6H SiC was irradiated with O^+ ions using the process outlined in Section 4.10. To examine the affects of the O^+ ion irradiation and the vacancy-type defects produced by the thermalization of the O atom, an ion-irradiated, un-annealed sample was measured using the simultaneous 2D ACAR and CDBAR technique. Additionally, the effect of only the O atoms on the crystal lattice of the SiC was also desired. To accomplish this, the sample required annealing to greatly reduce the concentration of vacancy-type defects produced as a result of the ion irradiation.

The 6H SiC sample implanted with 3.12×10^{14} ions/cm² of O^+ ions was measured twice using the simultaneous 2D ACAR and CDBAR technique, once without annealing and once following a high-temperature anneal. The sample was annealed at 1000°C for 30 min in a dry argon (Ar) environment, similarly to the technique of Kawasuso et al [67]. The 6H SiC sample was placed on a quartz rod which was enclosed in a 1-in outer-diameter quartz tube, housed inside of the BLUE MTM furnace, model number TF55030A and serial number R04E-202768-RE. The rod was pushed through the tube into the furnace and positioned over the heating element once the temperature inside of the quartz tube reached 1000°C. The quartz tube was filled with dry Ar gas at a flow rate of 20 L/min. After the 30 min anneal, the rod was pulled out of the furnace and cooled inside the quartz tube for 30 min. Based on the results obtained by Uedono et al [69], annealing at 1000°C for 30 min in dry argon gas annealed out V_C , V_{Si} , and $V_{Si}V_C$ divacancies, leaving only some open spaces adjacent to these defects, which finally annealed out at 1400°C.

The focus of the annealing was to reduce the concentration of vacancy-type defects without significantly diffusing the O atom layer. To determine the annealing affects on the O atom layer, the diffusion of the O atoms was calculated for a temperature of 1000°C at 30 min. To calculate the diffusion of O atoms in the SiC, the thin-film equation for diffusion, based on Fick's law presented by Kingery et al [88] was used and is as follows.

$$C = \frac{\alpha}{2\sqrt{\pi Dt}} \exp\left(-\frac{x^2}{4Dt}\right) \quad (37)$$

where C is the concentration of O atoms at a distance x from the original location prior to diffusion, x is the distance from the initial concentration of O atoms, D is the diffusion coefficient, α is the initial O atom concentration prior to diffusion and t is time. Using the parameters discussed above for α and t and using D of 10^{-22} cm²/sec for 6H SiC annealed at 1000°C, as determined by Tairov et al [89], annealing the sample reduced the concentration of O atoms to 50% at a diffusion length of 0.2 nm. This length is approximately the same dimension as the bond length in the SiC, and to 10% at a length of 0.4 nm. Therefore, annealing the 6H SiC sample did not diffuse the O atoms enough to expand the implanted O atom layer to affect the measurements.

5 Results and Discussion

5.1 Overview

Simultaneous 2D ACAR and CDBAR measurements, termed three-dimensional positron annihilation momentum measurement (3DPAMM), were collected for virgin Cu and 6H SiC and O⁺ ion irradiated 6H SiC samples. Performance of the three-dimensional positron annihilation spectroscopy system (3DPASS) was compared with published ACAR and DBAR experimental measurements and calculations for single-crystal Cu. The momentum data set for 6H SiC sample with 3.12×10^{14} ions/cm² was collected twice using the 3DPAMM technique, once without annealing and once with a high-temperature anneal. Then, the 2D ACAR, the DB lineshape and 3D momentum lineshapes were constructed and analyzed for the 6H SiC samples analyzed.

5.2 PALS Measurements

PALS measurements were made on all four samples. Using the fast-fast PALS spectrometer described in Ross [13] with identical settings and T-112A as the positron source, each of the samples were examined. Spectrum collection times were determined by recording the number of counts from a three-minute spectrum and calculating the time required to obtain the recommended 10^6 counts in the lifetime spectrum in order to extract lifetime components and their intensities. Collection times were set to 86,400 sec per measurement to achieve the 10^6 counts. The lifetime spectra for the samples are shown in Appendix B.

Lifetime spectra were processed in order to determine the lifetime(s) and their associated intensities in the samples using PALSfit [90]. PALSfit uses a least squares fit

process in two modules, Positronfit and Resolutionfit, to extract the various lifetime components and resolution function from the measured lifetime spectra. The PALSfit analyses procedure used was outlined by Williams and Johnson [91].

The lifetime spectra for the SiC samples and PALSfit output listing the best fitting lifetimes and their intensities are displayed in Appendix B. The exponents of three Gaussians describing the optimum resolution function were calculated to be 202 psec, 324 psec, and 1.135 psec and their associated intensities were 83 %, 11 %, and 6 %, respectively. The Cu lifetime spectrum was analyzed twice using the same resolution function. Once with all lifetimes guessed (the unconstrained analysis) and once with the Cu lifetime of 120 psec fixed (the constrained analysis). The 120 psec fixed lifetime for single-crystal Cu was the result previously measured by Robles et al [92]. In the unconstrained analysis, lifetimes of 115 ± 2 psec with an intensity of 59 ± 0.4 % and 492 ± 6 psec with an intensity of 36 ± 0.6 % were extracted and attributed to the Cu and the source contribution, respectively. To accurately quantify the source's contribution, a second analysis was conducted fixing the Cu lifetime to 120 psec. Two other lifetimes were extracted: 420 ± 5 psec with an intensity of 34 ± 0.9 % and the 635 ± 10 psec with an intensity of 8 ± 1.1 %. The 420 psec lifetime was attributed to the source contribution to the lifetime spectrum. Since the variance of the fit for both the unconstrained and constrained analysis were approximately equal (1.009 and 1.016, respectively), and the difference in the Cu lifetime between the two analyses was extremely small, there was no bias introduced from constraining the Cu lifetime. Therefore, the 420 psec lifetime for the source contribution to the spectrum was fixed in all subsequent PALSfit analyses. Next, the SiC lifetime spectra were analyzed.

First, the virgin SiC lifetime spectrum was analyzed. Fixing the source lifetime, a lifetime component of 139 ± 8 psec with an intensity of 73 ± 0.4 % was extracted and attributed to the bulk, virgin SiC, which is in good agreement with the bulk 6H SiC lifetime of 136-148 psec reported in Table 3. Next, the ion irradiated and annealed sample was analyzed with the bulk virgin SiC and source lifetimes fixed. The resulting lifetime of 286 ± 4 psec with an intensity of 23 ± 0.8 % was attributed to the O atoms in the SiC. Finally, the lifetime spectra for the ion irradiated and un-annealed SiC was analyzed with the bulk virgin SiC, O atom and source lifetimes fixed. Unfortunately, PALSfit cannot resolve more than 4 lifetimes well, and the resulting lifetime of 205 ± 8 psec, represents a convolution of all the vacancy-type defects present in the un-annealed sample. This lifetime, though, does fall within the lifetime ranges for V_{Si} , V_C and $V_C V_{Si}$, described in Table 3. Even though all three defect types were expected, a specific defect was not determined. It was important just to measure the presence of the defects. The differing lifetimes and intensities strongly suggested there was a measurable difference in the momentum distributions of the e^-e^+ pair prior to their annihilation between the ion irradiated and un-annealed 6H SiC sample when compared to the annealed sample, since a significant number of positrons interacted with the defects. Also, the lack of a fourth lifetime in the annealed lifetime spectrum indicated that the annealing process annealed out many of the vacancies produced during the thermalization of the O^+ ion, relative to the concentration of O atoms.

5.3 Virgin Cu 2D ACAR Response with No Compensation for DSSD Efficiency

To evaluate the simultaneous 3D momentum capability of 3DPASS, the 3DPAMM data set for single-crystal Cu without compensating for the varying efficiency across the DSSD charge collection strips was collected. The 2D ACAR spectrum was reconstructed, shown in Figure 43, following the procedure outlined in Sections 4.8 and 4.9. A total of 1.12×10^6 annihilation events were observed in this data set. The 2D ACAR spectrum was populated by processing coincident annihilation events using the interpolation method (Equation (33)) to determine event location. Note the “neck” feature at the peak of the momentum distribution and the slight misalignment of the distribution relative to the Z-axis.

A benefit of using Cu to calibrate the ACAR spectrum was that the spectrum’s inherent symmetry was used to precisely correct the sample/detector misalignment, which is better visualized in the contour plot of the Cu 2D ACAR spectrum shown in Figure 44. The momentum distribution should be centered on the Z-axis which it was not, indicating the source/sample combination was not axially aligned relative to the DSSDs. The system was 3.12 mm off in the X-direction and 2.51 mm off in the Y-direction, which was corrected by re-aligning the sample vacuum chamber, relative to the DSSD faces by the distances indicated by the contour plot.

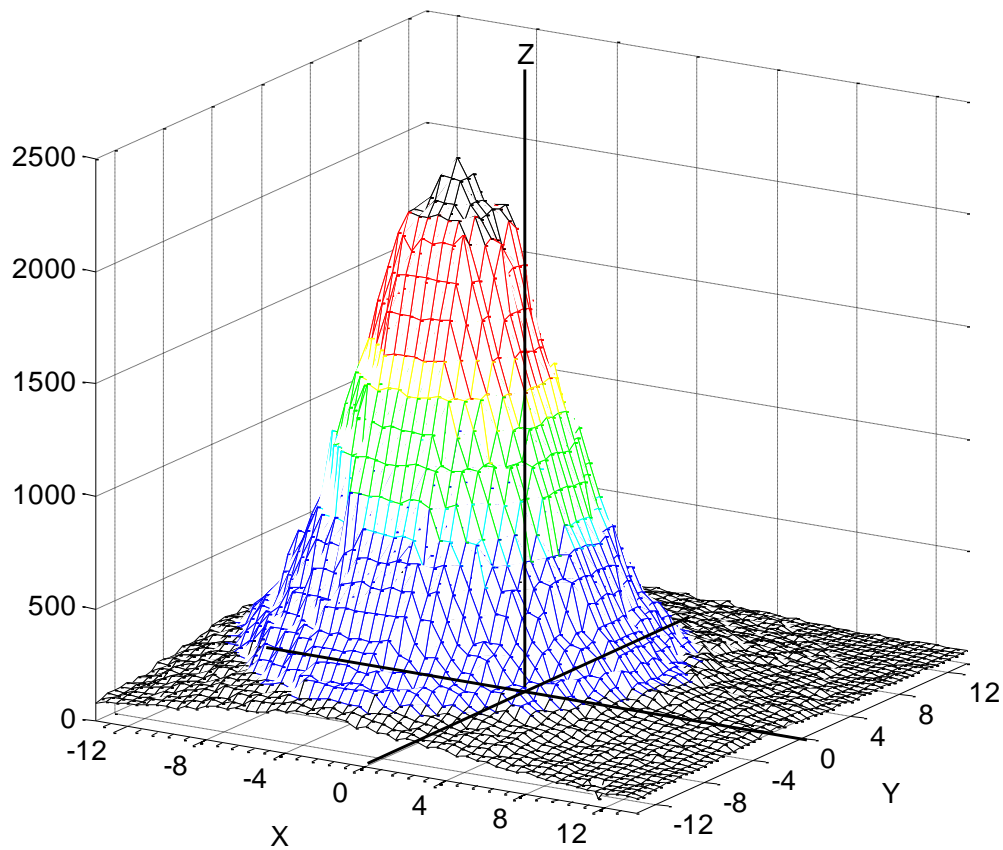


Figure 43. Single-crystal Cu 2D ACAR spectrum reconstructed from the 3DPAMM data set. X and Y units are in mrad or $10^{-3} m_0c$ (in momentum space) and Z is the number of counts. Note the “neck” at peak of the momentum distribution.

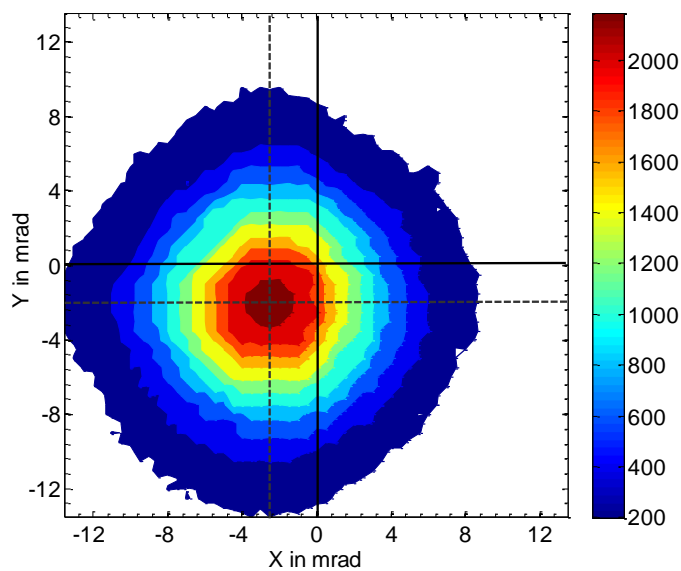


Figure 44. Contour plot of Cu ACAR momentum distribution displaying misalignment of sample and detectors.

The ACAR response of 3DPASS was evaluated using two alignment-corrected projections at $X = 0$ and $Y = 0$, one set consisted of the unsmoothed data and the other, slightly smoothed using a Savitsky-Golay 2nd order polynomial filter over a frame size of 5 data points. The smoothed projections, shown in Figure 45, compared closely to scaled ACAR data for single-crystal Cu collected by Senicki et al [93], measured using the 1D long-slit ACAR technique. The un-smoothed projections, however, exhibited notches at distinct angles in the raw Cu spectra. By applying the slight smoothing routine, these features were greatly reduced.

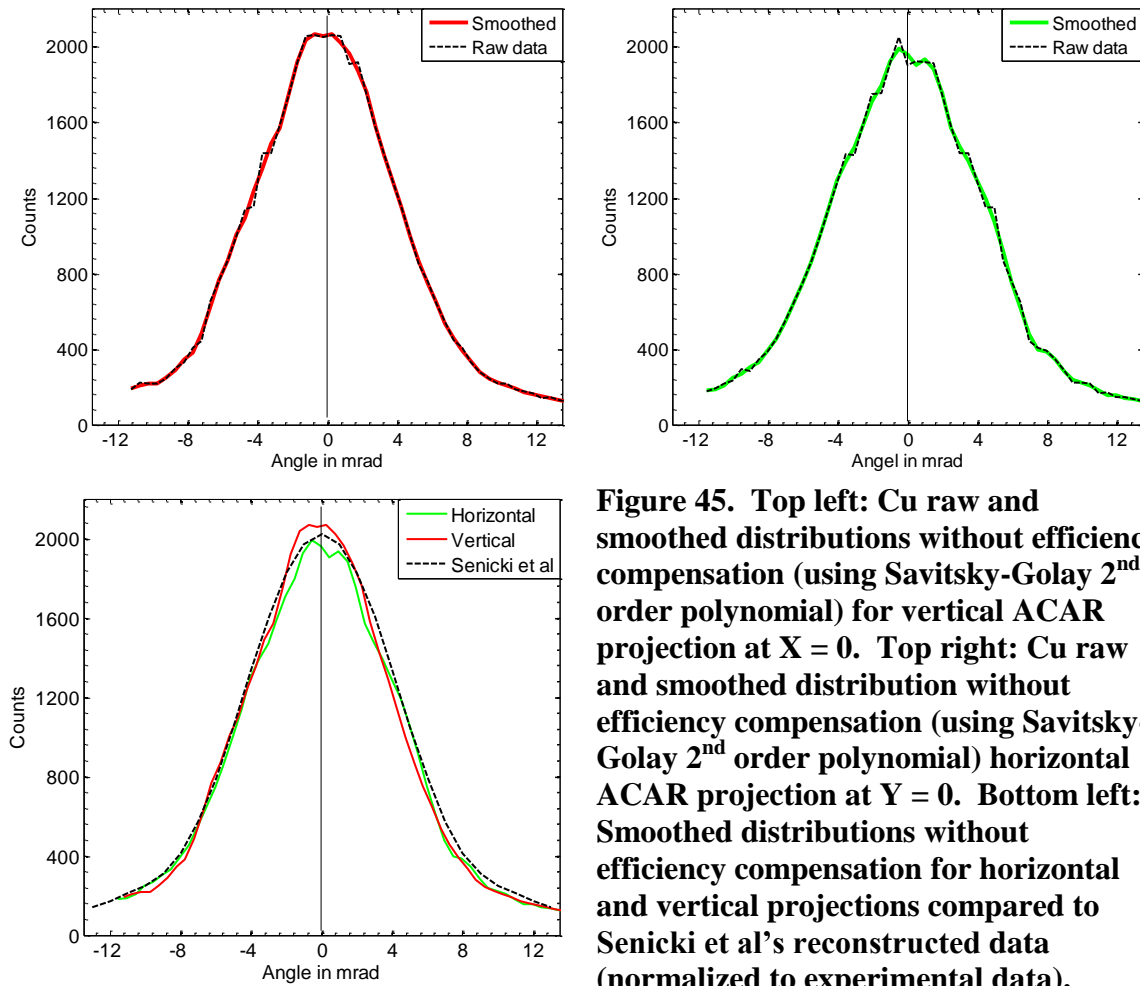


Figure 45. Top left: Cu raw and smoothed distributions without efficiency compensation (using Savitsky-Golay 2nd order polynomial) for vertical ACAR projection at $X = 0$. Top right: Cu raw and smoothed distribution without efficiency compensation (using Savitsky-Golay 2nd order polynomial) horizontal ACAR projection at $Y = 0$. Bottom left: Smoothed distributions without efficiency compensation for horizontal and vertical projections compared to Senicki et al's reconstructed data (normalized to experimental data).

The appearance of these features on the sides and the “neck” at the peak were most likely the result of one or more of the following. First, a decrease in efficiency in the charge collection strips was observed the closer events occurred to the edge of the strips. This could have distorted the spectrum depending on which subpixels detected the annihilation photons. This is addressed in the next section when the efficiency across the charge collection strips of the DSSDs is addressed. Second, many positrons from the ^{22}Na source probably interacted and annihilated with the vacuum chamber materials, causing momentum data from those annihilations to alter the Cu momentum data. Focusing a narrow stream of positrons directly into the sample instead of using the isotropic radiation from a planchette source, would have minimized positron interactions with materials other than the sample, reducing the extraneous “background” contributions to the momentum spectra. Finally, the Cu sample was oriented 45° relative to the face of the DSSDs face, where Senicki et al’s sample orientation was orthogonal. The slight anisotropy of Cu as discussed by Tanigawa et al could have contributed to the observed features. This especially holds true for the neck at the peak because the ACAR spectra perpendicular to the (111) orientation of the Cu does exhibit a noticeably defined neck at the peak of the momentum distribution. Since the Cu 3D momentum distribution was highly symmetric, these features surfaced in some form in the DBAR spectrum.

5.4 Virgin Cu 2D ACAR Response Compensated for DSSD Efficiency

The same 3DPAMM data set for single-crystal Cu was analyzed again, this time compensating for the varying efficiency across the DSSDs’ charge collection strips using Equation (34). The 2D ACAR distribution was reconstructed following the procedure

outlined in Sections 4.8 and 4.9. The shape of the 2D ACAR momentum distribution compensating for the efficiency was visually indistinguishable from the spectrum without the efficiency compensation (Figure 43). The distribution was equally off-centered by the dimensions mentioned above since the same data set was analyzed. The peak intensity in the compensated distribution scaled to 5053 counts, however, versus the 2167 counts in the uncompensated distribution. The neck feature was still present. Additionally, the error in the efficiency compensation was small, even at large angular deviations, compared to the uncorrected distribution, indicating the compensation was not erroneously biasing the spectrum.

The ACAR response of 3DPASS, compensated for strip efficiency was evaluated using two alignment-corrected projections at $X = 0$ and $Y = 0$, one set consisting of the unsmoothed data and the other of slightly smoothed data using a Savitsky-Golay 2nd order polynomial filter over a frame size of 5 data points, like in Section 5.3. The raw and smoothed projections compensated for the DSSD efficiency are shown in Figure 46. The smoothing routine provided virtually no difference when compared to the raw data. With the exception of the neck feature, the notches on the sides of the projection seen in the uncompensated projections disappeared. This suggested the notches on the sides of the projections were not due to the e^-e^+ momentum distribution in Cu, but rather were an artifact resulting from the preferential subpixel observations of annihilation events due to the strip efficiencies in the DSSDs. Next, the projections were compared to the momentum distribution for single-crystal Cu collected by Senicki et al [93], scaled to the area of the experimental distributions. With the exception of the neck near the peak, the experimental distribution compared extremely well with Senicki et al's results.

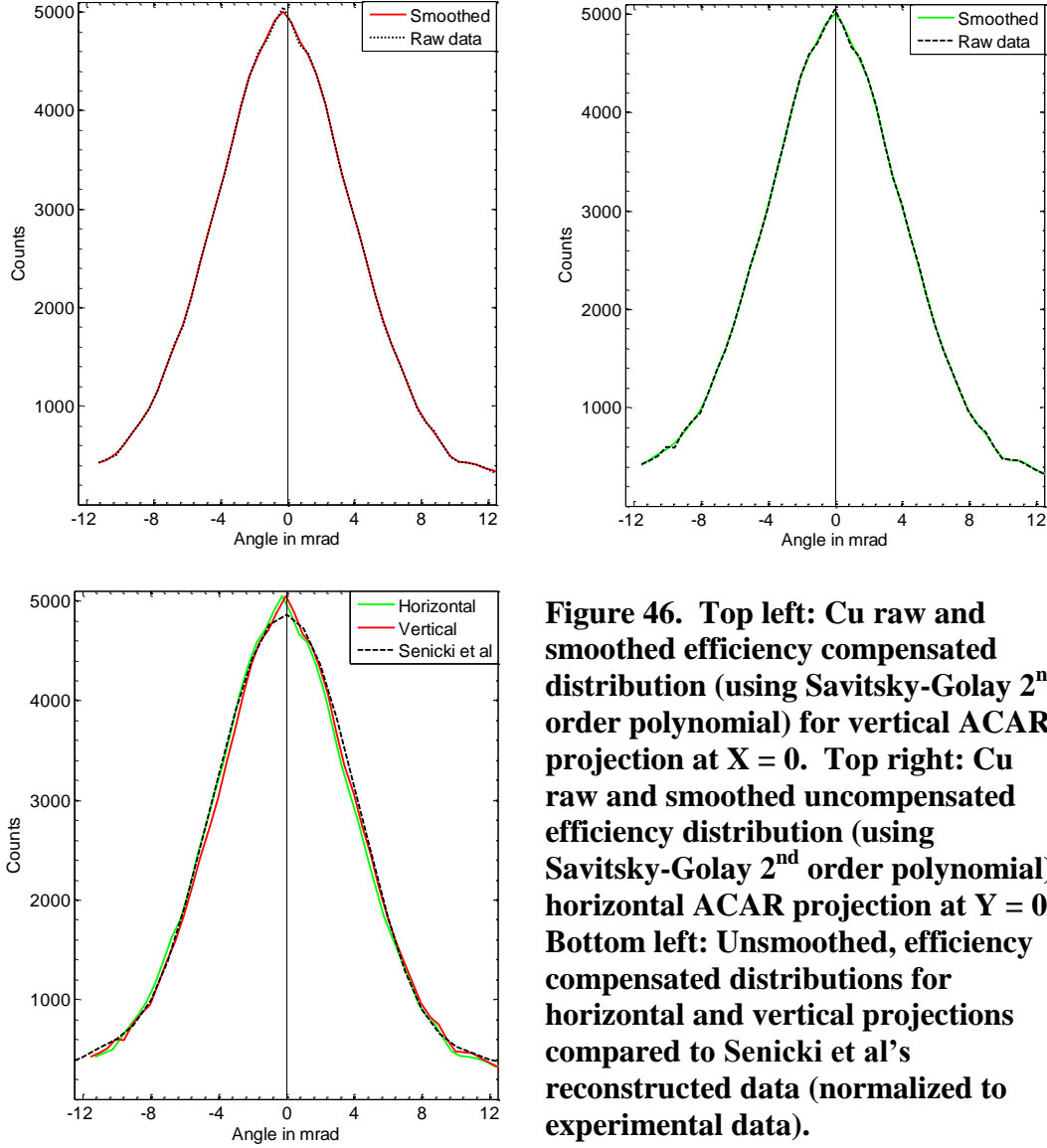


Figure 46. Top left: Cu raw and smoothed efficiency compensated distribution (using Savitsky-Golay 2nd order polynomial) for vertical ACAR projection at X = 0. Top right: Cu raw and smoothed uncompensated efficiency distribution (using Savitsky-Golay 2nd order polynomial) horizontal ACAR projection at Y = 0. Bottom left: Unsmoothed, efficiency compensated distributions for horizontal and vertical projections compared to Senicki et al's reconstructed data (normalized to experimental data).

With the disappearance of the notches on the sides of the experimental distribution by compensating for the efficiency across the DSSD strips, and the lack of the neck feature disappearing, it was reasonable to conclude the neck feature was real and most likely a function of the sample orientation as discussed above. The neck features occurred at ± 1.2 mrad, corresponding to $1.2 \times 10^{-3} m_0 c$ in momentum space. This neck

feature was present in both axial directions, suggesting the feature was symmetric around the z-axis.

Next, the derivative of each projection was calculated using the difference method and plotted to determine if any hidden features existed. The derivative plot is displayed in Figure 47. Both projections' derivatives were virtually identical. Four changes in the derivatives of the projections at $X = 0$ and $Y = 0$ were observed, centered at $\pm 1.2 \times 10^{-3} m_0 c$, $\pm 2.0 \times 10^{-3} m_0 c$, $\pm 4.0 \times 10^{-3} m_0 c$, and $\pm 6.0 \times 10^{-3} m_0 c$. The feature centered at $\pm 1.2 \times 10^{-3} m_0 c$ correlated to the neck feature and represented the large contribution to the spectrum resulting from positron interaction with low momenta valence electrons.

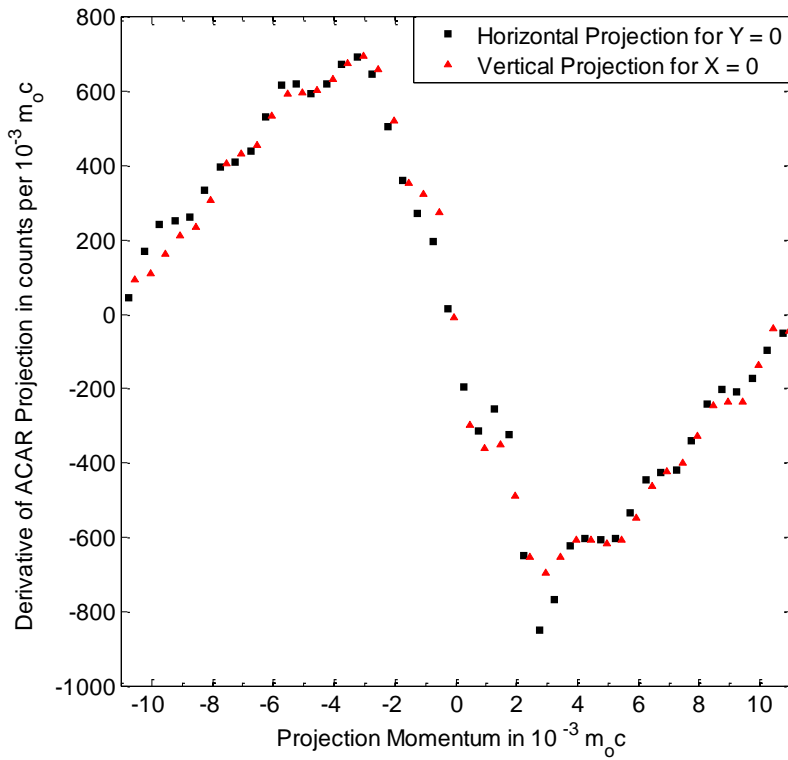


Figure 47. Derivative of X and Y = 0 projections extracted from Cu ACAR spectrum. Black squares represent the horizontal projection and the red triangles represent the vertical.

The large change in the derivative from 0 to $\pm 2.0 \times 10^{-3} m_o c$, representing the dominant interaction of positrons annihilating with delocalized valence electrons, appeared superimposed onto an evenly spaced fine structure. The fine structure consisted of the features centered at $\pm 2.0 \times 10^{-3} m_o c$, $\pm 4.0 \times 10^{-3} m_o c$, and $\pm 6.0 \times 10^{-3} m_o c$, evenly spaced with a separation of $\sim 2 \times 10^{-3} m_o c$. The contribution to the momentum distribution from core electrons is minor because they are tightly bound to the ion cores and the positron must overcome the nucleus' coulomb repulsion to annihilate with the core electron. For single-crystal metals, any effects representing positron interaction with core electrons correspond to x-ray absorption energies. On the other hand, contributions from valence electrons dominate because valence electrons are free move within the metallic crystal and are easily attracted to the positron as it samples the lattice.

2D ACAR spectra represent projections of the e^-e^+ density in momentum space ($\rho(\mathbf{K})$). If the momentum contribution of the positron, compared to the larger momentum contribution of the electron, is neglected then the momentum of the electron can be described by the expression:

$$\rho(\mathbf{K}) = \sum_{\mathbf{G}} \rho(\mathbf{k} + \mathbf{G}) \quad (38)$$

where $\rho(\mathbf{k})$ is the momentum contribution from the direct lattice and $\rho(\mathbf{G})$ is the momentum contribution from scattering within the reciprocal lattice [94,18-51]. The sum is over all occupied reciprocal lattice vectors to account for all scattering possibilities. In covalent solids, such as 6H SiC, contributions from $\rho(\mathbf{G})$ become significant. In metals, however, $\rho(\mathbf{G})$ is small and reflects a perturbation on the momentum contribution from the direct lattice, $\rho(\mathbf{k})$. Therefore, the fine structure observed in Figure 47 corresponds to

$\rho(G)$ for the Cu and correlates with x-ray absorption energies. This will prove useful in the sections ahead.

5.5 Virgin Cu 2D CDBAR Response

To investigate the CDBAR performance of 3DPASS, the CDBAR spectrum was populated following the procedure outlined in Section 4.9, using the same events in the 3DPAMM data set analyzed in the above ACAR analysis. The CDBAR spectrum for single-crystal Cu is displayed in Figure 48. This data was not smoothed.

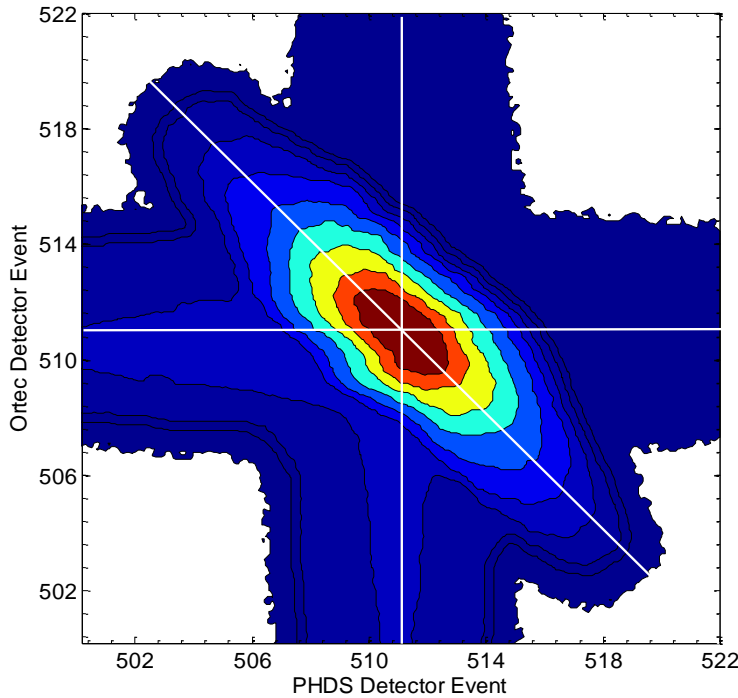


Figure 48. Single-crystal Cu CDBAR spectrum using same events used in the 3DPAMM data applied in the ACAR analysis (not smoothed).

Notice the 6.1-keV width orthogonal to the DB lineshape's base. This was wider than the DB lineshape width of 4.0 keV used by Baranowski et al and most likely a result of the larger energy resolution of the DSSDs' in 3DPASS. 3DPASS had an average

energy resolution of 1.63 keV, whereas Baranowski et al had an energy resolution on the order of 1.2 keV. While the resolution should have had minimal affect on the shape of the DB lineshape, as discussed by Baranowski et al, the resolution did affect the shape of the CDBAR distribution.

The DB lineshape was extracted from the Cu CDBAR spectrum for coincident annihilation events. DB lineshapes were constructed with Δ , in Equation (36), varied from zero, in increments the size of the CDBAR's bin dimensions, 0.1 keV, until the full-width at 1/100th maximum (FW(1/100)M) of the lineshape reached a minimum. The FW(1/100)M decreased from 11.4 keV at $\Delta = 0$ keV to 10.8 keV at Δ 's of 0.3 and 0.4 keV. The FW(1/100)M then increased at $\Delta = 0.5$ keV to 10.9 keV. Three of the results are shown in Figure 49; representing Δ 's equal to 0, 0.3, and 0.5 keV (the blue line indicated the FW(1/100)M in each DB lineshape) and the green arrows indicated features observed in the momentum distributions.

All three resulting Cu DB lineshapes of varying width compared favorably with the scaled annihilation lineshape measured by Szpala et al's in both the high and low momentum regions, except for the slightly larger background contribution on the low-energy side of the DB lineshape and two symmetric shoulders on the sides of the lineshape. As Δ increased from zero, the difference of the slightly larger background contribution on the low-energy side relative to the background on the high-energy side, decreased. Additionally, two shoulder features were present at differences in energy of ± 0.3 keV and ± 3.4 keV, corresponding to $1.2 \times 10^{-3} m_0c$ and $13.6 \times 10^{-3} m_0c$ in momentum space, respectively. The magnitude of these two momentum features coincide well with one-third of the value for the K and L x-ray absorption energies for Cu

(9 and 1 keV [95,10-224], respectively). Since the DB lineshape represents a single component of the momentum distribution and the distribution for Cu has been reported as spherically symmetric, the projection of the momentum onto p_{\parallel} would be one-third of the 9 and 1 keV, which was observed by the two shoulder features present in the DB lineshape at ± 0.3 keV and ± 3.4 keV.

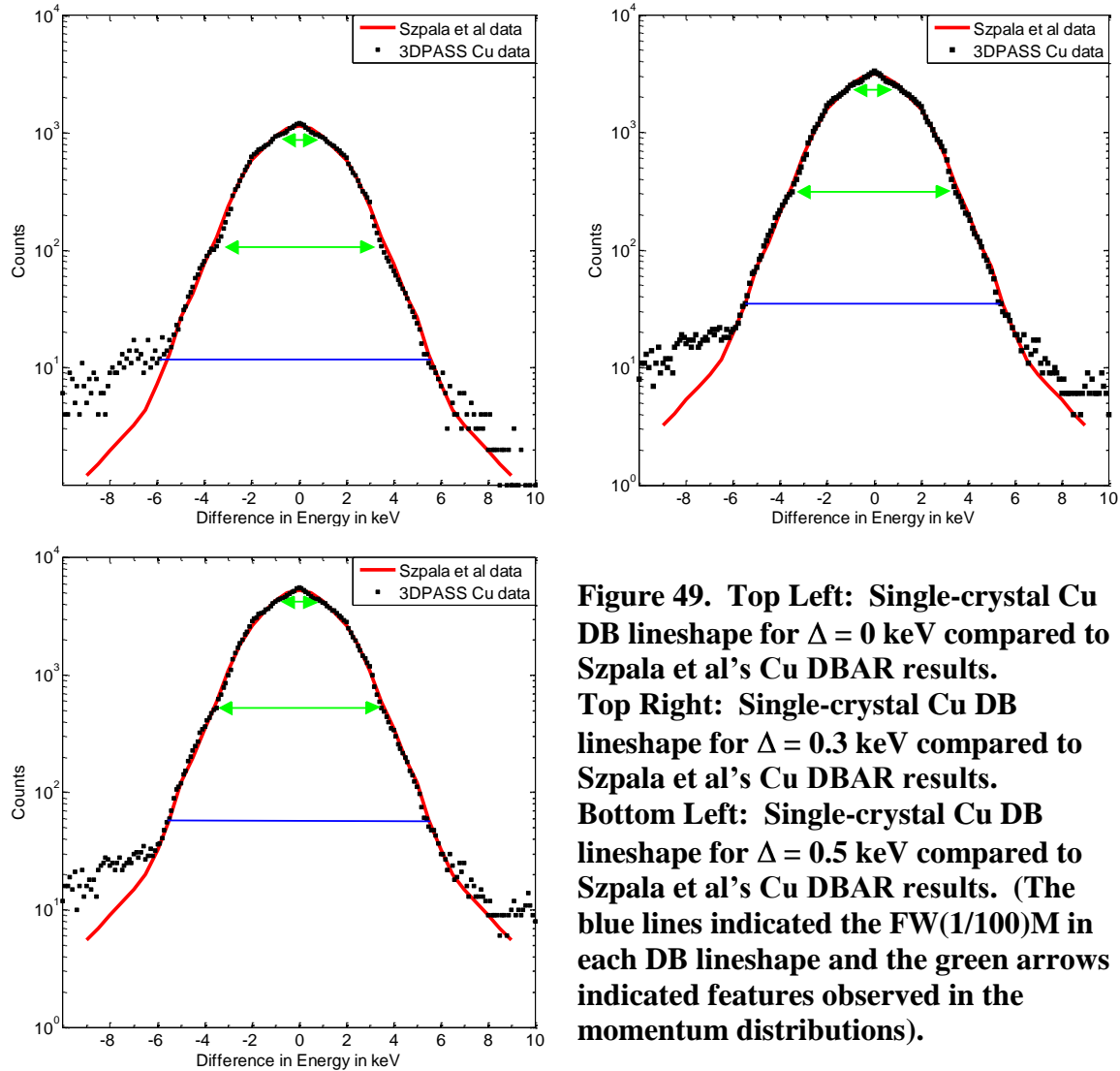


Figure 49. Top Left: Single-crystal Cu DB lineshape for $\Delta = 0$ keV compared to Szpala et al's Cu DBAR results. Top Right: Single-crystal Cu DB lineshape for $\Delta = 0.3$ keV compared to Szpala et al's Cu DBAR results. Bottom Left: Single-crystal Cu DB lineshape for $\Delta = 0.5$ keV compared to Szpala et al's Cu DBAR results. (The blue lines indicated the FW(1/100)M in each DB lineshape and the green arrows indicated features observed in the momentum distributions).

The smaller shoulder DB lineshape feature occurred at the same momentum value as the neck feature present in the ACAR spectra presented above. This indicated this orientation of the single-crystal Cu had a spherically symmetric, localized momentum minimum at $1.2 \times 10^{-3} m_0c$. This feature, unreported in the literature, was most likely caused by the 45° rotation of our sample and influenced by the slight anisotropy of Cu. The large momentum feature at $13.6 \times 10^{-3} m_0c$ was located just outside the angular range of the ACAR spectrum. This feature, also not reported in the literature, occurred in the energy difference range corresponding to positron annihilation with core electrons. The reason for this not being reported on the literature was most likely due to the lack of CDBAR raw data for single-crystal Cu. Published data for single-crystal Cu up to the time of this research was obtained using single-detector DBAR systems. Those systems did not have the background reduction necessary to reveal this feature in the higher momentum region in the DBAR spectrum.

The derivative of the DB lineshape with $\Delta = 0.3$ keV over one (blue) and two bins (red) was calculated and displayed in Figure 50. The two shoulder features present in the DB lineshape at differences in energy at ± 0.3 keV and ± 3.4 keV were observed in the derivative plot, with derivatives of ~ 1300 and ~ 1600 counts/keV, respectively. Two features, also symmetric around zero, present in the derivative plot were not visible in the DB lineshape or the ACAR spectrum, at differences in energy of ± 1.4 keV and ± 2.0 keV, corresponding to $4.8 \times 10^{-3} m_0c$ and $8.0 \times 10^{-3} m_0c$ in momentum space, respectively. The derivative of the feature corresponding to $4.8 \times 10^{-3} m_0c$ was not significantly larger than the surrounding derivatives, ~ 500 counts/keV. The feature

corresponding to $8.0 \times 10^{-3} m_0 c$, however, was ~ 800 counts/keV larger than the surrounding derivatives. Since this feature was not observed in the DB lineshape, it followed the DB lineshape was sensitive to derivatives greater than 800 counts/keV.

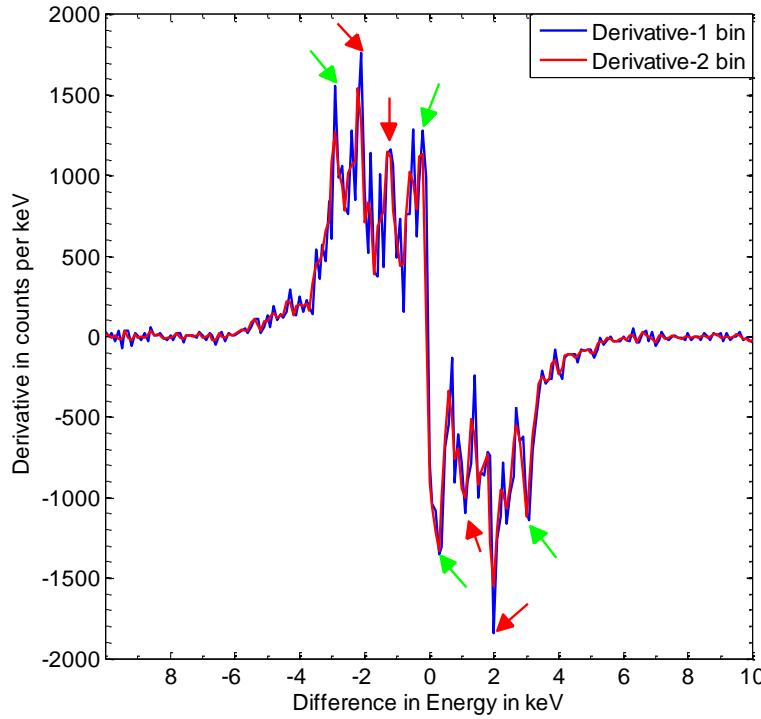


Figure 50. Derivative of DB lineshape with $\Delta = 0.3$ keV for virgin Cu. The blue line represented the derivative over a single bin (0.1 keV) and red represented the derivative over two bins (0.2 keV). Green arrows indicated features observed in green in the DB lineshape and red indicated significant changes in the lineshape's derivative without features present in the lineshape.

The DB lineshape derivative plot, representing the change in the parallel momentum component, was compared to the derivative of the ACAR projections at $X = 0$ and $Y = 0$ (perpendicular momentum component), shown in Figure 51. The derivative of the DB lineshape was not smooth and did not follow the derivatives of the ACAR projections very well. Unfortunately, the DBAR technique was not as sensitive to low momentum events, which was clearly evident by the noise in the derivatives in the parallel momentum component.

The derivative plot was used to extract momenta features in the DB lineshape and ACAR projections by looking for maximums and minimums in the derivatives of the DB lineshape and ACAR projections; minimums for momenta less than zero and maximums for momenta greater than zero. The difference method to calculate the derivatives magnified the error in lineshape as well. To decrease the potential of mis-identifying features with noise, features were identified by two criteria: correlation between DB lineshape features and features in the ACAR projections and confirmed by symmetry of the features about zero momentum.

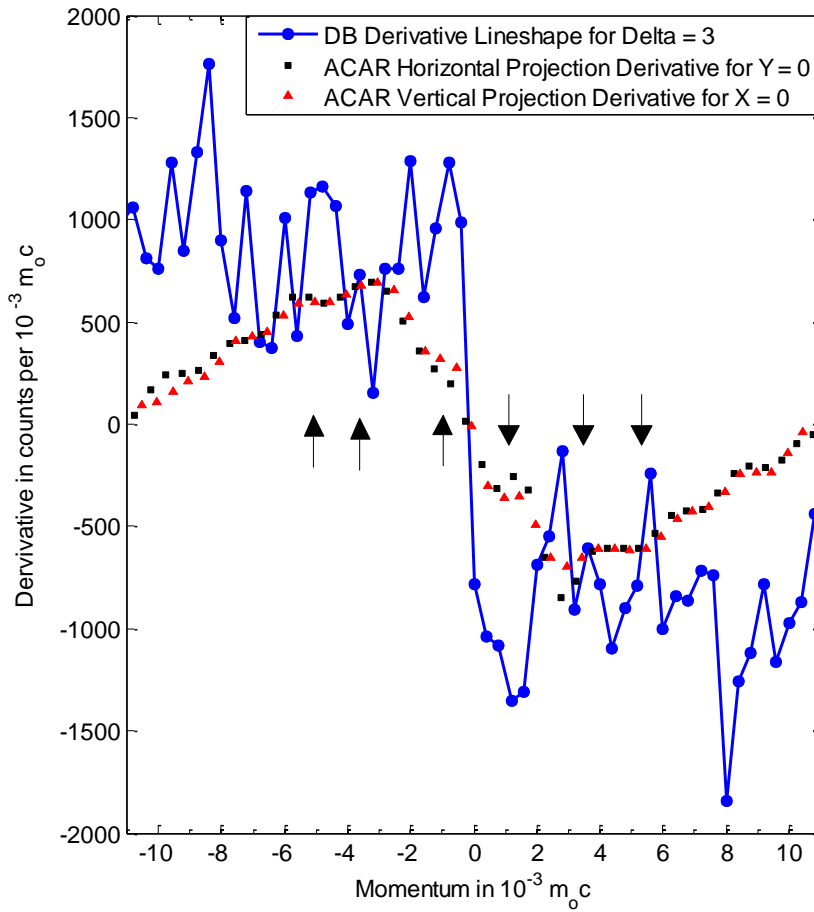


Figure 51.
Derivative plot for momentum components parallel (DB lineshape) and in the plane perpendicular (ACAR vertical and horizontal projections) to the e^-e^+ pair's motion prior to annihilation in single-crystal Cu. Black arrows indicated correlation between ACAR and DBAR features.

The structure observed in the derivatives of the ACAR projections correlated much better with the features in DB lineshape derivative to the right of zero momentum than to the left. Three features, symmetric around zero momentum, centered at ± 1.2 , $\sim \pm 4$, and $\pm 6 \times 10^{-3} m_{o}c$ were observed in both the derivatives of the ACAR projections and the DB lineshape. Correlation of these ACAR and DBAR features signified the momentum distribution in the Cu were spherically symmetric, as suggested in previous research, with the exception of the neck feature observed in the ACAR spectrum. The fact that 3DPASS detected these symmetric features not only further validated the capability of 3DPASS, but also that 3DPASS provided results never documented before.

5.6 Virgin 6H SiC 2D ACAR Response With and Without DSSD Efficiency Compensation

The virgin, un-annealed 6H SiC sample was analyzed using 3DPASS. The data with and without compensating for the varying efficiency across the DSSD subpixels resulting from the 3DPAMM technique was collected and the 2D ACAR spectra were reconstructed. This is shown in Figure 52, following the procedure outlined in Sections 4.8 and 4.9. A total of 1.04×10^6 annihilation events were observed in this data set. Compensating for the efficiency across the DSSDs' strips resulted in a scaled increase in counts. Specifically, the peaks located at (6.0,5.5), (5.0,-4.5), (-6.0,-4.5), and (-7.0,6.5) (using standard x and y coordinates) scaled from 1128 to 2301, 1023 to 2258, 1071 to 2263, and 1114 to 2220, respectively for a $210 \pm 6 \%$ average scaling. While a significant scaling of counts was observed across the momentum distribution, none of the structure was perturbed with the efficiency compensation. In fact, the anisotropies

became more circular and symmetric with the efficiency compensation, which more closely resembled the results by Kawasuso et al.

Several features present in both 3DPAMM-measured spectra compared well with both spectra of differing sample orientations Kawasuso et al measured, as shown in Figure 19. The peaks located at (6,5.5,0), (5,0,-4.5), (-6,0,-4.5), and (-7,0,6.5) in the 3DPAMM data's 2D ACAR spectra, for both the corrected and uncorrected for DSSD subpixel efficiency, correlated with the peaks at the (7,0,4,0), (7,0,-4,0), (-7,0,-4,0), and (-7,0,4,0) locations in Kawasuso et al's spectrum for the P_z along (0001) and P_x along (1100) orientation. Additionally, the peaks at (0,0,10,0) and (0,0,-10,0) in the 3DPAMM spectra were located exactly where Kawasuso et al observed in the P_x along (1100) orientation. The peaks located at (4,0,0,0) and (-4,0,0,0) in Kawasuso's spectrum in the same orientation were not present in the 3DPAMM data. Additionally, the structure in the middle of the 3DPAMM data did not correlate well with the P_z along (0001) and P_x along (1100) orientation, but shared some similarities with the P_z along (0001) and P_x along (1120) orientation. Finally, the direction and relative magnitudes of the anisotropies in the experimental spectrum relative to the center of the spectrum agreed with the direction and relative magnitudes of the bonds between the Si and C atoms in each layer and between layers in the SiC at the 45° sample rotation. This was also confirmed by the observation from Kawasuso et al's results that the propagation direction of the momentum features correlated well with the bonding direction between the Si and C atoms in each layer and between layers for their sample orientation.

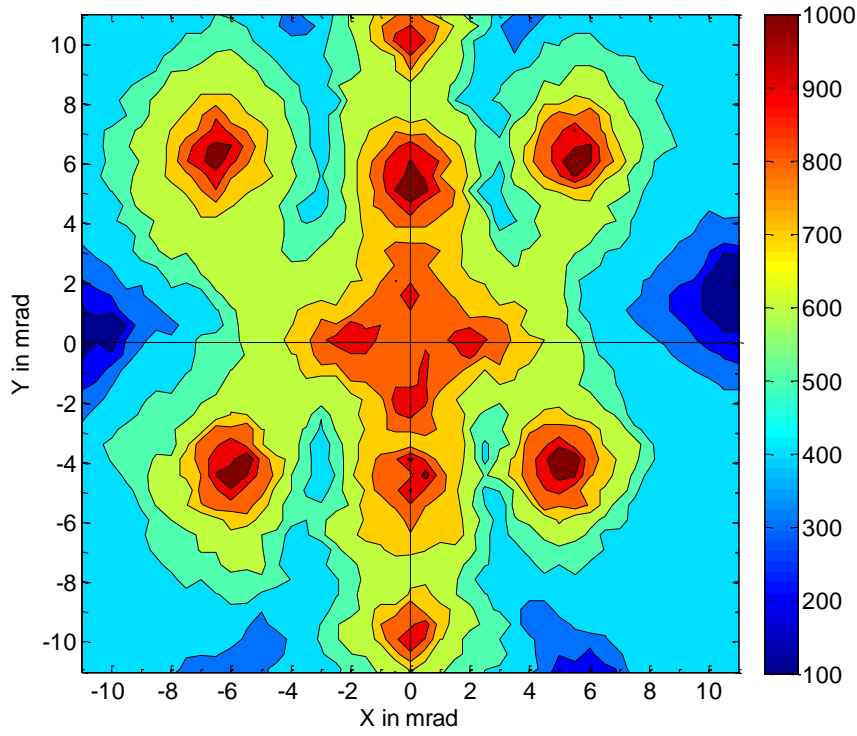
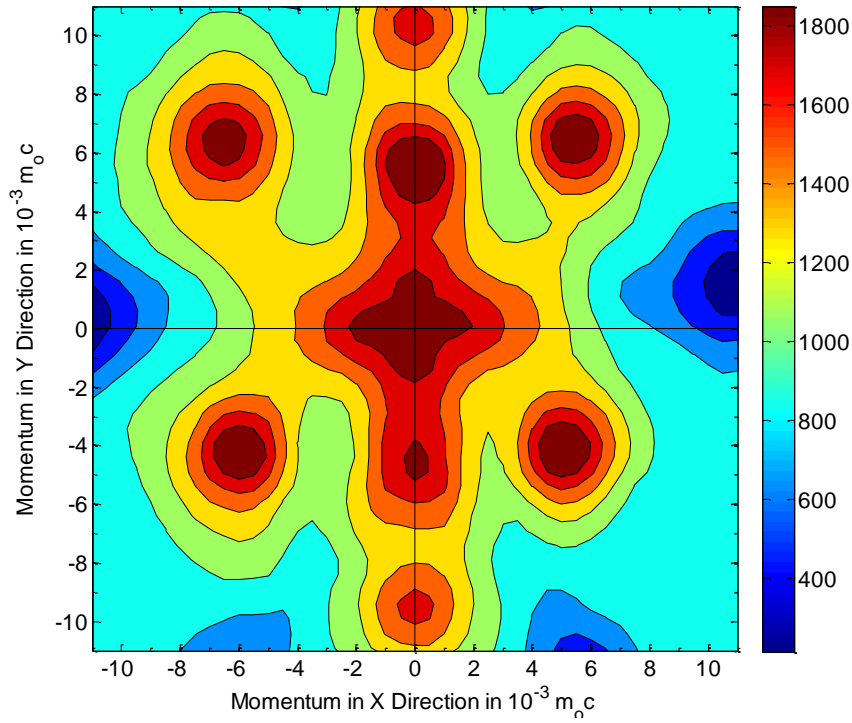


Figure 52.
Top: Virgin,
un-annealed
6H SiC 2D
ACAR without
DSSD efficiency
compensation,
presented in
real space.



Bottom: Virgin,
un-annealed
6H SiC 2D
ACAR with
DSSD efficiency
compensation,
presented in
momentum
space.

Comparing the data from Kawasuso et al in the P_z along (0001) and P_x along (1120) orientation to the 3DPAMM data, the features observed at (2.0,4.5), (2.0,-4.5), (-2.0,-4.5) and (-2.0,4.5) converged from four distinct peaks to two peaks at the (0.0,5) and (0.0,-4.5) locations in the 3DPAMM data. Additionally, the small ridge located in the center, (0.0,0.0), of Kawasuso et al's data was positioned at the same site of the large, diffuse peak that stretched along the axes in the center of the 3DPAMM ACAR spectra. With all these similarities, it was evident, the ACAR spectrum resulting from the 3DPAMM technique compared well with portions of both orientations measured by Kawasuso et al. Since the sample measured by 3DPASS was rotated 45° between both orientations, it was logically concluded the results were consistent with their published ACAR results on similar virgin 6H SiC.

Although the results compared well, one concern did surface. The peaks located at (6.0,6.0), (5.0,-4.0), (-6.0,-4.5), and (-7.0,6.0) in the 3DPAMM ACAR spectrum were not symmetric about both axes, as they were in Kawasuso et al's spectrum. This implied the sample was not positioned properly. The slot in the source/sample tray in the vacuum chamber the sample was held was approximately four times wider than the thickness of the 6H SiC sample. This width was used so that the source/sample tray could accommodate both the thicker Cu and thinner SiC samples. It was reasonable to conclude that the 6H SiC sample tilted in the slot rather than remain exactly vertical, especially when the vacuum was applied to the vacuum chamber. If the sample was not exactly vertical, a slight distortion in the ACAR spectrum could result. To determine if this was the cause of the concern, another data set was collected on the same 6H SiC sample and analyzed, following the same procedure as before.

For the position-corrected, virgin, un-annealed 6H SiC, a total of 0.99×10^6 annihilation events were recorded. The sample was positioned exactly vertically and shimmed to ensure it did not move when the vacuum was applied in the chamber. The features present in the position-corrected 3DPAMM ACAR spectra, shown in Figure 53, centered at (7.0,4.5), (7.0,-4.5), (-7.0,-4.0), and (-7.5,4.0) became more symmetric around the X and Y axes and compared favorably with the peaks centered at (7.0,4.0), (7.0,-4.0), (-7.0,-4.0), and (-7.0,4.0). This confirms that the sample was not exactly vertical, and subsequent measurements were properly shimmed to avoid this distortion.

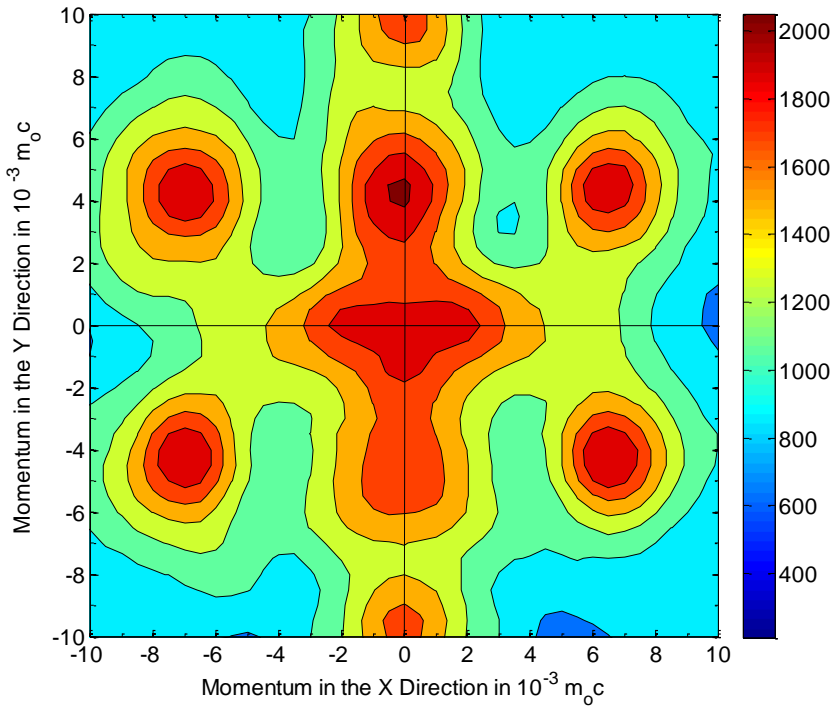


Figure 53. Virgin, un-annealed 6H SiC 2D ACAR with DSSD efficiency compensation and sample position-corrected, presented in momentum space.

Recall, the direction of the momentum anisotropies observed in Kawasuso et al's 6H SiC ACAR spectrum followed the direction of the bonding between the Si and C atoms for the orientation of the SiC they used. The SiC sample 3DPASS interrogated

was rotated 45° from the axis perpendicular to the (100) plane. The first two layers of the unit cell for 6H SiC was modeled in Materials Studio[®] v.4.4.0.0 from Accelrys Software, Inc and rotated 45° on the x-axis, representing the exact orientation of the 6H SiC sample relative to the face of the DSSDs, shown in Figure 54, where red indicated Si atoms and blue indicated C atoms. Superimposing the rotated unit cell fragment onto the ACAR spectrum for the virgin SiC, it was clear that the direction of the momentum of the e^-e^+ pair prior to their annihilation lined up well with the bonding directions in the 6H SiC. Specifically, the anisotropies present in the position-corrected 3DPAMM ACAR spectra centered at (7.0,4.5), (7.0,-4.5), (-7.0,-4.0), and (-7.5,4.0) which projected $\pm 30 \pm 1^\circ$ from the origin along the $\pm X$ axis correlated with the direction of the Si-C bonds between the center atoms and the four corner atoms in the unit cell projection, which projected $\pm 30^\circ$ from the origin along the $\pm X$ axis.

Two slight inconsistencies were noticed at the center of the ACAR spectrum, which widened somewhat along the X-axis and the anisotropies that were observed just above and below the center on the Y axis. These inconsistencies were most likely due to the projection of the bond of the center two atoms, one in front and one in the back, which influenced momentum contributions in both X and Y directions.

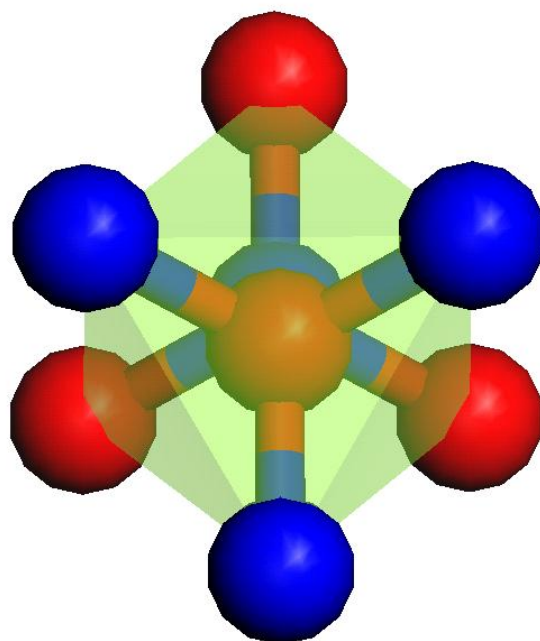


Figure 54. First two layers in 6H SiC unit cell rotated 45° on axis perpendicular to (100) plane. Red indicated Si atoms and blue indicated C atoms.

5.7 Virgin 6H SiC 2D CDBAR Response

The CDBAR spectrum resulting from the 3DPAMM measurement on virgin, un-annealed 6H SiC was populated from the same events used in the above ACAR analysis, following the procedure in Section 4.9. The spectrum is displayed in Figure 55. This data was not smoothed and the same contour levels were used as the ones in the Cu CDBAR spectra (Figure 48). The width orthogonal to the 6H SiC's DB lineshape's base was 6.3 keV versus the 6.1 and 4.0 keV widths in the Cu CDBAR spectrum and the Al spectrum acquired by Baranowski et al, respectively. This indicated the width of the base of the DB lineshape in the CDBAR spectrum was both a function of the energy resolutions of both detectors used and the material the positrons were interrogating. Also, the length of the last contour in the virgin 6H SiC DB lineshape was 3.8-keV longer

than the Cu DB lineshape. This revealed either the positrons or the electrons the positrons were annihilating with had higher momentum in the 6H SiC compared to the Cu. The latter was much more probable since the same positron source was used, and the positrons were near thermal energy.

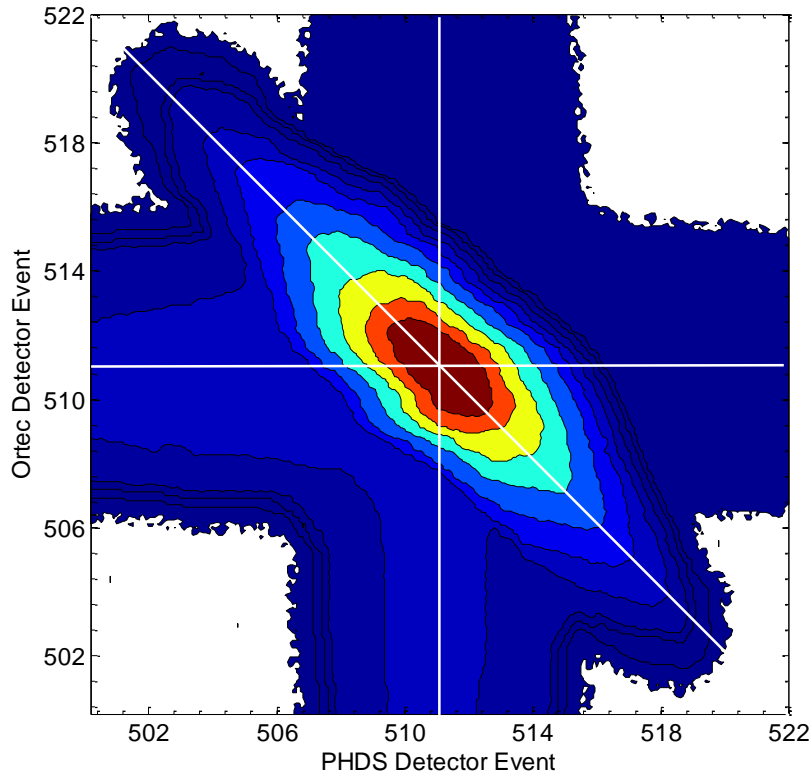
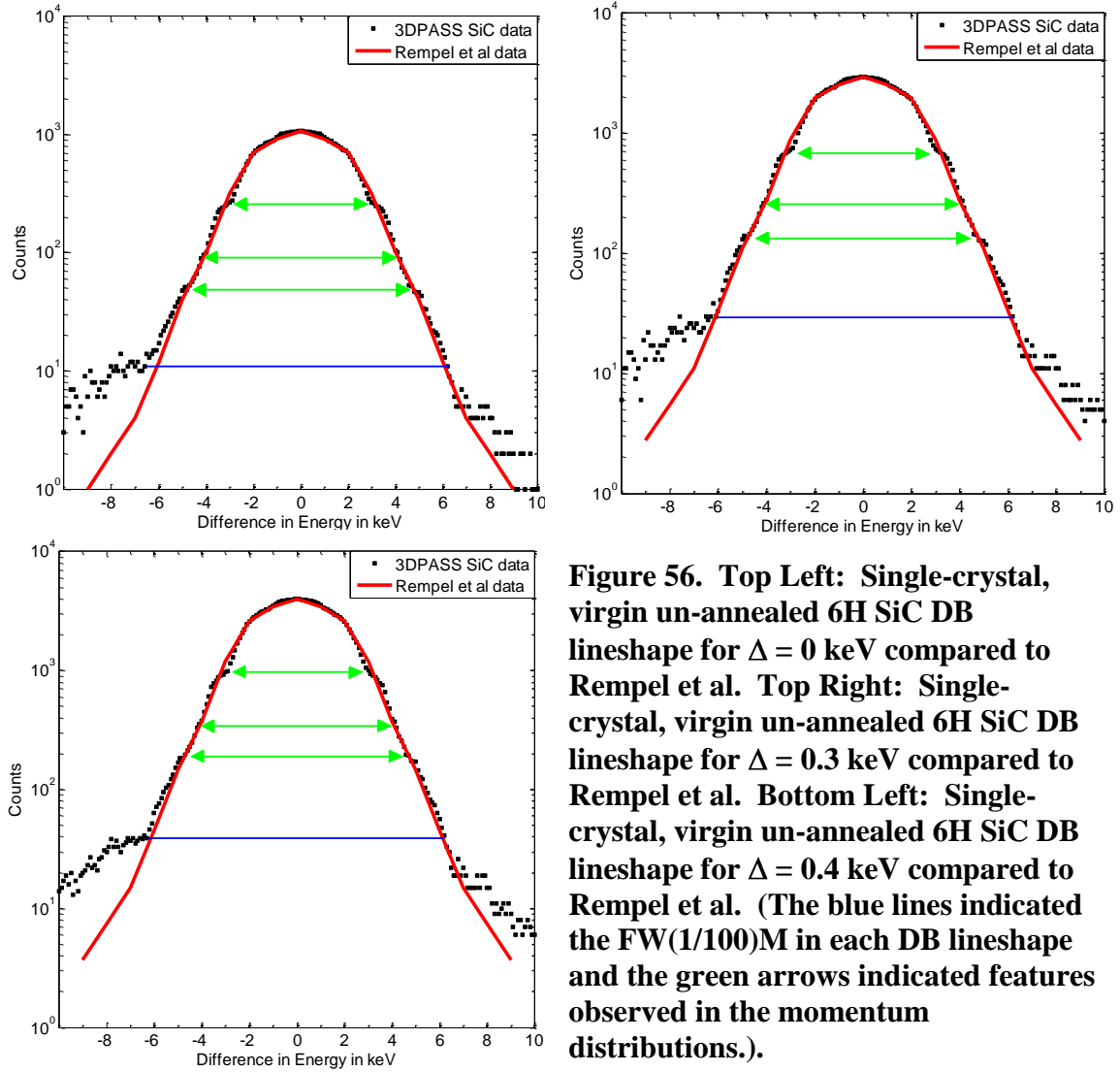


Figure 55. Single-crystal, virgin, un-annealed 6H SiC CDBAR spectrum using the same events from the 3PDAMM data set used in the ACAR analysis (not smoothed).

The DB lineshape was then extracted from the virgin 6H SiC CDBAR spectrum for coincident annihilation events. DB lineshapes were constructed with Δ , in Equation (36), varied from zero, in increments the size of the CDBAR's bin dimensions, 0.1 keV, until the FW(1/100)M of the lineshape reached a minimum. The FW(1/100)M decreased from 12.7 keV at $\Delta = 0$ keV to 12.2 keV at $\Delta = 0.3$ keV. The FW(1/100)M then

increased at $\Delta = 0.4$ keV to 12.4 keV. Three of the results are shown in Figure 56; representing Δ 's equal to 0, 0.3, and 0.4 keV (the blue line indicated the FW(1/100)M in each DB lineshape and the green arrows indicated features observed in the momentum distributions).



All three resulting virgin 6H SiC DB lineshapes of varying width compared favorably with the scaled annihilation lineshape measured by Rempel et al in the low momentum regions, with the exception of three shoulder features observed on the sides of the lineshape. The difference of the slightly larger background contribution on the low-energy side relative to the background on the high-energy side, decreased as Δ increased from zero, similar to the trend for the Cu DB lineshapes presented above. The high momentum portions of the spectrum with greater than a ± 2 keV difference in energy, however, did not compare favorably with the results by Rempel et al.

In the 3DPAMM data set, three shoulder features, symmetric on both sides of the DB lineshape with $\Delta = 0.3$ keV were present at differences in energy of ± 3 keV, ± 4.1 keV and ± 4.4 keV, corresponding to $12.0 \times 10^{-3} m_0c$, $16.4 \times 10^{-3} m_0c$ and $17.6 \times 10^{-3} m_0c$ in momentum space, respectively. The only “feature” Rempel et al observed was a sharp decrease in the slope tangent to the side of the momentum distribution at $\sim 16 \times 10^{-3} m_0c$. The other features observed in the 3DPAMM data set were not reported in published data. Recall Rempel et al incorporated two HPGe detectors to measure the DBAR momentum spectrum. Therefore, the most likely cause for the lack of the features was not a function of the spectrometer but mostly likely due to the difference in sample preparation or that the correlated 3D momentum data biased the data, only allowing certain events to be observed, resulting in the new features. Rempel et al reported they used single-crystal 6H SiC with n-type conductivity of unknown doping levels, procured from Cree, Inc. Although the sample measured using 3DPASS was also n-type and purchased from Cree, differences in the doping of the material could have caused significant differences at the high momentum regions in the distribution.

The derivative of the DB lineshape with $\Delta = 0.3$ keV over one (blue) and two bins (red) was calculated and displayed in Figure 57. The three shoulder features present in the DB lineshape at differences in energy of ± 3 keV, ± 4.1 keV and ± 4.4 keV were observed in the derivative plot, with derivatives of ~ 1600 , ~ 600 and ~ 300 counts/keV, respectively. The latter two features' derivatives were only slightly larger than the surrounding derivative values. Three features, also symmetric around zero, present in the derivative plot were not visible in the DB lineshape at differences in energy of ± 0.3 keV, ± 1.0 keV and ± 2.0 keV, corresponding to $1.2 \times 10^{-3} m_{oc}$, $4.0 \times 10^{-3} m_{oc}$ and $8.0 \times 10^{-3} m_{oc}$ in momentum space, respectively. These features did, however, correspond to features in the ACAR spectrum; namely the centers of the peaks along the axes of the ACAR spectrum and the four peaks centered at (7.1,4.2), (7.1,-4.2), (-7.2,-4.1), and (-7.2,4.1) in the position-corrected 3DPAMM ACAR spectrum. The fact these were present in both the ACAR (p_{\perp}) and DB lineshape (p_{\parallel}) derivative plot implied these features were spherically symmetric. Additionally, DBAR was sensitive to high momentum events, which could be why these unseen low momentum features were absent in the DBAR spectrum but present in the DB lineshape derivative plot which is sensitive to changes in momentum. This was subsequently strengthened by the features in the ACAR spectrum, which is sensitive to low momentum events.

Regardless of these slight features which were absent in the DB lineshape but observed in the derivative plot and ACAR spectrum, the performance of 3DPASS for measuring simultaneous 2D ACAR and CDBAR in a one measurement system compared well with published results for single-crystal, virgin, un-annealed 6H SiC.

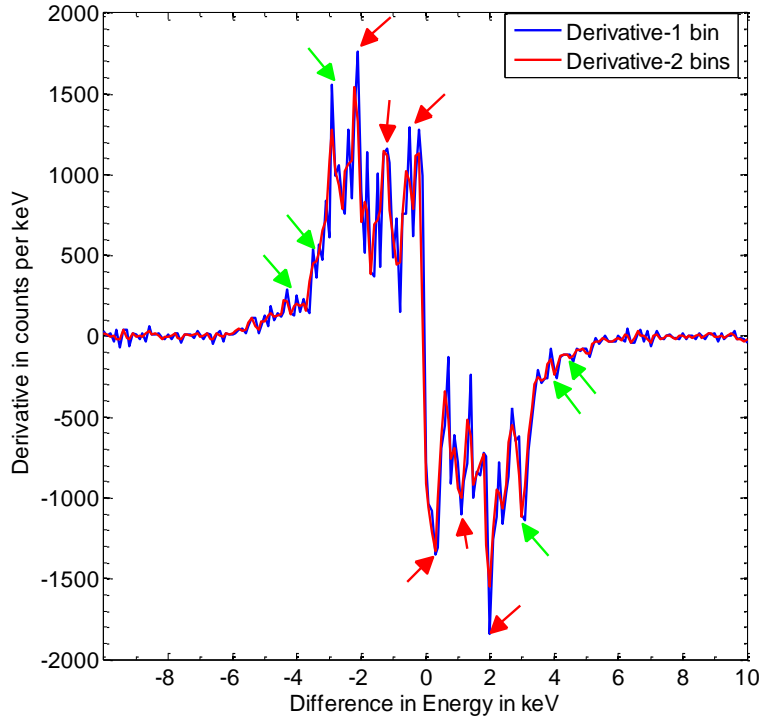


Figure 57. Derivative of DB lineshape with $\Delta = 0.3$ keV for virgin 6H SiC. The blue line represented the derivative over a single bin (0.1 keV) and red represented the derivative over two bins (0.2 keV). Green arrows indicated features observed in green in the DB lineshape with red indicating significant changes in the lineshape's derivative without features present in the lineshape.

5.8 3D Momentum Distribution for Virgin 6H SiC

The 3DPAMM data obtained by 3DPASS contained all three axial momentum components of the e^-e^+ pair prior to annihilation. While this data was readily available, displaying the 3D momentum presented a challenge. In order to fully display the 3D momentum for the e^-e^+ pair prior to annihilation, four dimensions were required. Since this was not possible another method was convenient. The momentum in one component, either the component parallel or the plane perpendicular to the e^-e^+ pair's motion prior to annihilation could be constrained, in any arrangement. For example, momentum features observed in the ACAR or DBAR spectra, and the momentum for the other component with the constraint imposed could be examined. To demonstrate this

capability, this was accomplished for all three SiC samples measured by 3DPASS: virgin and un-annealed, O⁺ ion irradiated and un-annealed and O⁺ ion irradiated and annealed. ACAR momentum anisotropies were treated as the constraint because the entire range of momentum in the ACAR application was contained in the DBAR's momentum range; whereas, the reverse was not true. First, the 3D momentum for virgin, un-annealed 6H SiC was determined.

The 3D momentum distribution from the 3DPAMM data set for virgin, un-annealed 6H SiC was analyzed. A square area was extracted from the position-corrected, 3DPAMM 2D ACAR, efficiency uncorrected spectrum encompassing each momentum peak centered at (7.0,4.5), (7.0,-4.5), (-7.0,-4.0), and (-7.5,4.0), specifically from regions in (5.0:9.0,2.0:6.0), (5.0:9.0,-2.0:-6.0), (-5.0:-9.0,2.0:6.0), and (-5.0:-9.0,-2.0:-6.0), where (x₁:x₂,y₁:y₂) represented the area inside in the ACAR spectrum bounded by (x₁,y₁), (x₁,y₂), (x₂,y₁) and (x₂,y₂). The data was extracted from the 3DPAMM data set which was not corrected for the DSSD charge collection strip efficiency, because it was critical that a recorded event in the ACAR spectrum correlated with the same event in the DBAR spectrum; using efficiency corrected data would violate that restriction. The four momentum peak areas contained a total of 1.33×10^5 counts, or 13.4% of the total counts recorded in the 3PDAMM data set.

Next, using the energy difference of the coincident events observed in the ACAR momentum peaks, the parallel component of the momentum distribution was calculated and plotted just like the process followed to construct the CDBAR spectrum. Then, the 3D momentum lineshape was extracted similarly to the DB lineshape, using $\Delta = 0.3$ keV for consistency. This 3D momentum lineshape represented the momentum component

parallel to the e^-e^+ pair's motion prior to annihilation for virgin, un-annealed 6H SiC with the momentum component in the plane perpendicular to the e^-e^+ pair's motion prior to annihilation constrained by the momentum peaks in the ACAR spectrum centered at (5.0:9.0,2.0:6.0), (5.0:9.0,-2.0:-6.0), (-5.0:-9.0,2.0:6.0), and (-5.0:-9.0,-2.0:-6.0). The resulting 3D momentum lineshape is shown in Figure 58.

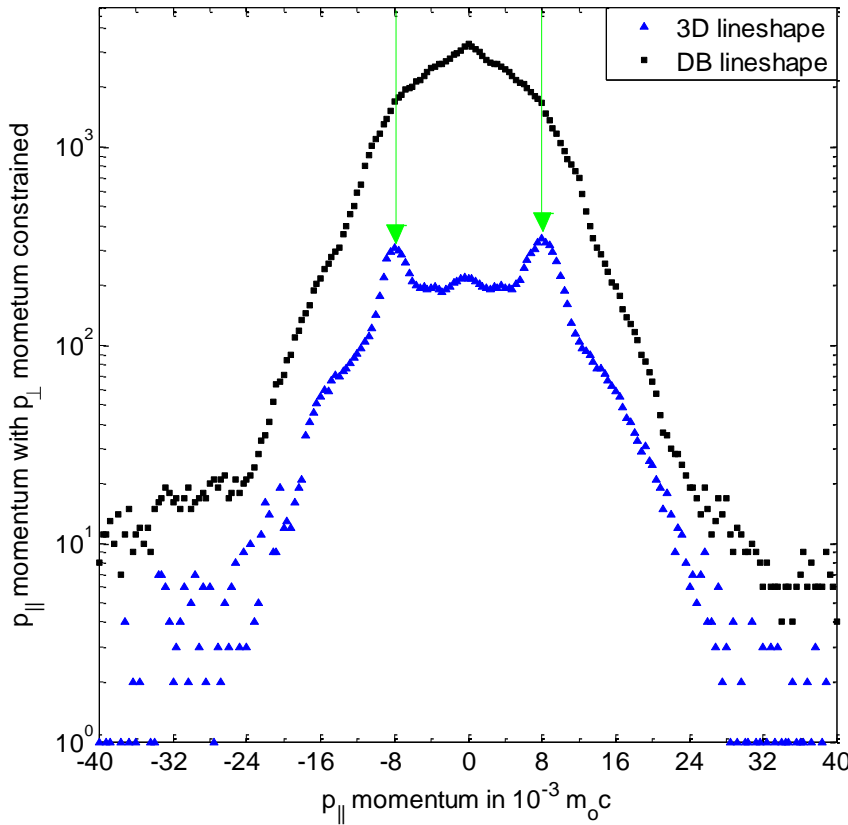


Figure 58. p_{\parallel} component for virgin, un-annealed 6H SiC with p_{\perp} component constrained by the momentum peaks in the ACAR spectrum centered at (5:9,2:6), (5:9,-2:-6), (-5:-9,2:6), and (-5:-9,-2:-6). A $\Delta = 0.3$ keV was used to define the 3D momentum lineshape width of the p_{\parallel} component. Black squares indicated unconstrained DB lineshape and blue triangles represented constrained, 3D momentum lineshape.

The two momentum peaks in the 3D lineshape in the direction parallel to the e^-e^+ pair's motion prior to annihilation corresponded very well to the magnitude of the momentum of the four features that the perpendicular momentum component was constrained to and to the large peaks at ± 2 keV observed in the derivative of the DB

lineshape. This indicated a momentum of $\pm 8.1 \times 10^{-3} m_0 c$ existed in both momentum components, the plane perpendicular and the component parallel to the direction parallel to the e^-e^+ pair's motion prior to annihilation. The widening of the 3D momentum lineshape at approximately $\pm 16 \times 10^{-3} m_0 c$ however, did not correspond to any previously observed feature and most likely was a result of the statistically low number of events in this region of the 3D momentum lineshape. The derivative of the 3D momentum lineshape was calculated and the plot was also constructed, but there were no significant features except for the ones mentioned above. 3D momentum lineshapes were also constructed for the anisotropies centered at (0,4.5 and 0,-4.5) and at (0,10.0) and (0,-10.0), but there was no discernable features within the noise, due to the low number of events that fell into those anisotropies.

To better show the utility and possibilities of analyzing the 3D momentum distribution imbedded in the 3DPAMM data, it would have been useful to constrain the momentum component parallel to the e^-e^+ pair's motion prior to annihilation and examine the momentum distribution of those events in the plane perpendicular to their motion. The ideal constraint would have been to examine events above the cutoff of the core electrons in the parallel momentum component as calculated by Muller et al and explore the momentum distribution in the plane perpendicular to the e^-e^+ pair's motion prior to annihilation. Unfortunately, using only the events with a difference in momentum in the region between $40.0 \times 10^{-3} m_0 c$ and $20.0 \times 10^{-3} m_0 c$ in the DB lineshape with $\Delta = 0.3$ keV to constrain the data and populate a 2D ACAR spectrum with those data points, resulted in considering only 2.7×10^2 events. The 2D ACAR plot was populated using those data points but there was no discernable pattern. Since the DB

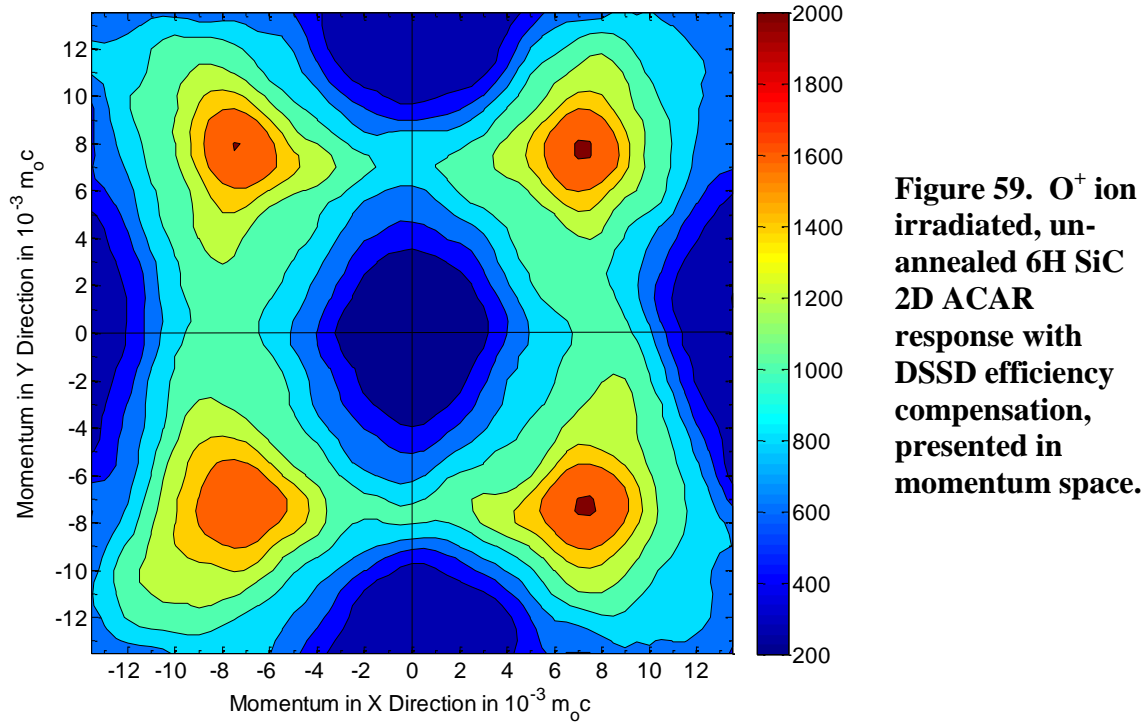
lineshape was a subset of the entire CDBAR spectrum and constraining the DB lineshape was an even smaller subset, it was statistically sound to constrain a subset of the momentum distribution in the plane perpendicular to the e^-e^+ pair's motion prior to annihilation and examine the effect on the parallel momentum component, as accomplished above. This was accomplished for the remaining 6H SiC samples measured using the 3DPAMM technique: the ion irradiated, un-annealed sample and the ion irradiated, annealed sample. Next, the O^+ ion irradiated, un-annealed 6H SiC sample was examined.

5.9 O^+ Ion Irradiated, Un-annealed 6H SiC 2D ACAR Response With DSSD

Efficiency Compensation

The O^+ ion irradiated, un-annealed 6H SiC sample was analyzed using 3DPASS. The data set with and without compensating for the varying efficiency across the DSSD charge collection strips resulting from the 3DPAMM technique was collected and the 2D ACAR spectra were reconstructed. From the previous ACAR results, it was apparent the spectrum corrected for the DSSD efficiency described the momentum distribution best and therefore only the corrected ACAR spectra was presented. The 2D ACAR spectrum for O^+ ion irradiated, un-annealed 6H SiC, compensated for the varying efficiency across the DSSD charge collection strips is shown in Figure 59, following the procedure outlined in Sections 4.8 and 4.9. A total of 1.01×10^6 annihilation events were observed in the uncorrected data set. Compensating for the efficiency across the DSSDs' strips resulted in an scaled increase at the peaks centered at $(7.5, 7.5)$, $(7.5, -7.5)$,

(-7.5,-7.5), and (-7.5,8.0) from 1011 to 2123, 1014 to 2150, 986 to 2130, and 1013 to 2227, respectively for a 212 ± 5 % average scaling.

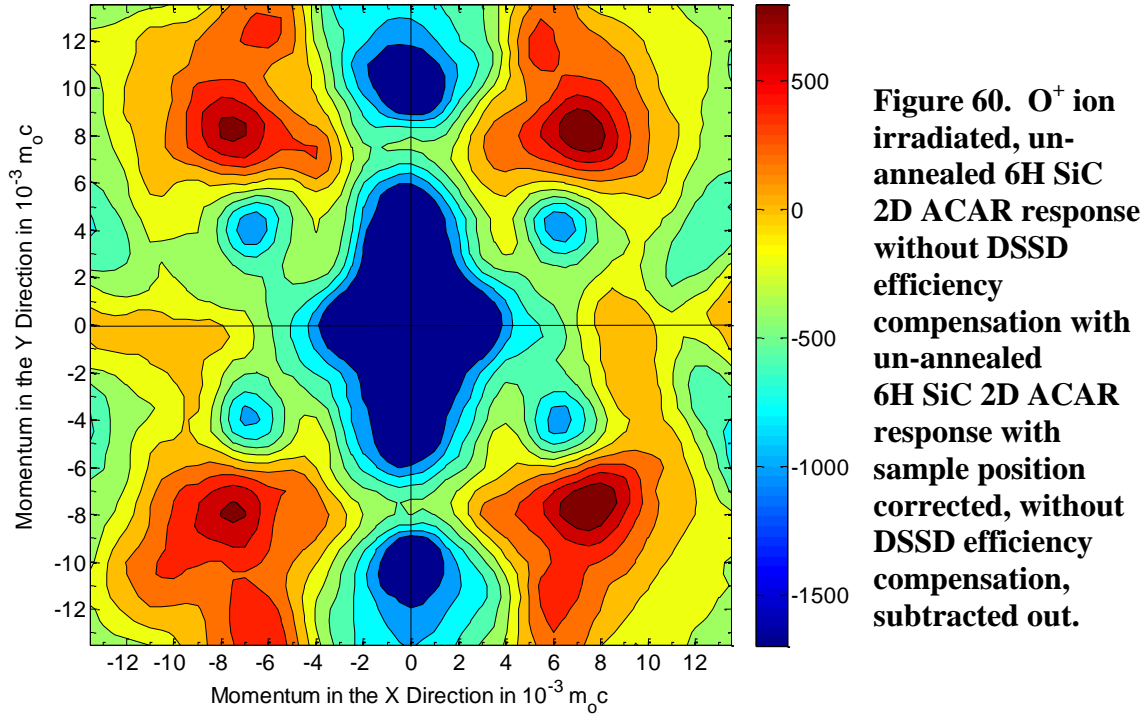


There were no features in the O^+ ion irradiated, un-annealed 6H SiC ACAR spectrum which compared exactly to the virgin, un-annealed 6H SiC ACAR spectrum. The peaks centered at (7.5,7.5), (7.5,-7.5), (-7.5,-7.5), and (-7.5,8.0) however shared a momentum component (in the X direction) with the peaks centered at (7.0,4.0), (7.0,-4.0), (-7.0,-4.0), and (-7.0,4.0) in the virgin 6H SiC spectrum measured by Kawasuso et al. If the observed features in the ion irradiated corresponded to the four features from the spectrum by Kawasuso et al discussed above, which is most likely the case, then the direction of the four observed anisotropies in the ion irradiated, un-annealed spectrum

changed from $\sim 33^\circ$, relative to the X axis, to $\sim 45^\circ$ compared to the virgin sample 2D ACAR spectrum. Additionally, the magnitude of the features increased from $8.1 \times 10^{-3} m_0 c$ to $10.6 \times 10^{-3} m_0 c$. This was most likely due to an increase of annihilations preferentially in one direction in the crystal lattice, which lies in the direction of the shifted anisotropies.

To gain a quantitative understanding of the changes in the momentum distribution in the plane perpendicular to the e^-e^+ pair's motion prior to annihilation in the 6H SiC as a result of the O^+ ion implantation, the virgin spectrum without efficiency compensation was subtracted from the ion irradiated, un-annealed spectrum without efficiency compensation. Since the data sets had approximately the same number of counts, a direct subtraction was taken. The difference plot is displayed in Figure 60. While many of the features present in the difference spectrum were present in either the O^+ ion implanted or the virgin spectra, two differences were noticeable and important to note. First, events with momentum corresponding with the site of the large, diffuse peak that stretched along the axes in the center of the virgin, un-annealed spectrum and the peaks centered at (0,10) and (0,-10) were significantly reduced by the ion implantation. Since those features had an extremely large Y component prior to irradiation, it followed that the ion irradiation resulted in a lower Y component in the momentum distribution. This could have resulted from a slight realignment of the Si-C dipole in the direction of the bonds from either the O atom itself or the vacancy-type defects resulting from the O atom thermalization, which ultimately caused a smaller influence on the momentum component in the Y direction. Second, four small circular regions surfaced in the difference spectrum which indicated a significant increase in events with momenta at (6,12), (6,-12), (-6,-12), and

(-6,12). These were regions of few events with those momenta in the virgin SiC, but after the ion implantation, events with these momenta significantly increased.



It was clearly evident the lattice structure was significantly perturbed by the ion implantation. At this point, it was unclear if the perturbation was due one or a combination of three processes: the O atom thermalizing and stopping between the lattice structure as an interstitial, the vast amount of vacancy-type defects produced by the thermalization of the O ion, or the O atoms localized within the vacancies produced during their thermalization. A definitive cause was determined at this time but a theoretical prediction provided some indication on what caused of the direction of the anisotropies to shift.

Adapting Duan's output into Materials Studio[®] v.4.4.0.0, the optimized geometrical configuration of the O atom interstitially bonded in between the first two layers of the 6H SiC unit cell was constructed and displayed in Figure 61. The orientation of the structure was rotated to allow visualization of the O atom.

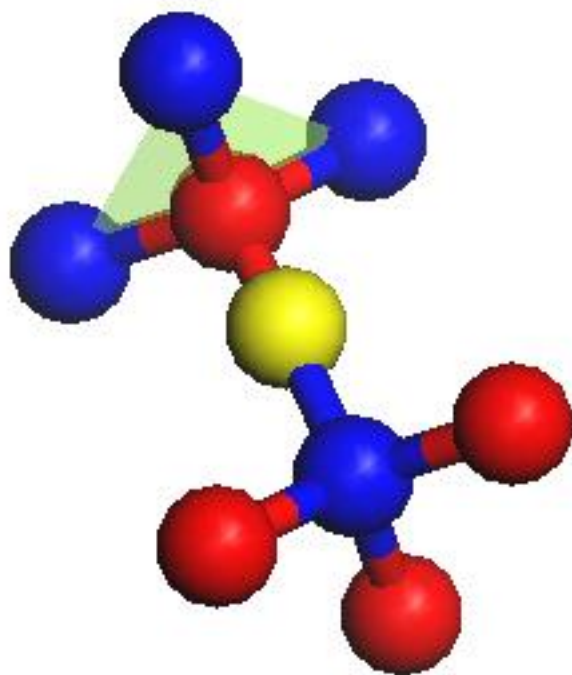


Figure 61. First two layers in 6H SiC unit cell with O atom interstitial. Red indicated Si atoms, yellow indicated O atom and blue indicated C atoms. The orientation of the structure was rotated to allow visualization of the O atom.

Based on Duan's predictions, the distance between the Si and C increased with the O atom interstitial. The anisotropies present in the virgin 6H SiC position-corrected 3DPAMM ACAR spectra centered at (7.0,4.5), (7.0,-4.5), (-7.0,-4.0), and (-7.5,4.0) which projected $\pm 30 \pm 1^\circ$ from the origin along $\pm X$ axis were assumed to have perturbed and shifted to the peaks centered at (7.5,7.5), (7.5,-7.5), (-7.5,-7.5), and (-7.5,8.0) in the O^+ irradiated, un-annealed sample (projected $\pm 45 \pm 1^\circ$ from the origin along $\pm X$ axis). Any vacancy-type defects produced by the thermalization of the O atoms, which were

subsequently filled with the thermalized O atom would not have perturbed the lattice structure to cause the $\sim 15^\circ$ increase in the direction of the bonds, relative to the X axis. The O atom interstitial, however, increased the distance between the Si and C atoms almost two-fold which would significantly influence the Si and C atom locations, thereby shifting the bonding directions. Since the location of the anisotropies present in the O^+ irradiated, un-annealed ACAR spectrum shifted to larger angles relative to the X axis, compared to the virgin sample, it was concluded a portion of the O atoms in the un-annealed 6H SiC sample resided in the SiC as interstitials.

5.10 O^+ Ion Irradiated, Un-annealed 6H SiC 2D CDBAR Response

The CDBAR spectrum resulting from the 3DPAMM measurement on O^+ ion irradiated, un-annealed 6H SiC was populated from the same events used in the above ACAR analysis. The width orthogonal to the spectrum's DB lineshape's base was 6.2 keV versus the 6.3 keV width in the virgin 6H SiC CDBAR spectrum. The DB lineshape was extracted from the ion implanted, un-annealed 6H SiC CDBAR spectrum for coincident annihilation events. DB lineshapes were constructed with Δ , in Equation (36), varied from zero, in increments the size of the CDBAR's bin dimensions, 0.1 keV, until the FW(1/100)M of the lineshape reached a minimum. The FW(1/100)M decreased from 12.4 keV at $\Delta = 0$ keV to 11.7 keV at $\Delta = 0.3$ keV and subsequently increased at $\Delta = 0.4$ keV to 11.9 keV. The DB lineshape corresponding to $\Delta = 0.3$ keV is shown in Figure 62.

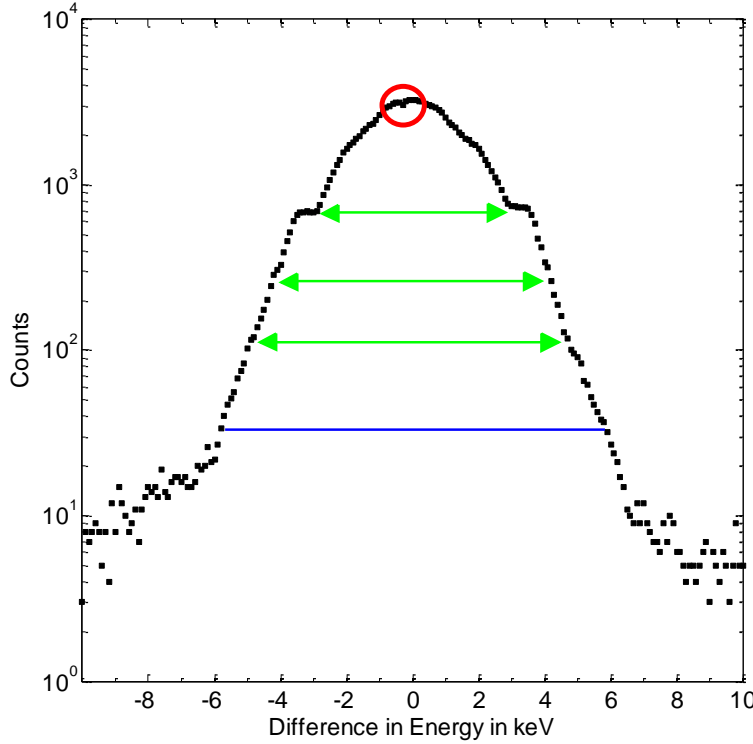


Figure 62. Single-crystal, O^+ ion irradiated, un-annealed 6H SiC DB lineshape for $\Delta = 3$ keV. (The blue line indicated the FW(1/100)M in the DB lineshape).

The difference of the slightly larger background contribution on the low-energy side relative to the background on the high-energy side, decreased as Δ increased from zero, which was also observed in the Cu and virgin DB lineshapes above. The three symmetric shoulder features visible in the virgin 6H SiC DB lineshape at differences in energy of ± 3 keV, ± 4.1 keV and ± 4.4 keV were all not as visible in the ion irradiated DB lineshape. The shoulder at ± 3 keV actually widened, whereas, the shoulders at ± 4.1 keV and ± 4.4 keV became almost unnoticeable. Additionally, a sharp decrease in events was observed, asymmetric around zero at a difference in energy of 0.3 keV, corresponding to $1.2 \times 10^{-3} m_0 c$ in momentum space. The derivative of the DB lineshape was calculated to amplify these and other minor features.

The derivative of the DB lineshape with $\Delta = 0.3$ keV over one (blue) and two bins (red) was calculated and displayed in Figure 63. The three shoulder features present in the virgin 6H SiC DB lineshape at differences in energy at ± 3 keV, ± 4.1 keV and ± 4.4 keV were observed in the ion implanted derivative plot, with derivatives of ~ 0 , ~ 800 and ~ 400 counts/keV, respectively. The latter two features' derivatives were only slightly larger than the surrounding derivative values. Additionally, the feature at $\Delta E = \pm 3$ keV was so wide that the derivative approached zero. Two features, also symmetric around zero, presented as local maximums in the derivative plot were not visible in the DB lineshape at differences in energy of ± 1.0 keV and ± 2.6 keV, corresponding to $4.0 \times 10^{-3} m_0 c$, and $10.4 \times 10^{-3} m_0 c$ in momentum space, respectively. The peak at $\Delta E = \pm 1.0$ keV in the DB lineshape's derivative did not correspond to any feature in the ACAR spectrum but the peak at $\Delta E = \pm 2.6$ keV did.

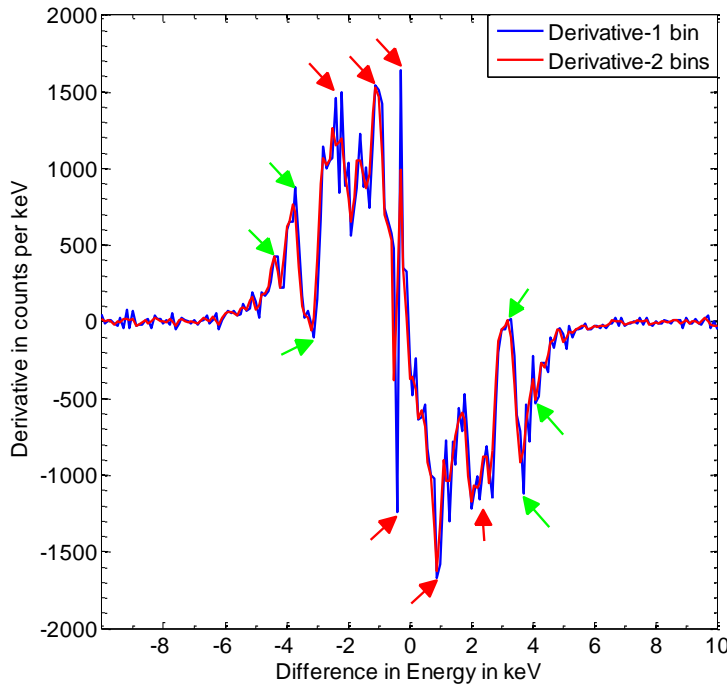


Figure 63. Derivative of DB lineshape with $\Delta = 0.3$ keV for O^+ ion irradiated, un-annealed 6H SiC. The blue line represented the derivative over a single bin (0.1 keV) and red represented the derivative over two bins (0.2 keV). Green arrows indicated features observed in green in the DB lineshape and red indicated significant changes in the lineshape's derivative without features present in the lineshape.

The magnitude of the momentum of the four features centered at (7.5,7.5), (7.5,-7.5), (-7.5,-7.5), and (-7.5,8.0) was simply the square root of the sum of the squares of the X and Y momentum components, resulting in an average momentum of $10.7 \pm 0.2 \times 10^{-3} m_0c$. The fact these momentum features were present in both the ACAR and DB lineshape derivative plot implied these momenta are symmetric to all three axis of the momentum distribution, since they were present both p_{\parallel} and p_{\perp} . To quantify the difference between the ion irradiated, un-annealed SiC to the virgin, un-annealed in the momentum distribution parallel to the direction of the $e^{-}e^{+}$ pair's motion prior to annihilation in the 6H SiC, the ratio curve was calculated.

The ratio curve for the O^{+} ion irradiated, un-annealed 6H SiC relative to the virgin sample was calculated by normalizing the DB lineshape for the ion irradiated, un-annealed 6H SiC to the virgin sample and comparing it to the virgin 6H SiC normalized to itself. The ratio curve is shown in Figure 64. To compare the relative difference in the frequency of positron annihilations with valence and core electrons, momenta associated with valence-only, core and valence and core-only electrons, was required. Muller et al [96] calculated that the positron interactions with mostly valence electrons occurred at momenta smaller than $10 \times 10^{-3} m_0c$ and positron interactions with mostly valence electrons occurred at momenta larger than $20 \times 10^{-3} m_0c$. The region bounded by those momenta was associated with positrons annihilating with a mix of both valence and core electrons. All three regions were indicated by the shaded areas in the figure.

As shown in the ratio curve, more positrons interacted with lower momentum valence electrons than higher momentum electrons in the valence electron momentum range ion irradiated, un-annealed sample compared to the virgin 6H SiC. More

annihilations in the ion irradiated, un-annealed 6H SiC were also observed in the valence and core electron momentum region. Additionally, there were significantly less positron interactions with core electrons after the irradiation. These trends were compared below to the DB lineshape ratio for the ion irradiated, annealed 6H SiC to discriminate O atom effects from the vacancy defects.

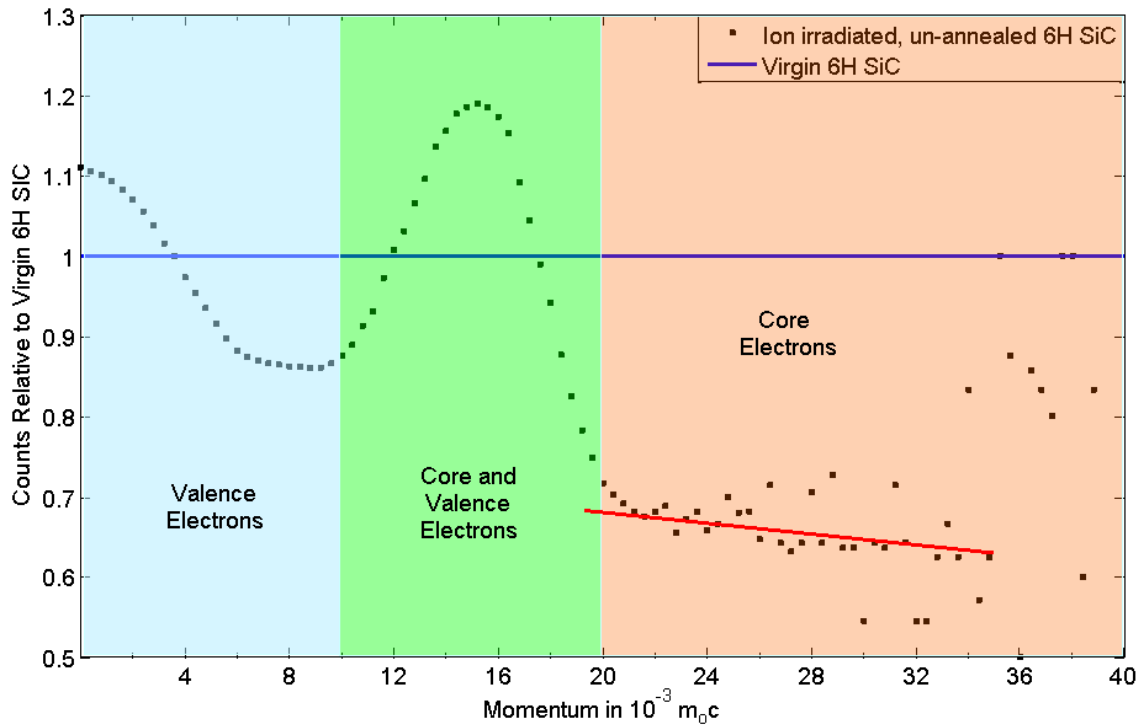


Figure 64. Ratio curve for ion irradiated, un-annealed 6H SiC (black squares) frequency of counts, relative to the virgin 6H SiC (blue line). Red line indicated least squares linear fit to statistically significant count distribution in core electron region.

5.11 3D Momentum Distribution for O⁺ Ion Irradiated, Un-annealed 6H SiC

Next, the 3D correlated momentum distribution from the 3DPAMM data set for O⁺ ion irradiated, un-annealed 6H SiC was analyzed. A square area, of the same size (in

momentum space) as the virgin sample, was extracted from the O^+ ion irradiated, un-annealed 3DPAMM 2D ACAR spectrum, without the efficiency correction. The momentum peaks centered at (7.5,7.5), (7.5,-7.5), (-7.5,-7.5), and (-7.5,8.0), specifically from the regions in (6.0:10.0,6.0:10.0), (6.0:10.0,-6.0:-10.0), (-6.0:-10.0,6.0:10.0), and (-6.0:-10.0,-6.0:-10.0) were extracted from the 3DPAMM data set which was not corrected for the DSSD charge collection strip efficiency. The four momentum peak areas contained a total of 1.89×10^5 counts, or 18.7% of the total counts recorded in the 3PDAMM data set. The resulting 3D momentum lineshape was constructed similarly as described above and is shown in Figure 65.

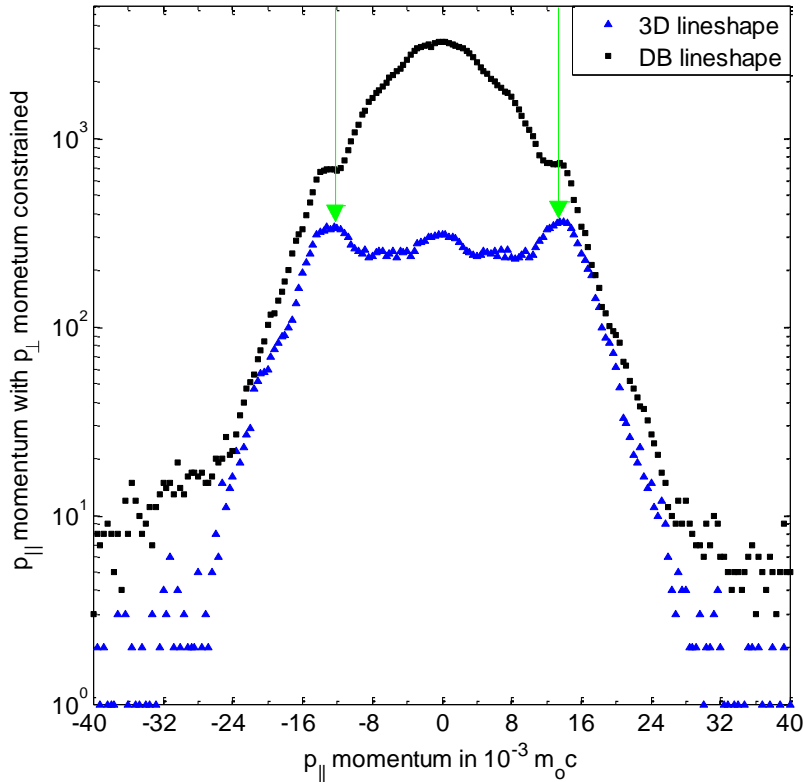


Figure 65. p_{\parallel} component for ion irradiated, un-annealed 6H SiC with p_{\perp} component constrained by peaks in the ACAR spectrum centered at (5:9,2:6), (5:9,-2:-6), (-5:-9,2:6), and (-5:-9,-2:-6). A $\Delta = 0.3$ keV was used to define the 3D momentum lineshape width of the p_{\parallel} component. Black squares indicated DB lineshape and blue triangles represented constrained, 3D momentum lineshape.

The two momentum peaks in the direction parallel to the e^-e^+ pair's motion prior to annihilation in the 3D lineshape above corresponded very well to the magnitude of the momentum of the two shoulder features at ± 3 keV observed in the corresponding DB lineshape. This not only indicated a momentum of $\pm 12 \times 10^{-3} m_0c$ existed primarily only in the component parallel to the direction parallel to the e^-e^+ pair's motion prior to annihilation, but it was correlated with the momentum in the plane perpendicular to the e^-e^+ pair's motion. Additionally, the magnitude of the momentum of the events in this region was calculated ($16.0 \pm 0.6 \times 10^{-3} m_0c$) since all three components were known. This correlation and the magnitude of the momentum would have never been unearthed if using separate ACAR and DBAR techniques to analyze the sample.

It was interesting to note that the wings in the 3D momentum lineshape for the ion irradiated, un-annealed SiC sample was in much closer proximity to the DB lineshape than for the virgin sample. This suggested the events which populated the four peaks in the ACAR spectra the 3D momentum was constrained to correlate with most of the high momentum events observed in the momentum component parallel to the e^-e^+ pair's motion prior to annihilation. The slight bump located at $-24 \times 10^{-3} m_0c$ did not correspond to any previously observed features and most likely was the result of the statistically low number of events in this region of the 3D momentum lineshape. The derivative of the 3D momentum lineshape was calculated and the plot was also constructed, but there were no significant features observed except for the ones mentioned above. Finally, the O^+ ion irradiated, annealed 6H SiC sample was examined.

5.12 O⁺ Ion Irradiated, Annealed 6H SiC 2D ACAR Response With DSSD

Efficiency Compensation

The O⁺ ion irradiated, annealed 6H SiC sample was analyzed using 3DPASS. The data compensated for the varying efficiency across the DSSD charge collection strips was collected and the 2D ACAR spectrum was reconstructed and is shown in Figure 66, following the procedure outlined in Sections 4.8 and 4.9. A total of 1.03×10^6 annihilation events were observed in the uncorrected data set. Compensating for the efficiency across the DSSDs' strips resulted in a scaled increase at the peaks centered at (9.0,10.0), (9.5,-9.5), (-9.5,-9.5), and (-9.5,10.0). The peaks scaled from 1041 to 2165, 1023 to 2178, 1052 to 2138, and 1036 to 2143, respectively for a 208 ± 4 % average scaling.

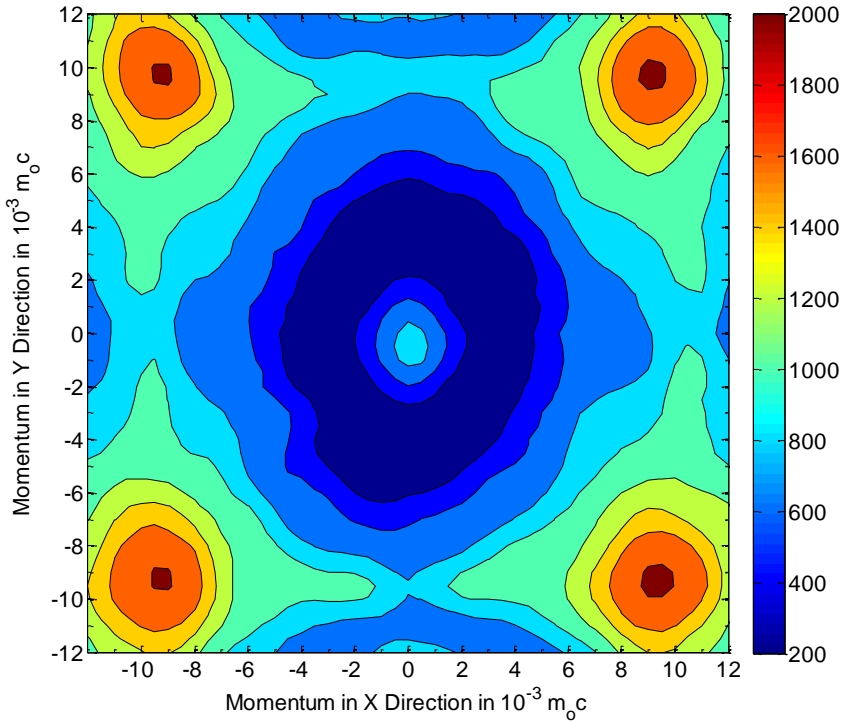
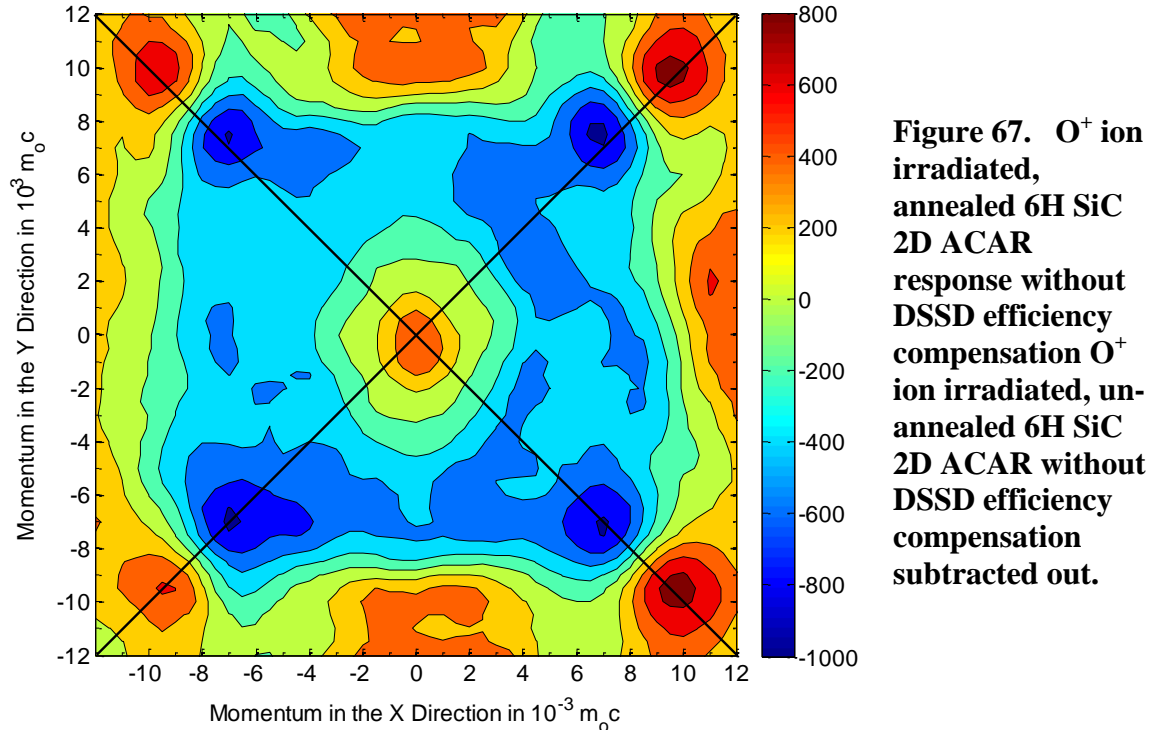


Figure 66. O⁺ ion irradiated, annealed 6H SiC 2D ACAR response with DSSD efficiency compensation, presented in momentum space.

The O^+ ion irradiated, un-annealed spectrum without efficiency compensation was subtracted from the ion irradiated, annealed spectrum without efficiency compensation to highlight any trends. The difference plot is displayed in Figure 67. Once again, many of the features present in the difference spectrum were present in either the O^+ ion implanted, un-annealed or the annealed spectra. The purpose of showing this plot was to highlight that as the vacancy-type defects were annealed out, confirmed by the PALS measurements, the magnitude of the momentum in the plane perpendicular to the e^-e^+ pairs' motion prior to annihilation increased from $2.8 \times 10^{-3} m_{oc}$ to $13.4 \times 10^{-3} m_{oc}$ along the same direction in that plane with annealing compared to the same momentum component in the un-annealed sample. If the direction of these momentum features in the experimental spectrum correlated with the bonding directions in the ion irradiated, annealed 6H SiC, which is supported by the correlation in the virgin sample results, then the location of the O atom relative to the Si-C bonding did not change from the un-annealed sample. Since the vacancy-type defects were annealed out, this implied the e^-e^+ momentum distribution associated with an interstitial O atom was more prevalent than the e^-e^+ momentum distribution of the O atom with surrounding vacancy-type defects or the O atom localized in a vacancy.



5.13 O^+ Ion Irradiated, Annealed 6H SiC 2D CDBAR Response

The CDBAR spectrum resulting from the 3DPAMM measurement on O^+ ion irradiated, annealed 6H SiC was populated from the same events used in the above ACAR analysis. The width orthogonal to the spectrum's DB lineshape's base was 6.6 keV versus the 6.2 keV width in the ion irradiated, un-annealed 6H SiC CDBAR spectrum. The DB lineshape was extracted from the ion implanted, annealed 6H SiC CDBAR spectra for coincident annihilation events. DB lineshapes were constructed with Δ , in Equation (36), varied from zero, following the same constraints listed in the earlier DB analyses. The FW(1/100)M decreased from 12.8 keV at $\Delta = 0$ keV to 12.1 keV at

$\Delta = 0.3$ keV. The FW(1/100)M then increased at $\Delta = 0.4$ keV to 12.2 keV. The DB lineshape corresponding to $\Delta = 0.3$ keV is shown in Figure 68.

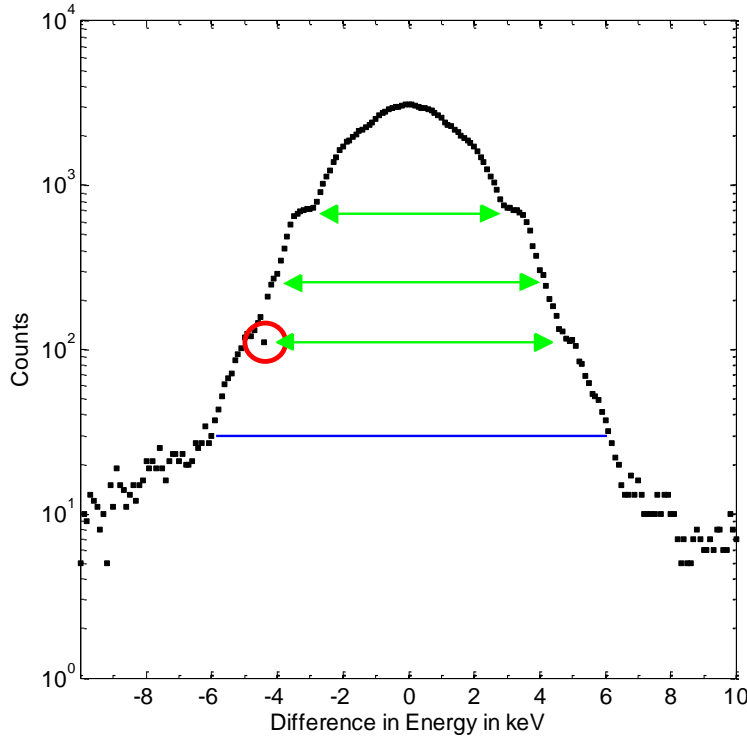


Figure 68. Single-crystal, O^+ ion irradiated, annealed 6H SiC DB lineshape for $\Delta = 3$ keV. (The blue line indicated the FW(1/100)M in the DB lineshape).

The difference of the slightly larger background contribution on the low-energy side relative to the background on the high-energy side, decreased as Δ increased from zero. The three symmetric shoulder features visible in the virgin 6H SiC DB lineshape at differences in energy of ± 3 keV, ± 4.1 keV and ± 4.4 keV were all not as visible in the ion irradiated, annealed DB lineshape, similar to the trend seen with the ion irradiated, un-annealed 6H SiC. The shoulder at ± 3 keV widened somewhat, whereas, the shoulders at ± 4.1 keV and ± 4.4 keV became almost unnoticeable. Additionally, a sharp decrease in events was observed, un-symmetrically around zero at a difference in energy

of -4.1 keV, corresponding to $16.6 \times 10^{-3} m_0 c$ in momentum space. The derivative of the DB lineshape was calculated to amplify these and other minor features.

The derivative of the DB lineshape with $\Delta = 0.3$ keV over one (blue) and two bins (red) was calculated and displayed in Figure 69. The three shoulder features present in the virgin 6H SiC DB lineshape at differences in energy of ± 3 keV, ± 4.1 keV and - 4.4 keV (+ 4.4 keV was absent) were observed in the ion implanted, annealed derivative plot, with derivatives of ~ 0 , ~ 900 and ~ 1000 counts/keV, respectively. The two larger momentum features had much larger derivatives than the surrounding derivative values when compared with the same features in the ion irradiated, un-annealed SiC DB lineshape. Additionally, the feature at $\Delta E = \pm 3$ keV was so wide and flat that the derivative approached zero, similarly to the un-annealed DB lineshape. Two features, also symmetric around zero, that presented as local maximums in the derivative plot were not visible in the DB lineshape, at differences in energy of ± 1.0 keV and ± 2.3 keV, corresponding to $4.0 \times 10^{-3} m_0 c$, and $9.2 \times 10^{-3} m_0 c$ in momentum space, respectively. These two features correlated with the two features observed in the ion implanted, un-annealed DB lineshape derivative plot and were also absent in the DB lineshape itself.

None of the features in the ion implanted, annealed 6H SiC's DB lineshape's derivative correlated to any feature in the ACAR spectrum. This suggested the features present in the DB lineshape and its derivative are uni-directional, corresponding to momentum in the component parallel to the e^-e^+ pair's motion prior to annihilation. To quantify the differences in the momentum distribution parallel to the direction of the e^-e^+ pair's motion prior to annihilation in the 6H SiC between the ion irradiated, annealed SiC

to the virgin, un-annealed and ion irradiated, un-annealed samples, the ratio curve was calculated.

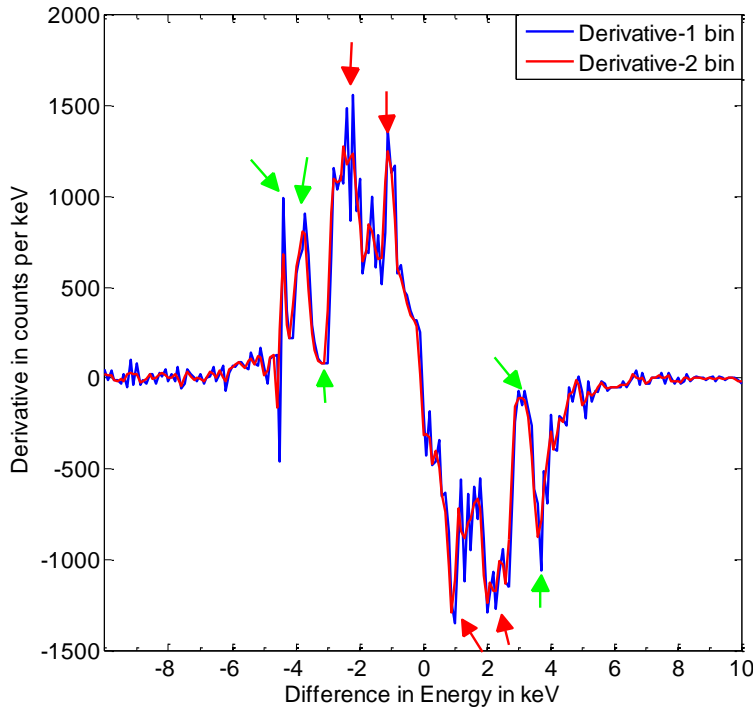


Figure 69. Derivative of DB lineshape with $\Delta = 0.3$ keV for O^+ ion irradiated, annealed 6H SiC. The blue line represented the derivative over a single bin (0.1 keV) and red represented the derivative over two bins (0.2 keV). Green arrows indicated features observed in green in the DB lineshape and red indicated significant changes in the lineshape's derivative without features present in the lineshape.

The ratio curve for the O^+ ion irradiated, annealed 6H SiC relative to the virgin sample was calculated by normalizing the DB lineshape for the ion irradiated, annealed 6H SiC to the virgin sample and comparing it to the virgin 6H SiC normalized to itself and the ion irradiated, un-annealed sample. The ratio curve is shown in Figure 70. As shown in the ratio curve, more positrons interacted with low momentum valence electrons than higher momentum electrons in the ion irradiated, annealed sample compared to the virgin 6H SiC but to a lesser degree than the ion irradiated, un-annealed sample. More annihilations in the ion irradiated, annealed 6H SiC were also observed in

the valence and core electron momentum region compared to the virgin 6H SiC, once again to a lesser degree than the ion irradiated, un-annealed sample. Additionally, there were more positron interactions with core electrons after with the ion irradiation and annealing compared to the un-annealed, but still less than the virgin 6H SiC sample. This implied more core electrons were readily available to interact with after the annealing, which indicated the O atoms that lodged into the vacancy-type defects due to the ion irradiation dislodged and most of the vacancies were filled with the Si and C interstitials. Not all vacancies were filled though because the ration in the core electron region was still below the virgin sample.

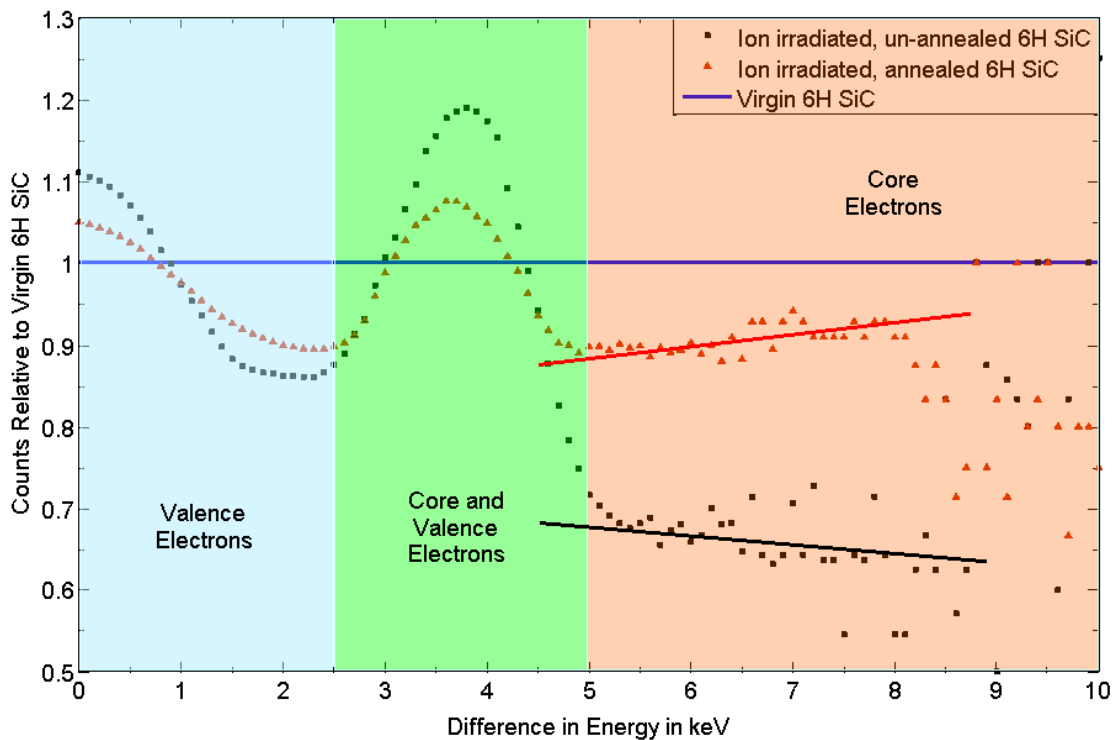


Figure 70. Ratio curve illustrating ion irradiated, un-annealed 6H SiC (black squares) and ion irradiated, annealed 6H SiC (red triangles) frequency of counts, relative to the virgin 6H SiC sample (blue line). Red and black lines indicated least squares fit of linear fit to count distribution in core electron region

5.14 3D Momentum Distribution for O^+ Ion Irradiated, Annealed 6H SiC

Next, the 3D momentum distribution from the 3DPAMM data set for virgin, annealed 6H SiC was analyzed. A square area, of the same size (in momentum space) as the virgin sample, was analyzed from the O^+ ion irradiated, annealed 3DPAMM 2D ACAR spectrum, without the efficiency corrected. Four momentum peak centered at (9.0,10.0), (9.5,-9.5), (-9.5,-9.5), and (-9.5,10.0), specifically from the regions in (7.0:11.0,8.0:12.0), (8.0:12.0,-8.0:-12.0), (-8.0:-12.0,8.0:12.0), and (-8.0:-12.0,-8.0:-12.0) were extracted from the 3DPAMM data set which was not corrected for the DSSD charge collection strip efficiency. The four momentum peak areas contained a total of 1.98×10^5 counts, or 19.2% of the total counts recorded in the 3PDAMM data set. The resulting 3D momentum lineshape is shown in Figure 71.

The two momentum peaks in the 3D momentum lineshape in the direction parallel to the e^-e^+ pair's motion prior to annihilation corresponded favorably to the magnitude of the momentum of the two shoulder features at ± 2.6 keV observed in the DB lineshape derivative plot. This indicated a momentum of $\pm 13.4 \times 10^{-3} m_0c$ represented by the momentum features in the ACAR spectrum centered at (9.0,10.0), (9.5,-9.5),(-9.5,-9.5), and (-9.5, 10.0) correlated with the $\pm 10.4 \times 10^{-3} m_0c$ momentum component parallel to the direction parallel to the e^-e^+ pair's motion prior to annihilation. Additionally, since all three components were known, the magnitude of the momentum of the events in this region was calculated as $17.0 \pm 0.9 \times 10^{-3} m_0c$. The magnitude of momentum for the anisotropies in the annealed and un-annealed sample ($16.0 \pm 0.6 \times 10^{-3} m_0c$) were statistically equal, which was expected from the conservation of momentum.

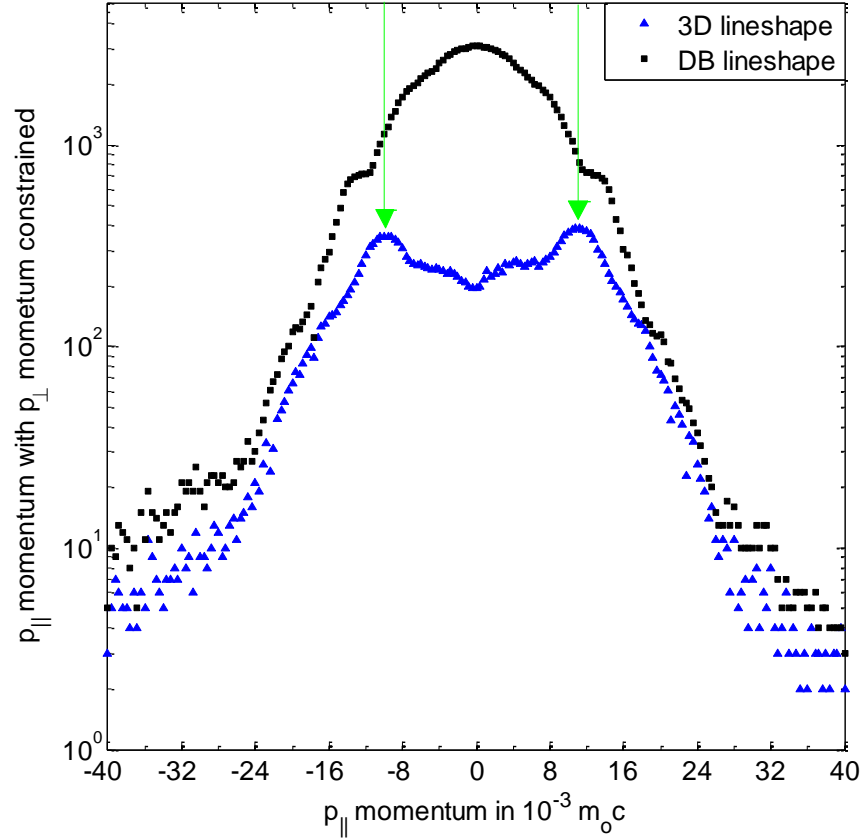


Figure 71. p_{\parallel} component for ion irradiated, annealed 6H SiC with p_{\perp} component constrained by the momentum peaks in the ACAR spectrum centered at (9.0,10.0), (9.5,-9.5), (-9.5,-9.5), and (-9.5, 10.0). A $\Delta = 0.3$ keV was used to define the 3D momentum lineshape width of the p_{\parallel} component. Black squares indicated unconstrained DB lineshape and blue triangles represented constrained, 3D momentum lineshape.

Note the wings in the 3D momentum lineshape for the ion irradiated, annealed SiC sample, like the un-annealed sample's 3D lineshape, was in much closer proximity to the DB lineshape when compared to the virgin sample. Additionally, as a result of the annealing, a majority of the high momentum events located in the features in the plane perpendicular to the $e^{-}e^{+}$ pair's motion had a higher momentum component in this plane, but a smaller component in the parallel momentum component, compared to the ion irradiated, un-annealed sample indicated by the small dip in the center of the 3D

momentum lineshape around 0 momentum. Since more O atoms were dislodged from the vacancy-type defects and settled out as interstitials in the SiC lattice, the hybridization of the S-C bonds increased. The increased hybridization of the SiC bonds resulted in a lower s - p orbital ratio. Therefore, fewer low momentum electrons, typically associated with s -orbitals were observed than the high momentum electrons in the p -orbitals. These correlations would have never been unearthed if using separate ACAR and DBAR techniques to analyze the sample.

6 Conclusions and Future Work

This research accomplished several goals which are new to the PAS community. First, the first-ever positron spectrometer (3DPASS) capable of simultaneously measuring all three axial components of the e^-e^+ pair's momentum prior to annihilation was constructed and its performance validated using single-crystal Cu and virgin 6H SiC PAS results from previous research. Additionally, incorporation of several novel engineering techniques, such as utilizing two HPGe DSSDs, including transient charge analysis to exploit subpixel interpolation, and integrating fast, programmable, digital electronics capable of real-time calculations of the transient charges' FOM, permitted significant reduction in the footprint of the spectrometer, compared to other state-of-the-art PAS systems. Finally, a model to quantify the subpixel resolution of the DSSDs used in 3DPASS from experimental data which has not been documented in the literature was developed and executed. While these are advances in the technique, the data itself is ground-breaking. This section will detail the conclusions the 3DPASS data revealed for all three 6H SiC samples measured using 3DPASS.

In the virgin un-irradiated 6H SiC, it is clear that the direction of the momentum of the e^-e^+ pair prior to their annihilation lines up favorably with the bonding directions in the 6H SiC by superimposing the rotated unit cell onto the ACAR spectrum for the virgin SiC. Additionally, the 2D ACAR and CDBAR spectra obtained using 3DPASS correlated well with previously published results. Next, it is clearly evident by the considerable change in the ACAR momentum anisotropies that the 6H SiC's lattice structure was significantly perturbed by the ion implantation due to either the O atom thermalizing and stopping between the lattice structure as an interstitial, the vast amount

of vacancy-type defects produced by the thermalization of the O ion, or the O atoms localized within the vacancies produced during their thermalization, or any combination of three processes. Additionally, the manner in which the anisotropies change suggest a slight realignment of the Si-C dipole in the direction of the bonds from either the O atom itself or the vacancy-type defects resulting from the O atom thermalization. This ultimately caused a smaller influence in one direction of the momentum distribution. Finally the results from the ratio curve for the O^+ ion irradiated, annealed 6H SiC sample indicated that the O atoms that lodged into the vacancy-type defects from the ion irradiation dislodged and most of the vacancies were filled with the Si and C interstitials. These findings were deduced by examining the ACAR and DBAR analysis independently. By correlating the momentum components, which were inherent due to the interpolation method's criteria, and analyzing the correlated ACAR/DBAR response, even more conclusions have been drawn.

The 3D momentum lineshape, which has never been reported in the literature, examined the correlated momentum components by constraining the momentum in the plane perpendicular to the e^-e^+ pair's motion prior to annihilation (the ACAR features) and populating the 3D momentum lineshape by investigating the energy difference of the coincident events subjected to the constraint, which represented the parallel momentum component. First, two momentum peaks in the 3D momentum lineshape for the virgin 6H SiC correspond very well to the magnitude of the momenta of the four features that the perpendicular momentum component was constrained to which indicated a momentum of $\pm 8.1 \times 10^{-3} m_0 c$ existed in both momentum components in the sample. Next, for the ion irradiated, un-annealed sample, the 3D momentum lineshape results

indicated a momentum of $\pm 12 \times 10^{-3} m_0 c$ existed primarily only in the component parallel to the direction parallel to the e^-e^+ pair's motion prior to annihilation, which correlated with the anisotropies observed in the plane perpendicular to the e^-e^+ pair's motion. Next, for the ion irradiated, annealed 6H SiC sample, the momentum of $\pm 10.4 \times 10^{-3} m_0 c$, observed in the 3D momentum lineshape correlated to the $\pm 13.4 \times 10^{-3} m_0 c$ momentum features in the ACAR spectrum. Finally, the magnitude of momentum of the anisotropies in the annealed and un-annealed samples, $17.0 \pm 0.9 \times 10^{-3} m_0 c$ and $16.0 \pm 0.6 \times 10^{-3} m_0 c$, respectively, were calculated and were statistically equivalent, which was expected from the conservation of momentum. These correlations would have never been found using separate ACAR and DBAR techniques to analyze the samples.

The 3DPAMM technique when used with the 3DPASS is promising for simultaneously extracting all three dimensions of e^-e^+ pair's momentum prior to annihilation in a single measurement. Several areas of research, both theoretical and experimental in nature, should be conducted in order to fully explore the techniques limits and potential applications to other types of materials.

A quantum mechanical code should be developed which approximates the electronic wavefunction of the 6H SiC lattice, the O atom and the vacancy-type defects produced from the thermalization of the O^+ ions, and the positronic wavefunction. Then the e^-e^+ pair's momentum distribution in both the direction parallel and the plane perpendicular to the e^-e^+ pair's momentum prior to annihilation can be approximated. These calculations can be compared to the 2D ACAR and CDBAR results of the samples measured using 3DPASS.

3DPASS suffered from the low activity of the source and the size of the sample used. To increase the system's capabilities, a positron beam with a small spot size, on the order of 1 mm, would increase the number of positrons injected into the sample. The narrow beam, however, would not degrade the system's angular resolution. Additionally, the beam would allow for any desired orientation of the sample relative to the face of each DSSD.

Replacement of the Ortec DSSD with another DSSD similar to the PHDS would increase efficiency and the range of the momentum measurement (or decrease the angular resolution if desired) in the plane perpendicular to the e^-e^+ pair's motion prior to annihilation. Another improvement to examine is to include coaxial Ge detectors behind the PHDS DSSDs and look at Compton events scattered out of the PHDS into the coaxial. Including these events would undoubtedly increase the overall efficiency of the system, but to what extent should be modeled using GEANT4 and experimentally reinforced.

Completion of the theoretical work suggested above will validate that the 3DPAMM technique using the 3DPASS provides collection of ACAR and DBAR momentum distributions comparable to state-of-the-art PAS spectrometers detailed in the literature and correlated 3D momentum distributions which have never been measured before. Additionally, the experimental research suggested above will increase the system's efficiency, allowing either a reduction in the measurement time or acquiring more correlated momentum events.

Appendix A Spec32 Settings and Operation

The Spec32 settings were initially set using PHDS' recommendations and optimized by collecting numerous spectra to attain the sharpest resolution without significantly sacrificing efficiency. The following table lists the final equipment settings for the Spec32, as programmed into the Imager32 software collect spectra. A short description of the settings follows.

Table 7. Final Spec32 settings for experiment.

Slow-channel Pulse Shaping					Fast-channel Pulse Shaping				
	Daughter Board Num					Daughter Board Num			
	0	1	2	3		0	1	2	3
Gap (20 ns)	50	50	50	50	Gap (in 20 ns)	0	0	0	0
Peaking Time (20 ns)	200	200	200	200	Peaking Time (20 ns)	11	11	11	11
Shift By	2	1	2	1	Shift By	0	0	0	0
P/Z Correction	30	30	30	30					
Input Signal Polarity					Trigger Mode				
	Daughter Board Num					Daughter Board Num			
	0	1	2	3		0	1	2	3
Lower 4 Channels	Pos	Pos	Neg	Pos	Pulse Threshold	280	220	247	220
Higher 4 Channels	Pos	Pos	Neg	Pos	Slow Threshold	0	0	0	0
Detector Configuration									
Minimum DC Channel				0	Maximum DC Channel				15
Minimum AC Channel				16	Maximum DC Channel				31

Some user-defiend settings can be set for the entire Spec32 system while others for specific sub-sets inthe Spec32. The daughter board represents a board with two FPGA's. The lower 4 channels represents one FPGA and the higher 4 channels represents the other. The slow- and fast-channel pulse shaping, and trigger modes can only be set for each daughter board, but the input signal polarity can be set for each individual FPGA. The Gap and Peaking Time are the settings for the trapezoidal filter for the flat-top and rise-time discriminators, respectively. Shift By, acts analagously to

the gain on NIM electronics by linearly stretching the the spectra over the 32K channels in the spectra as the Shift By number decreases. P/Z Correction is the setting to compensate for the preamplifier decay constant and returns the pulse to baseline without undershooting the baseline between pulses. Pulse Threshold ignores pulses below a certain level. The value of the pulse threshold is not a direct representative of energy, rather it is proportional to pulse height in ADC units. The Input Signal Polarity is the polarity indicator for the pulses present in the channels connected for each FPGA in the Spec32. Each FPGA is limited to a single input polarity. The minimum and maximum AC and DC channels are the settings to indicate which channels are the front and rear of the DSSDs to allow the Imager software to automatically interpolate. This feature can only be used for a single DSSD with two sides. The system is limited to 16 AC and 16 DC channels for a single DSSD. Although this feature was not used for this application due to utilizing two DSSDs, the setting were selected for the sake of completeness.

Several type of spectra can be viewed in Spec32. The "Eng Spec" option displays individual strip spectra and the pulldown menu allows selection of the strip to view. The "Show all" check box allows a display of all channels at once. This feature is nice because it lines up all spectra at the same energy for easy comparison between strips. The "Ave Spec" option displays a spectrum built up from averaged energies for events that were detected coincidently on both an AC side and a DC side strip. It shows for each AC/DC pixel (intersection of an AC and DC strip) the averaged energy of events detected within that pixel. The pulldown menu allows for selection of an individual pixel ("Pixel AC DC") or the total of all pixels ("Pixel Total"). The last selection, "All Events" was added to accomodate high energy sources where most of the interactions are Compton

scattered events and all of the gamma ray energy is not contained in any single pixel.

This option shows the average of the total AC-side and DC-side energies, summed over all strips.[77]

Appendix B Lifetime Spectra and PALSfit Results

The lifetime spectra for the virgin single-crystal Cu, virgin, single-crystal 6H SiC, the un-annealed O^+ ion irradiated 6H SiC sample with the positrons injected on the opposite side of the 6H SiC sample as the ions and that sample subsequently annealed are presented below. Next, PALSfit was executed for each of the lifetime spectra mentioned above and the lifetimes and their associated intensities were calculated.

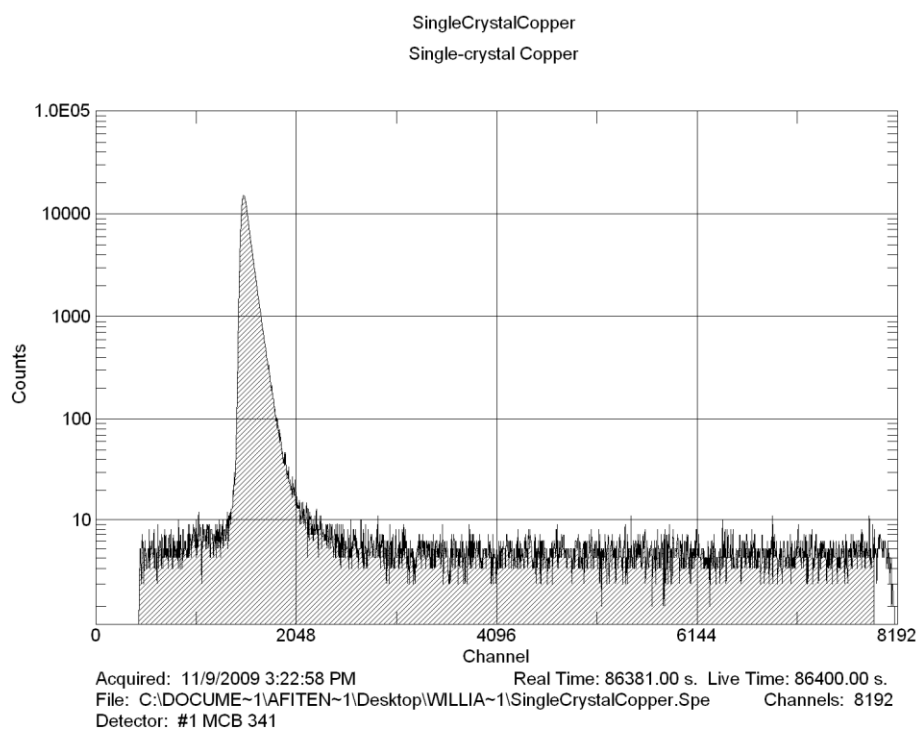


Figure 72. Lifetime spectrum for virgin, single-crystal Cu.

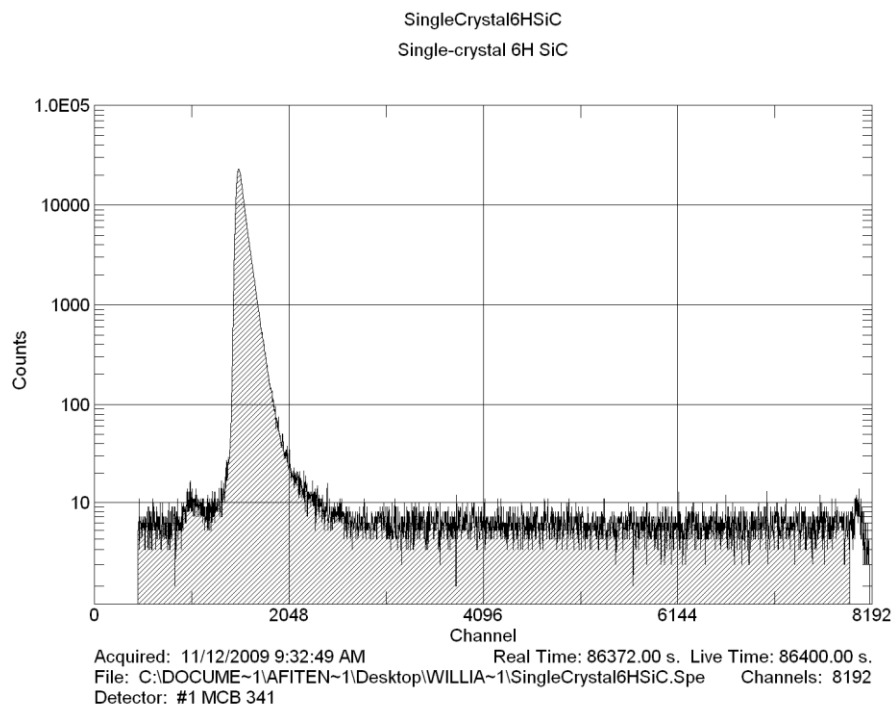


Figure 73. Lifetime spectrum for virgin, single-crystal 6H SiC.

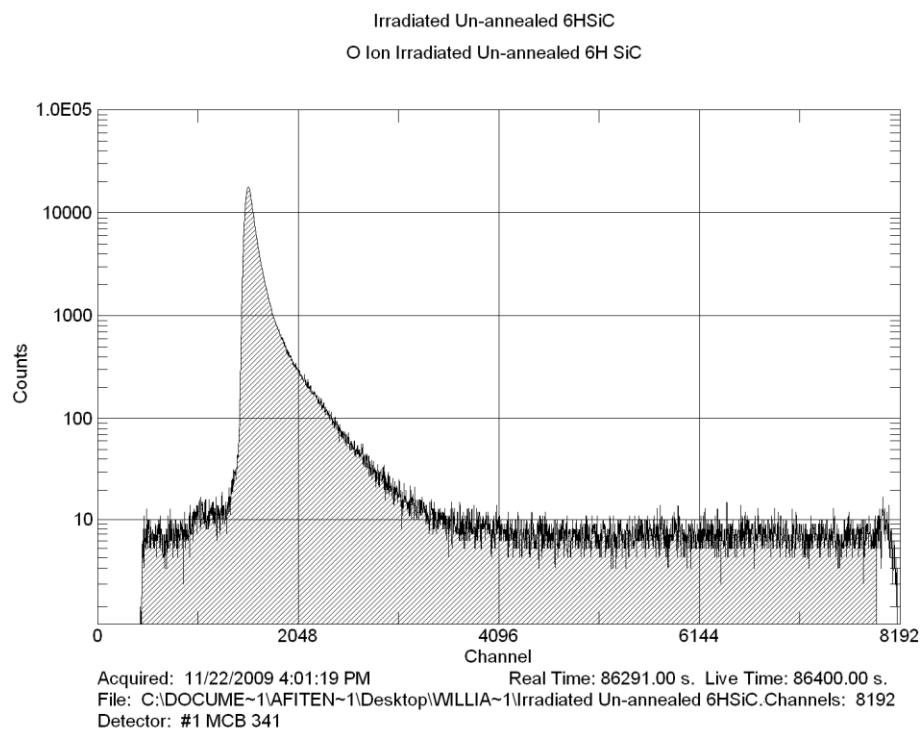


Figure 74. Lifetime spectrum for O^+ ion irradiated, un-annealed single-crystal 6H SiC.

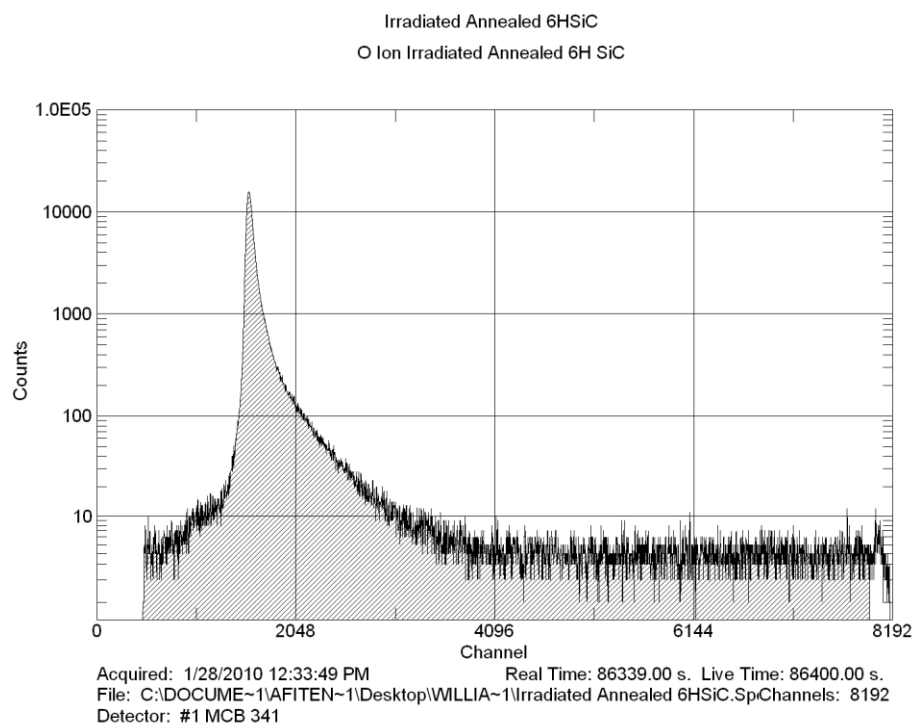


Figure 75. Lifetime spectrum for O⁺ ion irradiated, annealed single-crystal 6H SiC.

Unconstrained single-crystal virgin Cu PALSfit output file

PositronFit output file: C:\Documents and Settings\AFIT
ENP\Des...\SingleCrystalCopper_1.out

ITERATION CYCLE NO 1 COMPLETED

ITERATION CYCLE NO 2 COMPLETED

P O S I T R O N F I T . VERSION AUG. 06 . JOB TIME 19:55:28.35 24-NOV-09

SingleCrystalCopper_1

L T I B Z A G
3 0 0 0 0 0 3

TIME SCALE NS/CHANNEL : 0.006200
AREA RANGE STARTS IN CH. 444 AND ENDS IN CH. 8192
FIT RANGE STARTS IN CH. 1445 AND ENDS IN CH. 2200

RESOLUTION FWHM (NS) : 0.2021 0.3236 1.1352
FUNCTION INTENSITIES (%) : 83.0000 11.0000 6.0000
SHIFTS (NS) : 0.0000 -0.0651 0.1593

INITIAL TIME-ZERO (CH.NO): 1490.0000G
PARAMETERS LIFETIMES (NS) : 0.1200 0.4000G 1.8500G

----- N O S O U R C E C O R R E C T I O N -----

F I N A L R E S U L T S

L T I B Z A G
3 0 0 0 0 0 3

CONVERGENCE OBTAINED AFTER 19 ITERATIONS
VARIANCE OF THE FIT = 1.009 WITH STANDARD DEVIATION 0.056
CHI-SQUARE = 654.84 WITH 649 DEGREES OF FREEDOM
SIGNIFICANCE OF IMPERFECT MODEL = 64.03 %

LIFETIMES (NS) : 0.1154 0.4916 0.6098
STD DEVIATIONS : 0.0021 0.0061 0.0110

INTENSITIES (%) : 59.0073 36.1228 4.8699
STD DEVIATIONS : 0.3518 0.6483 0.9830

BACKGROUND COUNTS/CHANNEL : 6.4407
STD DEVIATIONS : 0.2683

TIME-ZERO CHANNEL NUMBER : 1498.1052
STD DEVIATIONS : 0.0826

TOTAL-AREA FROM FIT : 1.12396E+06 FROM TABLE : 1.15370E+06

P O S I T R O N F I T

Time for this job: 0.13 seconds.

Constrained single-crystal virgin Cu PALSfit output file

PositronFit output file: C:\Documents and Settings\AFIT
ENP\Des...\SingleCrystalCopper_29.out

ITERATION CYCLE NO 1 COMPLETED

ITERATION CYCLE NO 2 COMPLETED

P O S I T R O N F I T . VERSION AUG. 06 . JOB TIME 12:09:18.05 25-NOV-09

SingleCrystalCopper_29

L T I B Z A G
3 1 0 0 0 0 3

TIME SCALE NS/CHANNEL : 0.006200
AREA RANGE STARTS IN CH. 444 AND ENDS IN CH. 8192
FIT RANGE STARTS IN CH. 1445 AND ENDS IN CH. 2200

RESOLUTION FWHM (NS) : 0.2021 0.3236 1.1352
FUNCTION INTENSITIES (%) : 83.0000 11.0000 6.0000
SHIFTS (NS) : 0.0000 -0.0651 0.1593

INITIAL TIME-ZERO (CH.NO): 1490.0000G
PARAMETERS LIFETIMES (NS) : 0.1200F 0.4000G 1.8500G

----- N O S O U R C E C O R R E C T I O N -----

F I N A L R E S U L T S

L T I B Z A G
3 1 0 0 0 0 3

CONVERGENCE OBTAINED AFTER 17 ITERATIONS
VARIANCE OF THE FIT = 1.016 WITH STANDARD DEVIATION 0.056
CHI-SQUARE = 658.28 WITH 648 DEGREES OF FREEDOM
SIGNIFICANCE OF IMPERFECT MODEL = 61.89 %

LIFETIMES (NS) : 0.1200 0.4202 0.6135
STD DEVIATIONS : 0.0000 0.0052 0.0128

INTENSITIES (%) : 57.4567 34.3301 8.2132
STD DEVIATIONS : 0.4804 0.9327 1.1137

BACKGROUND COUNTS/CHANNEL : 6.4407
STD DEVIATIONS : 0.2683

TIME-ZERO CHANNEL NUMBER : 1498.1052
STD DEVIATIONS : 0.0826

TOTAL-AREA FROM FIT : 1.12396E+06 FROM TABLE : 1.15370E+06

P O S I T R O N F I T

Time for this job: 0.12 seconds.

Single-crystal virgin 6H SiC PALSfit output file

PositronFit output file: C:\Documents and Settings\AFIT
ENP\Des...\SingleCrystal6HSiC_34.out

ITERATION CYCLE NO 1 COMPLETED

P O S I T R O N F I T . VERSION AUG. 06 . JOB TIME 10:28:41.07 26-NOV-09

SingleCrystal6HSiC

L T I B Z A G
3 1 0 0 0 0 3

TIME SCALE NS/CHANNEL : 0.006200
AREA RANGE STARTS IN CH. 457 AND ENDS IN CH. 8192
FIT RANGE STARTS IN CH. 1453 AND ENDS IN CH. 2200

RESOLUTION FWHM (NS) : 0.2046 0.3244 1.1371
FUNCTION INTENSITIES (%) : 83.0000 11.0000 6.0000
SHIFTS (NS) : 0.0000 0.1151 -0.8926

INITIAL TIME-ZERO (CH.NO): 1490.0000G
PARAMETERS LIFETIMES (NS) : 0.4200F 0.2000G 1.8500G

----- N O S O U R C E C O R R E C T I O N -----

F I N A L R E S U L T S

L T I B Z A G
3 1 0 0 0 0 3

CONVERGENCE OBTAINED AFTER 9 ITERATIONS
VARIANCE OF THE FIT = 1.017 WITH STANDARD DEVIATION 0.052
CHI-SQUARE = 752.52 WITH 740 DEGREES OF FREEDOM
SIGNIFICANCE OF IMPERFECT MODEL = 63.34 %

LIFETIMES (NS) : 0.1387 0.4200 1.5116
STD DEVIATIONS : 0.0068 0.0000 1.7743

INTENSITIES (%) : 73.2231 26.3359 0.4410
STD DEVIATIONS : 0.4114 1.6031 0.3981

BACKGROUND COUNTS/CHANNEL : 5.8288
STD DEVIATIONS : 0.1969

TIME-ZERO CHANNEL NUMBER : 1496.9219
STD DEVIATIONS : 0.0717

TOTAL-AREA FROM FIT : 1.20357E+06 FROM TABLE : 1.30168E+06

P O S I T R O N F I T

Time for this job: 0.05 seconds.

Single-crystal O⁺ Ion Irradiated Un-annealed 6H SiC PALSfit output file

PositronFit output file: C:\Documents and Settings\AFIT
EN...\SinglecrystalOIrradiatedUnannealed6HSiC_21.out

ITERATION CYCLE NO 1 COMPLETED

P O S I T R O N F I T . VERSION AUG. 06 . JOB TIME 11:11:30.31 29-Jan-10

SinglecrystalOIrradiatedUnannealed6HSiC_21

L	T	I	B	Z	A	G
4	3	0	0	0	0	3

TIME SCALE	NS/CHANNEL	:	0.006200			
AREA RANGE	STARTS IN CH.	456	AND ENDS IN CH.	8192		
FIT RANGE	STARTS IN CH.	1453	AND ENDS IN CH.	2200		

RESOLUTION	FWHM (NS)	:	0.2032	0.3265	1.1364	
FUNCTION	INTENSITIES (%)	:	83.0000	11.0000	6.0000	
	SHIFTS (NS)	:	0.0000	-0.0293	-0.2077	

INITIAL	TIME-ZERO (CH.NO):	1490.0000G				
PARAMETERS	LIFETIMES (NS)	:	0.1390F	0.2860F	0.4200F	

1.8500G

----- N O S O U R C E C O R R E C T I O N -----

F I N A L R E S U L T S

L	T	I	B	Z	A	G
4	3	0	0	0	0	3

CONVERGENCE OBTAINED AFTER 13 ITERATIONS
VARIANCE OF THE FIT = 1.017 WITH STANDARD DEVIATION 0.039
CHI-SQUARE = 1373.61 WITH 1350 DEGREES OF FREEDOM
SIGNIFICANCE OF IMPERFECT MODEL = 60.22 %

LIFETIMES (NS)	:	0.1390	0.2860	0.4200	0.2050
STD DEVIATIONS	:	0.0000	0.0000	0.0000	0.0084

INTENSITIES (%)	:	42.8628	24.2173	13.9199	19.0001
STD DEVIATIONS	:	1.4962	1.2191	0.3701	1.7329

BACKGROUND	COUNTS/CHANNEL	:	8.2901		
	STD DEVIATIONS	:	0.5906		

TIME-ZERO	CHANNEL NUMBER	:	1544.8354		
	STD DEVIATIONS	:	0.6967		

TOTAL-AREA	FROM FIT	:	1.00019E+06	FROM TABLE	: 1.01528E+06
------------	----------	---	-------------	------------	---------------

P O S I T R O N F I T

Time for this job: 0.11 seconds.

Single-crystal O⁺ Ion Irradiated Annealed 6H SiC PALSfit output file

PositronFit output file: C:\Documents and Settings\AFIT
ENP\Des...\IrradiatedAnnealed6HSiC_59.out

ITERATION CYCLE NO 1 COMPLETED

P O S I T R O N F I T . VERSION AUG. 06 . JOB TIME 23:05:19.11 28-JAN-10

IrradiatedAnnealed6HSiC_59

L T I B Z A G
3 2 0 0 0 0 3

TIME SCALE NS/CHANNEL : 0.006200
AREA RANGE STARTS IN CH. 457 AND ENDS IN CH. 8192
FIT RANGE STARTS IN CH. 1453 AND ENDS IN CH. 2200

RESOLUTION FWHM (NS) : 0.2068 0.3283 1.1402
FUNCTION INTENSITIES (%) : 83.0000 11.0000 6.0000
SHIFTS (NS) : 0.0000 -0.0875 -0.5341

INITIAL TIME-ZERO (CH.NO): 1490.0000G
PARAMETERS LIFETIMES (NS) : 0.1390F 0.4200F 1.8500G

----- N O S O U R C E C O R R E C T I O N -----

F I N A L R E S U L T S

L T I B Z A G
3 2 0 0 0 0 3

CONVERGENCE OBTAINED AFTER 8 ITERATIONS
VARIANCE OF THE FIT = 0.998 WITH STANDARD DEVIATION 0.034
CHI-SQUARE = 1855.30 WITH 1859 DEGREES OF FREEDOM
SIGNIFICANCE OF IMPERFECT MODEL = 54.59 %

LIFETIMES (NS) : 0.1390 0.4200 0.2864
STD DEVIATIONS : 0.0000 0.0000 0.0044

INTENSITIES (%) : 61.1951 15.7007 23.1042
STD DEVIATIONS : 1.7618 1.6326 0.7817

BACKGROUND COUNTS/CHANNEL : 6.2266
STD DEVIATIONS : 0.7391

TIME-ZERO CHANNEL NUMBER : 1504.3739
STD DEVIATIONS : 0.4070

TOTAL-AREA FROM FIT : 1.32522E+06 FROM TABLE : 1.32827E+06

P O S I T R O N F I T

Time for this job: 0.08 seconds.

Bibliography

1. Harris G. (1995) *Properties of Silicon Carbide*. Short Run Press Ltd. United Kingdom.
2. Morkoc H., Strite S., Gao G. B., Lin M. E., Sverdlov B., and Burns M. (1994) "Large-Band-Gap SiC, III-V Nitride, and II-VI ZnSe-based Semiconductor Device Technologies", *Journal of Applied Physics*, Vol. 76, Iss. 3, pp. 1363-98.
3. Dirac P.A.M. (1928) "The Quantum Theory of the Electron", *Proceedings of the Royal Society of London. Series A, Containing Papers of a Mathematical and Physical Character*, Vol. 117, Iss. 778, pp. 610-24
4. Anderson Carl D. (1933) "The Positive Electron", *Physical Review*, Vol. 43, pp. 491-4.
5. Morgana G, Alricka K, Saundersa A, Cvernaa F, Kinga N, Merrilla F, Watersa L, Hanson A, Greene G, Liljestrand R, Thompson R, and Henry E. (2003) "Total Cross Sections for the Production of ^{22}Na and ^{24}Na in Proton-induced Reactions on ^{27}Al from 0.40 to 22.4 GeV", *Nuclear Instruments and Methods in Physics Research Section B: Beam Interactions with Materials and Atoms*, Vol. 211, Iss. 3, pp. 297-304.
6. Knoll Glenn F. *Radiation Detection and Measurement- 3rd Edition*, John Wiley and Sons Inc, New York, 2000.
7. Turner James E. *Atoms, Radiation, and Radiation Protection-2nd Edition*, John Wiley and Sons Inc, New York, 1995.
8. Bauer-Kugelmann W., Koegel G., Sperr P., and Triftauser W. (1997) "Positron Lifetimes and Positron Moderation of 4H-SiC Subjected to various Treatments", *Materials Science Forum*, Vols. 255-7, pp. 662-4.
9. Stormer J, Goodyear A, Anwand W, Brauer G, Coleman P, and Triftshauer W. (1996) "Silicon Carbide: A New Positron Moderator", *Journal of Physics Condensed Matter*, Vol. 8, pp L89-L94.
10. Adamson P. E. (2005) *Quantum Mechanical Prediction of Experimental Observables of Positron-Vacancy Complexes in Silicon Carbide*. Dissertation. The Air Force Institute of Technology.
11. Jean Y. C., Mallon P. E. and Schrader D. M. *Principles and Applications of Positron and Positronium Chemistry*. World Scientific, New Jersey, 2003.

12. Ore A. and Powell J. L. (1949) "Three-Photon Annihilation of an Electron-Positron Pair," *Physical Review*, Vol. 75, Num. 11, pp. 1696-99.
13. Ross, M. (2008) *Development and Optimization of a Positron Annihilation Lifetime Spectrometer to Measure Nanoscale Defects in Solids and Borane Cage Molecules in Aqueous Nitrate Solutions*. Thesis. The Air Force Institute of Technology.
14. DuMond, J. M. W., Lind D. A., and Watson B. B. (1949) "Precision Measurement of the Wavelength and Spectral Profile of the Annihilation Radiation from ^{64}Cu with the Two-meter Focusing Curved Crystal Spectrometer", *Physical Review*, Vol. 75, Num. 8, pp. 1226-39.
15. Ho K., Beling F., Cheng V., Ng M, and Yip A. (2003) "Deconvolution of Positron Annihilation Coincidence Doppler Broadening Spectra Using an Iterative Projected Newton Method with Non-negativity Constraints", *Review of Scientific Instruments*, Vol. 74, Num. 11, pp. 4779-87.
16. Charlton M and Humbertson J. W. *Positron Physics*, Cambridge University Press, Cambridge, 2001.
17. Hunt A.W., Cassidy D. B., Sterne P.A., Cowan T. E., Howell R. H., Lynn K. G., and Golovchenko J. A. (2001) "Doppler Broadening of In-Flight Positron Annihilation Radiation Due to Electron Momentum", *Physical Review Letters*, Vol. 86, Num. 24, pp. 5612-5.
18. Nascimento E, Helenea O, Takiyab C, and Vanin V. (2005) "Doppler Broadening of Positron Annihilation Radiation: Fitting the Coincidence Spectrum", *Nuclear Instruments and Methods in Physics Research A*. Vol. 538, pp. 723–30.
19. Lynn, K.G and Goland, A.N. (1976) "Observation of High Momentum Tails of Positron-annihilation Lineshapes", *Solid State Communications*, Vol. ,18 Iss. 11-12, pp. 1549-52.
20. Haaks M., Staab T. E. M., and Maier K. (2006) "Analyzing the High-momentum Part of Positron Annihilation Doppler Spectra with a Single Germanium Detector", *Nuclear Instruments and Methods in Physics Research A*, Vol. 569, pp. 829–36.
21. Nagai Y., Tangb Z., and Hasegawa M. (2000) "Chemical Analysis of Precipitates in Metallic Alloys Using Coincidence Doppler Broadening of Positron Annihilation Radiation", *Radiation Physics and Chemistry*, Vol. 58, Iss. 5-6, pp. 737-42.
22. Baranowskia A., Beliczynskia J., Kostrzewab M., and Szuszkiewicz M. (2004) "A Two-detector Spectrometer for Measurements of Doppler Broadened Positron Annihilation Spectra", *Nuclear Instruments and Methods in Physics Research A*, Vol. 526, pp. 420–31.

23. Dekker J, Saarinen K, Olafsson H, and Sveinbjornsson E. (2003) "Observation of Interface Defects in Thermally Oxidized SiC Using Positron Annihilation", *Applied Physics Letters*, Vol. 82, Num. 13, pgs 2020-2023.
24. Karwasz G ; Rurali R; Consolati G; and Godignon P. (2004) "Defect Dynamics in P+ Implanted 6H-SiC Studied by Positron Annihilation Spectroscopy", *Physica Status Solidi C*, Vol. 1, Num. 2, pp. 257-60.
25. Maekawa M, Kawasuso A, Yoshikawa M, Miyashita A, Suzuki R, and Ohdaira T. (2006) "Structure of SiO₂/4H-SiC Interface Probed by Positron Annihilation Spectroscopy", *Physical Review B*, Vol. 73, Iss. 1.
26. Saint Gobain Crystals. (Dec 2007) *Scintillation Products Technical Note: BrillianceTM Scintillators Performance Summary*.
27. Canberra. (2003) *Germanium Detectors*.
28. Krause-Rehberg R and Leipner H. *Positron Annihilation in Semiconductors*. Springer Verlag, Berlin, 1998.
29. Beringer R. and Montgomery C. G. (1942) "The Angular Distribution of Positron Annihilation Radiation", *Physical Review*, Vol. 61, pp. 222-4.
30. DeBenedetti S., Cowan C. E., Konneker W. R., and Primakoff H. (1949) "On the Angular Distribution of Two-photon Annihilation Radiation", *Physical Review*, Vol. 77, Num. 2, pp. 205-12.
31. Singu R. M. (1974) "Measurement of the Angular Correlation of Positron Annihilation Radiation Using a Ge(Li) Detector", *Journal of Physical Chemistry: Solids*, Vol. 35, pp. 33-5.
32. Ashcroft N W. and Mermin N. D. *Solid State Physics*. Brooks/Cole Thomson Learning, Australia, 1976.
33. Major A., Fretwell H, and Alam M. (1998) "Fermi-surface Reconstruction from Two-dimensional Angular Correlation of Positron Annihilation Radiation (2D-ACAR) Data Using Maximum-likelihood Fitting of Wavelet-like Functions", *Journal of Physics: Condensed Matter*, Vol. 10, pp. 10507-15.
34. Hoffman L., Barbiellini B., Manuel A., Peter M., Rumiantsev A., and Ivanov A. (1996) "Fermi Surface of γ -tin Studied by Positron 2D-ACAR", *Physica B*, Vol. 222, pp. 31-42.

35. Kontrym-Sznajd G. and Samsel-Czekala M. (2005) "Fermi-surface Mapping from 2D Positron Annihilation Data", *Acta Physica Polonica A*, Vol. 107, pp. 586-91.
36. Jura A., Kontrym-Sznajd G. and Samsel-Czekala M. (2001) "Fermi Surface of Mg and Cd", *Journal of Physics and Chemistry of Solids*, Vol. 62, pp. 2241-7.
37. Inoue K., Saito H., Nagashima Y., Hyodo T., Nagai Y., Muramatsu S., Nagai S., and Masuda K. (2002). "A Position-Sensitive γ -Ray Detector for Positron Annihilation 2D-ACAR Based on Metal Package Photomultiplier Tubes", *Nuclear Instruments and Methods in Physics Research A*, Vol. 487, pp. 471-6.
38. Burks M. T.; Amman M.; Boggs S. E.; Hull E. L.; Luke P. N.; Madden N. W.; Riot V. J.; and Zioc K. P. "A Germanium Gamma Ray Imager with 3-D Position Sensitivity", *2001 IEEE Nuclear Science Symposium Conference Record*, Institute of Electrical and Electronics Engineers Inc., 2001, pp. 223-5.
39. Alberigi Quaranta A., Martini M., and Ottaivani G. (1969) "The Pulse Shape and Timing Problem in Solid State Detectors", *IEEE Transactions on Nuclear Science*, Vol. NS-16, Iss. 2, pp. 35-61.
40. Vetter K., Kuhn A., Deleplanque M. A., Lee I. Y., Stephens F. S., Schmid G. J., Beckedahl D., Blair J. J., Clark R. M., Cromaz M., Diamond R. M., Fallon P., Lane G. J., Kammeraad J. E., Macchiavelli A. O., and Svensson C. E. (2000) "Three-Dimensional Position Sensitivity in Two-Dimensionally Segmented HPGe Detectors", *Nuclear Instruments and Methods in Physics Research A*, Vol. 452, Iss. 1, pp. 223-38.
41. Cooper R. J., Boston A. J., Boston H. C., Creswell J. R., Grint A. N., Mather A. R., Nolan P. J., Scraggs D. P., Turk G, Hall C. J., Lazarus I., Berry A., Beveridge T., Gillam J., and Lewis R. A. (2007) "SmartPET: Applying HPGe and Pulse Shape Analysis to Small-Animal PET", *Nuclear Instruments and Methods in Physics Research A*, Vol. 459 Iss. 1, pp. 313-7.
42. Amman M., Luke P. N. (2000) "Three-Dimensional Position Sensing and Field Shaping in orthogonal-Strip Germanium Gamma-Ray Detectors", *Nuclear Instruments and Methods in Physics Research A*, Vol. 452 Iss. 1, pp. 155-66.
43. Inderhees S., Philips B., Kroeger R., Johnson W., Kinzer R., Kurfess J., Graham B., and Gehrels N. (1996) "Spectroscopy, Imaging and Compton-scatter Polarimetry with a Germanium Strip Detector", *IEEE Transactions on Nuclear Science*, Vol. 43, Num. 3, pp. 1467-71.
44. Rossi G., Morse J., and Protic D. (1997) "Energy Resolution of Germanium Microstrip Detectors at X-ray Energies 15 to 100 keV", *IEEE Transactions on Nuclear Science*, Vol. 46, Iss. 3, pp. 765-73.

45. Advanced Measurement Technology, Inc. (2002) *Ortec Model 113 Scintillation Preamplifier Operating and Service Manual*. Oak Ridge, Tennessee.
46. Kurokawa M., Shimoura S., Iwasaki H., Baba H., Michimasa S., Ota S., and Murakami H. (2003) "Pulse Shape Simulation and Analysis of Segmented Ge Detectors for Position Extraction", *IEEE Transactions on Nuclear Science*, Vol. 50 Num. 5, pp. 1309-16.
47. Brudanin V. B., Morozov V. A., and Morozova N. V. (2004) "Application of Computers in Experiments: A Statistical Method of Pulse Shape Analysis and Its Applications to Nuclear Spectroscopy", *Instruments and Experimental Techniques*, Vol. 47, Num. 6, pp. 755-61.
48. Wieland O., Camera F., Million B. Bracco A., Pignanelli M., Ripamonti G., Geraci A., and Van der Marel J. (2001) "Efficiency of Segmented HPGe Detectors: Design Criteria for Pulse Shape Analysis", *IEEE Transactions on Nuclear Science*, Vol. 48 Num. 3, pp. 296-301.
49. Blair J., Beckedahl D., Kammaradd J., and Schmid G. (1999) "Spatial Resolution Attainable Germanium Detectors by Pulse Shape Analysis", *Nuclear Instruments and Methods in Physics Research A*, Vol. 422, Iss. 1, pp. 331-336.
50. Crespi F. C. L., Camera F., Wieland O., Benzoni G., Brambilla S., Million B., and Montanari D. (2007) "A Pulse Shape Analysis Algorithm for HPGe Detectors", *Nuclear Instruments and Methods in Physics Research A*, Vol. 570, Issue 2, pp. 459-66.
51. Burks M., Jordan E., Hull E., Mihailescu L., and Vetter K. (2004) "Signal Interpolation in Germanium Detectors for Improved 3-D Position Resolution", *2004 IEEE Nuclear Science Symposium Conference Record*. Italy, pp. 1114-8.
52. Cooper R. J., Boston A. J., Boston H. C., Creswell J. R., Grint A. N., Harkness L. J., , Nolan P. J., Oxley D. C., Scraggs D. P., Lazarus I., Simpson J., and Dobson J. (2008) "Charge Collection Performance of a Segmented Planar High-purity Germanium Detector", *Nuclear Instruments and Methods in Physics Research A*, Vol. 595, pp. 401-9.
53. C S Williams, W P Baker, L W Burggraf, P E Adamson, and J C Petrosky. "Toward Simultaneous 2D ACAR and 2D DBAR: Subpixel Spatial Characterization of a Segmented HPGe Detector Using Transient Charges", accepted by *IEEE Transaction on Nuclear Science*, January 4, 2010.

- 54 Gao F., Campbell L., Xie Y., Devanathan R., Peurrung A., and Weber W. (2008) "Electron-Hole Pairs Created by Photons and Intrinsic Properties in Detector Materials", *IEEE Transactions on Nuclear Science*, Vol. 55, Num. 3, pp. 1079.
- 55 Evans R. D. (1955) *The Atomic Nucleus*, McGraw-Hill Publishing Company Ltd., Bombay.
- 56 Hayward J. and Wehe D. (2008) "Incomplete Charge Collection in a HPGe Double-Sided Strip Detector", *Nuclear Instruments and Methods in Physics Research Section A: Accelerators, Spectrometers, Detectors and Associated Equipment*, vol 586, iss 2, pp. 215-23.
- 57 <http://physics.nist.gov/PhysRefData/XrayMassCoef/ElemTab/z32.html>
- 58 Bailey, M. E. and Sparks W. B. (1983) "The Quick Convolution of Galaxy profiles, with Application to Power-law Intensity Distributions", *Monthly Notices of the Royal Astronomical Society*, vol 204, pp. 53-58.
59. Shur M. *SiC and Related Materials and Devices*. Euro Conference on Advanced Heterostructure Devices for Micro and Optoelectronics II, June 1998.
<http://nina.ecse.rpi.edu/shur/>
60. Orlinski S. B., Schmidt J., Mokhov E. N., and Baranov P. G. (2003) "Silicon and Carbon Vacancies in Neutron-Irradiated SiC: A High-Filed Electron Paramagnetic Resonance Study", *Physical Review B*, Vol. 67 pp. 125207-1 through 125207-8.
61. Vlaskina S, Vlaskin V, Podlasov S, Rodionov V, and Svechnikov G. (2007) "Boron, Aluminum, Nitrogen, and Oxygen Impurities in Silicon Carbide", *Semiconductor Physics, Quantum Electronics and Optoelectronics*, Vol. 10, Num. 2, pp. 21-5.
62. Dalibor T, Trageser H; Pensl G; Kimoto T; Matsunami H; Nizhner D, Shigiltchoff O; Choyke W. (1999) "Oxygen In Silicon Carbide: Shallow Donors and Deep Acceptors", *Proceedings of the 1998 2nd European Conference on Silicon Carbide and Related Materials*, Montpellier, 1998.
63. Bermudez, V. (1989) "Photoemission Study of Oxygen Adsorption on (001) Silicon Carbide Surfaces", *Journal of Applied Physics*, Vol. 66, Iss. 12, pp. 6084-92.
64. Duan, X. (2010) Personal communications and email.
- 65 Lam C., Lam T., Ling C., Fung S., Beling C., De-Sheng H., and Huimin W. (2004) "Positron Lifetime Studies on 8 MeV Electron-irradiated N-type 6H Silicon Carbide", *Journal of Physics Condensed Matter*, Vol. 16, pp. 8409-19.

- 66 Rempel A., Blaurock K., Reichle K., Sprengel W., and Schaefer. (2002) "Chemical Environment of Atomic Vacancies in Electron Irradiated Silicon Carbide Measured by 2D-Doppler Broadening Technique", *Materials Science Forum*, Vol. 389-33, pp. 485-8.
- 67 Kawasuso A., Chiba T., and Higuchi T. (2005) "Angular Correlation of Annihilation Radiation Associated with Vacancy Defects in Electron-irradiated 6H-SiC", *Physical Review B*, Vol. 71, pp. 193204:1-4.
- 68 Anwand W.; Brauer G.; Wirth H.; Skorupa W.; and Coleman P. (2002) "The Influence of Substrate Temperature on the Evolution of Ion Implantation-Induced Defects in Epitaxial 6H-SiC", *Applied Surface Science*, Vol 194, Num. 1, pp. 127-130.
- 69 Uedono A., Tanigawa S., Ohshima T., Itoh H., Aoki Y., Yoshikawa M., and Nashiyama I. (1999) "Oxygen-related Defects in O⁺-implanted 6H-SiC Studied by Monoenergetic Positron Beam", *Journal of Applied Physics*, Vol. 86, pp. 5392-8.
- 70 Van Veen A.; Schut H.; Clement M.; Kruseman A.; Ijpma M.R.; De Nijs J.M.M. (1995) "VEPFIT Applied to Depth Profiling Problems", *Applied Surface Science* Vol. 85, pp. 216-24.
- 71 Gentils A., Barthe M. F., Thome L., and Behar M. (2008) "Determination of Defects in 6H-SiC Single Crystals Irradiated with 20 MeV Au Ions", *Applied Surface Science*, Vol. 255, pp. 78-80.
- 72 Szpala S., Asoka-Kumar P., Nielsen B., Peng J., Hayakawa S., Lynn K., and Gossman H. (1996) "Defect Identification Using the Core-electron Contribution in Doppler-broadening Spectroscopy of Positron-annihilation Radiation", *Physical Review B*, Vol. 54, Num. 7, pp 4722-31.
- 73 Howell R., Meyer P., Rosenberg I., and Fluss M. (1985) "Two-dimensional Electron-positron Momentum Measurement at a Copper Single-crystal Surface", *Physical Review Letters*, Vol. 54, Num. 15, pp. 1698-701.
- 74 Senicki E., Becker H., Gould A., West R., and Hogg B. (1973) "Positron Annihilation in Copper Single Crystals", *Journal of Physical Chemical Solids*, Vol. 34, pp. 673-7.
- 75 Tanigawa S., Ito K., Terakado S., Morisue A., Fujii S. and Iwase Y. (1985) "2D-ACAR in Al and Cu Single Crystals Containing Edge Dislocations". *Positron Annihilation*, World Scientific Publishing Co., Singapore, pp. 288-90.

76. Sulham Clifford. (2004) *Special Nuclear Material Imaging Using a High Purity Germanium Double Sided Strip Detector*. Thesis. The Air Force Institute of Technology.
77. Personal and email communications with Dr. Ethan Hull and Mr. Dave Brumgard from PHDS Co.
78. X-Ray Instrumentation Associates. *Digital Gamma Finder (DGF) DGF-4C Manuals Version 3.04*. January 2004. Newark, California.
79. Rothenbush Fred. (2005) *Improved Multinuclide Imaging of Special Nuclear Material Using a High Purity Germanium Double Sided Strip Detector*. Thesis. The Air Force Institute of Technology.
80. Hayward J. P. (2008) *Charge Loss Correction and Inter-strip Interpolation in a High-purity Germanium Double-sided Strip Detector*. Dissertation. University of Michigan.
81. Eckert & Ziegler, Isotope Products. *Eckert & Ziegler Reference & Calibration Sources Product Information*. Valencia, CA.
82. Cree, Incorporated. *CREE Silicon Carbide Substrates and Epitaxy: Product Specifications*. Durham, NC.
83. http://www.aimalloys.com/solder_chart.htm
84. <http://www.newport.com/>
85. Agostinelli S, et al. (2003) "Geant4: A simulation toolkit", *Nuclear Instruments and Methods in Physics Research A*, Vol. 506, pp. 250-303.
86. Allison, J.; et al. (2006) "Geant4 developments and applications", *IEEE Transactions on Nuclear Science*, Vol. 53, Num. 1, pp. 270-278.
87. Ziegler J F, Biersack J P, and Ziegler M D. (2009) *The Stopping and Range of Ions in Solids*. Pergamon Press, New York.
88. Kingery W, Bowen H and Uhlmann D. (1960) *Introduction to Ceramics*, John Wiley and Sons, New York, pp. 217-39.
89. Tairov Y and Tsvetkov V. (1988) *Compound Semiconductors A4B4*, "Handbook on Electronic Materials, Energoatomizdat, Leningrad, vol. 3, p. 446.
90. Olsen J., Kirkegaard P., Pedersen N. and Eldrup M. (2006) *PALSfit: A Computer Program for Analyzing Positron Lifetime Spectra*. Riso National Laboratory, Denmark.

91. Williams C. and Johnson S. (2009) *AFIT/ENP and AFRL/RWME and TECHNICAL MEMORANDUM 09-01: PALSfit (Version 1.40) Program Execution Procedure*. Requests for the document can be made to Air Force Research Laboratory, Munitions Directorate, Energetic Materials Branch (AFRL/RWME), Eglin AFB FL 32542-5910
92. Campillo Robles J., Ogando E., and Plazaola F. (2007) “Positron Lifetime Calculation for the Elements of the Periodic Table”, *Journal of Physics: Condensed Matter*, Vol. 19, pp. 176222-42.
93. Senicki E., Becker H., Gould A., West R., and Hogg B. (1973) “Positron Annihilation in Copper Single Crystals”, *Journal of Physical Chemical Solids*, Vol. 34, pp. 673-7.
94. McKelvey P. (1993) *Solid State Physics for Engineering and Materials Science*. Krieger Publishing Company, Malabar, Florida.
95. Lide D. (2009) *CRC Handbook of Chemistry and Physics, 90th Edition*. CRC Press Taylor and Francis Group, Boca Raton, Florida.
96. Muller M., Rempel A., Reichle K., Sprengel W., Major J., and Schaefer H. (2001) “Identification of Vacancies on Each Sublattice of SiC by Coincident Doppler Broadening of the Positron Annihilation Photons after Electron irradiation”, *Materials Science Forum*, Vols. 363-5, pp. 70-2.

REPORT DOCUMENTATION PAGE				Form Approved OMB No. 0704-0188	
Public reporting burden for this collection of information is estimated to average 1 hour per response, including the time for reviewing instructions, searching existing data sources, gathering and maintaining the data needed, and completing and reviewing this collection of information. Send comments regarding this burden estimate or any other aspect of this collection of information, including suggestions for reducing this burden to Department of Defense, Washington Headquarters Services, Directorate for Information Operations and Reports (0704-0188), 1215 Jefferson Davis Highway, Suite 1204, Arlington, VA 22202-4302. Respondents should be aware that notwithstanding any other provision of law, no person shall be subject to any penalty for failing to comply with a collection of information if it does not display a currently valid OMB control number. PLEASE DO NOT RETURN YOUR FORM TO THE ABOVE ADDRESS.					
1. REPORT DATE (DD-MM-YYYY) 25-03-2010		2. REPORT TYPE Doctoral Dissertation		3. DATES COVERED (From - To) June 2007 - March 2010	
4. TITLE AND SUBTITLE Three Dimensional Positron Annihilation Momentum Measurement Technique (3DPAMM) Applied to Measure Oxygen-Atom Defects in 6H Silicon Carbide				5a. CONTRACT NUMBER	
				5b. GRANT NUMBER	
				5c. PROGRAM ELEMENT NUMBER	
6. AUTHOR(S) Williams, Christopher S., Lt Col, USAF				5d. PROJECT NUMBER	
				5e. TASK NUMBER	
				5f. WORK UNIT NUMBER	
7. PERFORMING ORGANIZATION NAME(S) AND ADDRESS(ES) Air Force Institute of Technology Graduate School of Engineering and Management (AFIT/EN) 2950 Hobson Way WPAFB OH 45433-7765				8. PERFORMING ORGANIZATION REPORT NUMBER AFIT/DS/ENP/10-M02	
9. SPONSORING / MONITORING AGENCY NAME(S) AND ADDRESS(ES) AF Office of Scientific Research Defense Threat Reduction Agency Research AFOSR/NL DTRA/CXC 801 North Randolph Street 8725 John J. Kingman Road MSC 6201 Arlington VA 22203-1977 Ft. Belvoir VA 22060				10. SPONSOR/MONITOR'S ACRONYM(S) AFOSR/NL DTRA/CXC	
				11. SPONSOR/MONITOR'S REPORT NUMBER(S)	
12. DISTRIBUTION / AVAILABILITY STATEMENT APPROVED FOR PUBLIC RELEASE; DISTRIBUTION UNLIMITED					
13. SUPPLEMENTARY NOTES Additional Sponsor: Department of Homeland Security (DHS/Tech. Branch), 245 Murrey Drive, Building 410, Washington DC 20528					
14. ABSTRACT A three-dimensional Positron Annihilation Spectroscopy System (3DPASS) capable to simultaneously measure three-dimensional electron-positron (e^-e^+) momentum densities measuring photons derived from e^-e^+ annihilation events was designed and characterized. 3DPASS simultaneously collects a single data set of correlated energies and positions for two coincident annihilation photons using solid-state double-sided strip detectors (DSSD). Positions of photons were determined using an interpolation method which measures a figure-of-merit proportional to the areas of transient charges induced on both charge collection strips directly adjacent to the charge collection strips interacting with the annihilation photons. The subpixel resolution was measured for both double-sided strip detectors (DSSD) and quantified using a new method modeled after a Gaussian point-spread function with a circular aperture. Error associated with location interpolation within an intrinsic pixel in each of the DSSDs, the subpixel resolution, was on the order of ± 0.20 mm (this represents one-standard deviation). The subpixel resolution achieved was less than one twenty-fifth of the 25-mm^2 square area of an intrinsic pixel created by the intersection of the DSSDs' orthogonal charge collection strips. The 2D ACAR and CDBAR response for single-crystal copper and 6H silicon carbide (6H SiC) was compared with results in the literature. Two additional samples of 6H SiC were irradiated with 24 MeV O^+ ions, one annealed and one un-annealed, and measured using 3DPASS. Three-dimensional momentum distributions with correlated energies and coincident annihilation photons' positions were presented for all three 6H SiC samples. 3DPASS was used for the first experimental PAS measurement of the structure of oxygen defects in bulk 6H SiC.					
15. SUBJECT TERMS spatial resolution, transient charge, image charge, segmented germanium, ACAR, DBAR, Angular Correlation of Annihilation Radiation, Doppler-Broadening of Annihilation Radiation					
16. SECURITY CLASSIFICATION OF:			17. LIMITATION OF ABSTRACT	18. NUMBER OF PAGES	19a. NAME OF RESPONSIBLE PERSON
a. REPORT	b. ABSTRACT	c. THIS PAGE			Larry W. Burggraf, PhD, (ENP)
U	U	U	UU	198	19b. TELEPHONE NUMBER (include area code) (937) 255-3636 ext 4507 lburggraf@afit.edu